THÈSE DE DOCTORAT

NNT : 2023UPAST089

Development of optical diagnostics for quantitative imaging of evaporating fuel films and soot in combustion

Développement de diagnostics optiques pour l'imagerie quantitative des films de carburant en évaporation et de la suie en combustion

Thèse de doctorat de l'université Paris-Saclay et de l'université de Duisburg-Essen

École doctorale n° 579,
Sciences Mécaniques et Energétiques, Matériaux et Géosciences (SMEMAG)
Spécialité de doctorat : Combustion

Thèse préparée à l'IFP Energies Nouvelles, Direction Mobilité et Système (Rueil-Malmaison, France) et à l'université de Duisburg-Essen (UDE, Duisburg and Essen, Allemagne), sous la direction de **Gilles BRUNEAUX**, Dr. HDR, la co-direction de **Sebastian KAISER**, Prof, le co-encadrement de **Michele BARDI**, Dr.

Thèse soutenue à Duisburg, le 04 Octobre 2023, par

Kamal SHWAY

Composition du Jury

Membres du jury avec voix délibérative

Christof SCHULZ Professeur, Université de Duisburg - Essen	Examinateur
Stefan WILL Professeur, Université d'Erlangen - Nürnberg	Examinateur & Rapporteur
Christine ROUSSELLE Professeure, Université d'Orléans	Présidente & Rapporteure
Guillaume PILLA Docteur, HDR, Université de Paris - Saclay	Examinateur
Sebastian A. KAISER Professeur, Université de Duisburg - Essen	Examinateur

Development of optical diagnostics for quantitative imaging of evaporating fuel films and soot in combustion

Von der Fakultät für Ingenieurwissenschaften, Abteilung Maschinenbau
und Verfahrenstechnik der
Universität Duisburg-Essen
zur Erlangung des akademischen Grades

eines

Doktors der Ingenieurwissenschaften

Dr.-Ing.

genehmigte Dissertation

von

Kamal SHWAY
aus
Deir El Qamar, Libanon

Gutachter: Univ.-Prof. Dr. Sebastian Kaiser
Professorin Christine Rousselle
Univ.- Prof. Dr.-Ing. Stefan Will

Tag der mündlichen Prüfung: 4.10.2023

Acknowledgements

First of all, I would like to express my sincere gratitude to my supervisors, Michele Bardi, Gilles Bruneaux, and Sebastian Kaiser, for giving me the opportunity to join their research groups at IFPEN and the University of Duisburg-Essen (UDE) as a PhD student, which has been a privilege and an invaluable experience for me. I am grateful for their unwavering support and encouragement throughout my research journey. Their expertise and advice were instrumental in shaping my research work, and their valuable feedback helped me refine my ideas and arguments. I would also like to thank Niklas Jüngst, my colleague at the UDE, who generously shared his time and expertise to support my experimental campaign in Duisburg.

I would also like to thank IFPEN, the University of Paris Saclay, in particular the SMEMaG doctoral school, and the UDE for giving me the opportunity to enroll in their renowned Cotutelle PhD program. I would like to thank IFPEN and Sebastian A. Kaiser's group for providing me with the necessary infrastructure and equipment to carry out my research in France and in Duisburg. I am grateful to the technicians (especially to Clément Bramoullé) and engineers of the optical diagnostics group at IFPEN, and to Niklas Jüngst and Joel Albrecht at UDE for their help and support during the experiments. I would like to thank my fellow PhD students at IFPEN: Abhijit, Mohammed-Amine, Louise, Maxime, and Outmane, and at UDE: Fangyi, Sadrollah, Asif, Kai, and Judith.

I am also deeply grateful to my father, who unfortunately passed away during the first year of my thesis, to my mother and to my entire family, for their support throughout my thesis journey. Their love, understanding, and encouragement have been a constant source of motivation and inspiration, and I am forever grateful for their presence in my life.

Finally, I would like to thank all the people who have directly or indirectly contributed to the success of this thesis and have encouraged and supported me to complete this work.

Abstract

Spray impingement and the resulting non-evaporated liquid fuel films are main causes of soot formation in gasoline direct-injection (GDI) engines. This work presents an experimental investigation of liquid fuel-film formation and evaporation, and fuel-film premixed-flame interaction at conditions representative for engines. Two experimental campaigns were conducted at IFPEN (France) and the University of Duisburg-Essen (UDE, Germany).

The experiments at IFPEN were performed in a constant-volume vessel. One of the 8-hole "Spray G" injectors from the Engine Combustion Network (ECN) was used, with a transparent plate mounted perpendicular to the injector axis at 30 mm from the nozzle. A fuel surrogate consisting of 30% toluene - 70% iso-octane was injected at 200 bar, under non-reacting and reacting conditions. UV-absorption imaging and diffused back-illumination (DBI) techniques were used to measure liquid-fuel film thickness and soot extinction, respectively. Since vapor and liquid cannot be distinguished spectrally, morphological post-processing was developed to separate the diffuse, moving vapor and soot clouds from the sharp, stationary features of the fuel film. Spatio-temporally resolved measurements of the film thickness were obtained by high-speed imaging of the UV absorption of toluene. DBI images at 810 nm provided information on soot formation due to film/flame interaction and its spatial distribution at different oxygen excess percentages.

At the UDE, a UV-vis absorption technique was developed to image the fuel-film thickness after direct injection in a heated constant-flow facility in the presence of fuel-vapor and soot. A six-hole GDI injector sprayed fuel at 100 bar onto a transparent plate 30 mm from the nozzle. The gas and wall temperatures were respectively 103 and 79°C, and the gas pressure 1 bar. Another fuel surrogate consisted of a mixture of 30% toluene - 60% iso-octane - 10% n-octane (boiling points 110, 99 and 125°C, respectively) was also used. Absorption by toluene vapor was estimated similarly as at IFPEN. The contributions of scattering and soot extinction at 265 nm were estimated from absorbance images at 310, 365, and 520 nm. Soot incandescence was accounted from dark frame images. The multi-spectral approach permitted obtaining spatio-temporally resolved fuel-film thickness measurements and additional information on the soot.

Keywords:

UV-vis absorption, Liquid fuel-film thickness, Fuel-film evaporation, Soot extinction, High-speed imaging, Engine Combustion Network.

Résumé

L'impact du spray de carburant injecté et les films liquides non évaporés qui en résultent sont les principales causes de la formation de suie dans les moteurs à injection directe d'essence (GDI). Ce travail présente une étude expérimentale de la formation et de l'évaporation du film de carburant liquide, ainsi que de l'interaction entre le film de carburant et la flamme de prémélange dans des conditions représentatives des moteurs. Deux campagnes expérimentales ont été menées à IFPEN (France) et a l'Université de Duisburg-Essen (UDE, Allemagne).

Les expériences menées à IFPEN ont été réalisées dans une cellule à volume constant. L'un des injecteurs "Spray G" à 8 trous du réseau Engine Combustion Network (ECN) a été utilisé, avec une plaque transparente montée perpendiculairement à l'axe de l'injecteur à 30 mm de la buse. Un substitut de carburant composé de 30 % de toluène - 70 % d'iso-octane a été injecté à 200 bar, dans des conditions non-réactives et réactives. L'imagerie par absorption UV et les techniques de rétro-illumination diffuse (DBI) ont été utilisées pour mesurer l'épaisseur du film liquide-carburant et l'extinction de la suie, respectivement. La vapeur du carburant et le film liquide ne pouvant être distingués spectralement, un post-traitement morphologique a été mis au point pour séparer les nuages de vapeur et de suie diffus et mobiles des caractéristiques nettes et fixes du film de combustible. Des mesures spatio-temporelles de l'épaisseur du film ont été obtenues par imagerie à grande vitesse de l'absorption du toluène dans l'ultraviolet. Les images DBI à 810 nm ont fourni des informations sur la formation de suie due à l'interaction film/flamme et sur sa distribution spatiale à différents pourcentages d'excès d'oxygène.

À l'UDE, une technique d'absorption UV-vis a été mise au point pour obtenir des images de l'épaisseur du film de carburant après injection directe dans une installation chauffée à flux constant en présence de vapeur de carburant et de suie. Un injecteur GDI à six trous a injecté du carburant à 100 bar sur une plaque transparente située à 30 mm de la buse. Les températures du gaz et de la paroi étaient respectivement de 103 et 79°C, et la pression du gaz de 1 bar. Un autre substitut de carburant composé d'un mélange de 30 % de toluène - 60 % d'iso-octane - 10 % de n-octane (points d'ébullition 110, 99 et 125°C, respectivement) a également été utilisé. L'absorption par les vapeurs de toluène a été estimée de la même manière qu'à IFPEN. Les contributions de la diffusion et de l'extinction des suies à 265 nm ont été estimées à partir des images d'absorbance à 310, 365 et 520 nm. L'incandescence des suies a été prise en compte à partir d'images acquises en obscurité. L'approche multispectrale a permis d'obtenir des mesures

spatio-temporelles de l'épaisseur du film de combustible, ainsi que des informations supplémentaires sur la suie.

Mots clés :

Absorption UV-vis, Épaisseur du film de carburant liquide, Évaporation du film de carburant, Extinction de la suie, Imagerie à haute vitesse, Engine Combustion Network.

Kurzfassung

Das Auftreffen des Kraftstoffsprays auf Zylinderinnenwände und die daraus resultierenden nicht verdampften Flüssigkraftstofffilme sind die Hauptursache für die Rußbildung in Motoren mit Benzindirekteinspritzung (GDI). In dieser Arbeit wird eine experimentelle Untersuchung der Bildung und Verdampfung von Flüssigkraftstofffilmen und der Wechselwirkung zwischen Kraftstofffilm und vorgemischter Flamme unter für Motoren repräsentativen Bedingungen vorgestellt. Zwei Messkampagnen wurden dafür am IFPEN (Frankreich) und an der Universität Duisburg-Essen (UDE, Deutschland) durchgeführt.

Die Experimente am IFPEN wurden in einem Behälter mit konstantem Volumen durchgeführt. Es wurde eine der 8-Loch "Spray G"-Einspritzdüsen des Engine Combustion Network (ECN) verwendet, wobei eine transparente Platte senkrecht zur Achse der Einspritzdüse in einem Abstand von 30 mm von der Düse angebracht wurde. Ein Kraftstoffsurrogat aus 30 % Toluol - 70 % Iso-Oktan wurde mit 200 bar unter nicht reagierenden und reagierenden Bedingungen eingespritzt. Zur Messung der Schichtdicke des Flüssigbrennstoffs und der Ruß-Extinktion wurden UV-Absorptions- und DBI-Techniken (Diffused Back-Illumination) eingesetzt. Da Dampf und Flüssigkeit spektral nicht unterschieden werden können, wurde eine morphologische Nachbearbeitung entwickelt, um die diffusen, sich bewegenden Dampf- und Rußwolken von den scharfen, stationären Merkmalen des Brennstofffilms zu trennen. Räumlich und zeitlich aufgelöste Messungen der Filmdicke wurden durch Hochgeschwindigkeitsaufnahmen der UV-Absorption von Toluol gewonnen. DBI-Bilder bei 810 nm lieferten Informationen über die Rußbildung aufgrund der Wechselwirkung zwischen Film und Flamme und deren räumliche Verteilung bei unterschiedlichen Sauerstoffüberschüssen.

An der UDE wurde ein UV-Vis-Absorptionsverfahren entwickelt, um die Dicke des Kraftstofffilms nach der Direkteinspritzung in einer beheizten Strömung mit Atmosphärendruck in Gegenwart von Kraftstoffdampf und Ruß abzubilden. Ein GDI-Injektor mit sechs Löchern spritzte Kraftstoff mit 100 bar auf eine transparente Platte 30 mm von der Düse entfernt. Die Gas- und Wandtemperaturen betrugen 103 bzw. 79 °C, der Gasdruck 1 bar. Ein weiteres Kraftstoffsurrogat, bestehend aus einer Mischung von 30 % Toluol - 60 % Iso-Oktan - 10 % n-Oktan (Siedepunkte 110, 99 bzw. 125 °C), wurde ebenfalls verwendet. Die Absorption durch Toluoldampf wurde in ähnlicher Weise wie beim IFPEN geschätzt. Die Beiträge der Streuung und der Ruß-Extinktion bei 265 nm wurden anhand der Absorptionsbilder bei 310, 365 und 520 nm geschätzt. Die Rußinkandeszenz wurde anhand durch Abzug von Dunkel-Bildern verrechnet. Der multispektrale Ansatz ermöglichte räumlich und zeitlich

aufgelöste Messungen der Dicke des Kraftstofffilms und zusätzliche Informationen über den Ruß.

Schlüsselwörter:

UV-Vis-Absorption, Dicke des Flüssigkraftstofffilms, Verdampfung des Kraftstofffilms, Ruß-Extinktion, Hochgeschwindigkeitsbildgebung, Engine Combustion Network.

List of symbols

Symbol	Meaning	Unit
W_t^{dark}	dark image acquired before W_t	counts
k_λ^t	Correction coefficient at time t	-
μ	Detection efficiency	-
A	Absorbance	-
A_λ	Absorbance image at λ	-
c	Concentration	mol l^{-1}
d	Thickness	µm
D	Diameter	cm
$d(t)$	Thickness image at time t	µm
f	Frame rate acquisition	fps
f_v	Soot volume fraction	-
I	Transmitted light	counts
I_0	Incident light	counts
I_a	Absorbed intensity	-
I_{dark}	Dark image	counts
I_{dry}	Scattered intensity without a liquid film	counts
I_f	Fluorescence intensity	-
I_{ref}	Reference image	counts
I_t	Intensity image at time t	counts
I_{wet}	Scattered light intensity with a liquid film	counts
K	Extinction coefficient	-
k_e	Dimensionless extinction coefficient	-
KL	Optical density	-
L	Path length	cm
m	Mass	mg
m_{ini}	Initial deposited fuel mass	mg
m_{spray}	Mass of spray	mg
p	Pressure	bar
p_{cell}	Cell pressure	bar
p_{inj}	Injection pressure	bar
S	Size of the image plane	cm
t	Time	sec
T	Temperature	°C
T_{air}	Air flow temperature	°C
T_{fuel}	Fuel temperature	°C
t_{inj}	Time of injection	ms
T_{wall}	Wall temperature	°C
W_{ref}	Reference image	counts
W_t	Image at time t	counts
X	Molar fraction	-
Y	Mass fraction	-

α	Beam steering angle	deg
ε	Molar absorptivity	l mol^{-1} cm^{-1}
ζ	Residual oxygen excess	%
θ	Diffuser angle	deg
λ	Wavelength	nm
Φ	Fluorescence quantum yield	-
ω	Acceptance angle	deg

List of abbreviations

Abbreviation	Description
aSOI	After start of injection
BDC	Bottom dead center
BEV	Battery electric vehicle
bSOI	Before start of injection
CA	Crank angle
CMOS	Complementary metal-oxide semiconductor
CWL	Center wavelength
DBI	Diffused back illumination
DISI	Direct injection spark ignition
EV	Electric vehicle
FCEV	Fuel cell electric vehicle
FS1	Fuel surrogate 1
FS2	Fuel surrogate 2
FWHM	Full width at half maximum
GDI	Gasoline direct injection
IR	Infrared
LCV	Light-commercial vehicle
LED	Light-emitting diode
LIF	Laser-induced fluorescence
LII	Laser induced incandescence
nd	Neutral density
Nd:YAG	Neodymium-doped yttrium aluminum garnet
PAH	Polycyclic aromatic hydrocarbon
PFI	Port fuel injection
PHEV	Plug-in hybrid vehicle
PLDV	Passenger light-duty vehicle
PM	Particulate matter
PN	Particulate number
QE	Quantum efficiency
RIM	Refractive index matching
ROI	Region of interest
SM	Spatial mask
SOI	Start of injection
STM1	First spatio-temporal mask
STM2	Second spatio-temporal mask
TDC	Top dead center
TWC	Three-way catalyst
UV	Ultraviolet
UV-vis	Ultraviolet-visible

Table of contents

1 Introduction

1.1 Motivation

So far, combustion is the dominant energy conversion process, in which fuel reacts with an oxidizer (usually oxygen in the air) to release energy and combustion products. In transportation, the internal combustion engine (ICE) is currently the primary energy conversion system for most vehicles due to its efficiency, versatility, and low operating costs. There are two main types of ICE on the market: the spark-ignition (gasoline) engine and the compression-ignition (diesel) engine. Passenger cars account for 74% of annual ICE production for light-duty trucks, heavy-duty trucks, ships, and other construction equipment [1].

Despite the historically superior efficiency of diesel engines, stringent regulations on nitrogen oxide (NO_x) and particulate number (PN) emissions, as well as the psychological and political impact of the so-called “diesel gate”, have pushed automakers to rely on cleaner gasoline engines for future powertrains [1]. Unlike diesel engines, in which fuel auto-ignition initiates the combustion process, the gasoline engine is characterized by a spark plug initiating fuel combustion. For this reason, it is commonly referred to as a spark-ignition engine [2]. There are two main types of gasoline injection systems: port fuel injection (PFI) and gasoline direct injection (GDI). The difference between these two injection systems is explained in **section 2.1**.

The introduction of direct injection systems in gasoline engines improved their efficiency, providing much higher power and performance than other gasoline injection systems while reducing CO_2 emissions. However, due to the reduced fuel atomization time in GDI engines, the directly injected fuel-spray can cause an increase in carbon particulate emissions if the spray impinges on piston or liner and forms liquid films. These liquid fuel-films evaporate slowly, and after ignition, they can interact with the premixed flame, producing soot.

Most GDI engines produce one to two times more particulate matter (PM) emissions with more ultrafine nanoparticles than conventional PFI gasoline engines. Soot hazards, which are composed of carbon nanoparticles, are an important source of air pollution, harmful to the ecosystem and human health, causing thousands of deaths around the world. In a 2017 study led by EMPA, researchers found that some GDI engines emit as much soot as unfiltered diesel cars did in the past, and that soot is strongly produced at accelerated speeds [3].

In the late 1990s, the European Union took the lead in introducing automotive emission regulations to limit pollutants such as carbon monoxide (CO), unburned

hydrocarbons (HC), NO_x, PM, and PN produced by internal combustion engines in cars. **Table 1.1** shows the evolution of European standards for PM and PN emissions from Euro5a (2009) to Euro6c (2017) [4]. The Euro 6 standards introduced new regulations on PN emissions for vehicles, requiring a closer look at all soot formation mechanisms in GDI engines. Understanding liquid fuel-film formation, evaporation, and subsequent soot formation in GDI engines is a key to improving injection strategies, engine design, and reducing soot emissions [5,6]. GDI engines must keep improving their efficiency and performance to meet the new emission regulations and to achieve efficient, clean, and flexible combustion technologies.

Emission regulations	Euro5a-September 2009	Euro5b-September 2011	Euro6b-September 2014	Euro6c-September 2017
PM (mg/ Km)	5	4.5	4.5	4.5
PN (#/Km)	-	-	6×10^{12}	6×10^{11}

Table 1.1. European automotive emission regulations for particulate matter (PM) and particulate number (PN) [4].

Figure 1.1a shows a time projection of the overall European market share of GDI engine vehicles [7]. The market of gasoline engine vehicles is moving towards direct injection. By 2025, the percentage of new vehicle sales with GDI engines is expected to exceed 95%. **Figure 1.1**b shows the evolution of the market share of GDI engine vehicles for different vehicle brands from 2001 to 2017. These traces show a trend of increasing production and sales of GDI-powered vehicles.

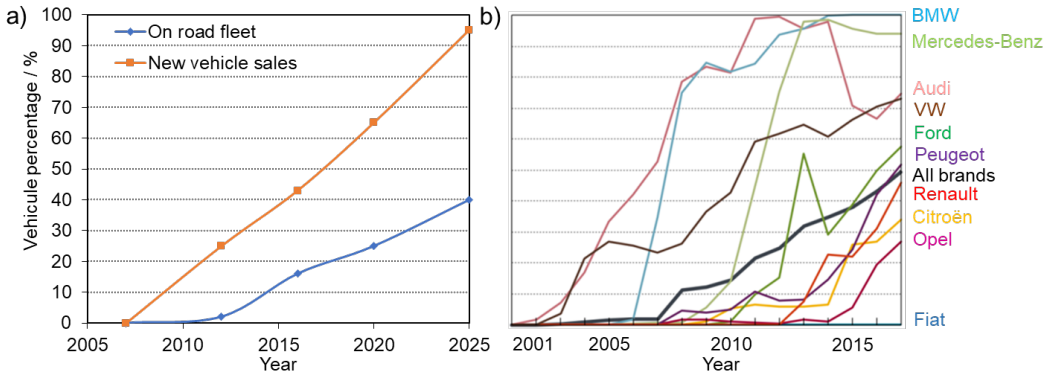

Figure 1.1. Market share of vehicles with GDI engines (a) in Europe and (b) by car brand [7].

Many countries around the world are implementing new policies to adopt cleaner car production to reduce local emissions in cities and fight climate change. Automakers are currently investing heavily in the transition to the electric vehicles (EVs). However, despite significant progress in electric vehicles, ICE vehicles still dominate the market. **Figure 1.2** shows the IEA's 2DS scenario, which gives an 80% chance of limiting the global average temperature increase to 2°C until 2050. In this scenario, despite the large increase in EVs, conventional ICE vehicles and ICE hybrids will continue to be produced in the foreseeable future and EVs will not be able to completely replace them. According to the IEA, the internal combustion engine will still be installed in more than 40% of vehicles in 2050 [8,9].

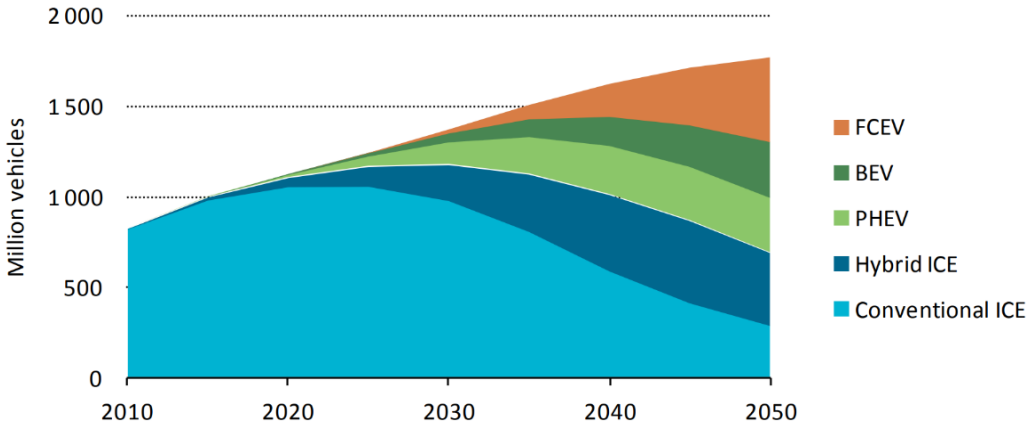

Figure 1.2. Projections of passenger car sales by powertrain type between 2010 and 2050 [9]. FCEV: fuel cell electric vehicle, BEV: battery electric vehicle, PHEV: plug-in hybrid electric vehicle.

The IEA's 2019 outlook projected future vehicle generation using two different policy scenarios: The first is the New Policies Scenario, which is based on policies and measures implemented by governments. The second is the EV30@30 scenario, which aims to achieve a 30% market share for electric vehicles in 2030 [8]. **Figure 1.3** and **Figure 1.4** show the EV stock and EV sales, respectively. In the New Policies Scenario, the EV stock will reach 130 million vehicles in 2030, of which about 50 million are hybrids.

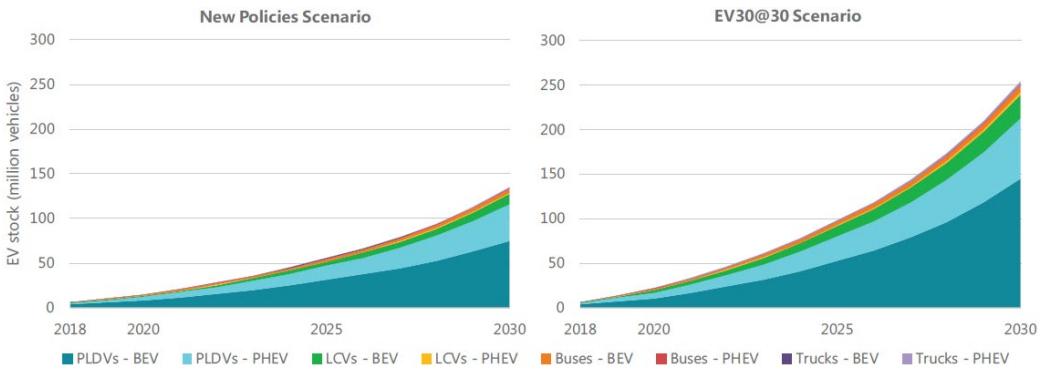

Figure 1.3. Projections of the future global EV stock according to the New Policies Scenario and the EV30@30 Scenario by scenario, between 2018 and 2030 [8]. PLDVs: passenger light-duty vehicles, LCVs: light-commercial vehicles.

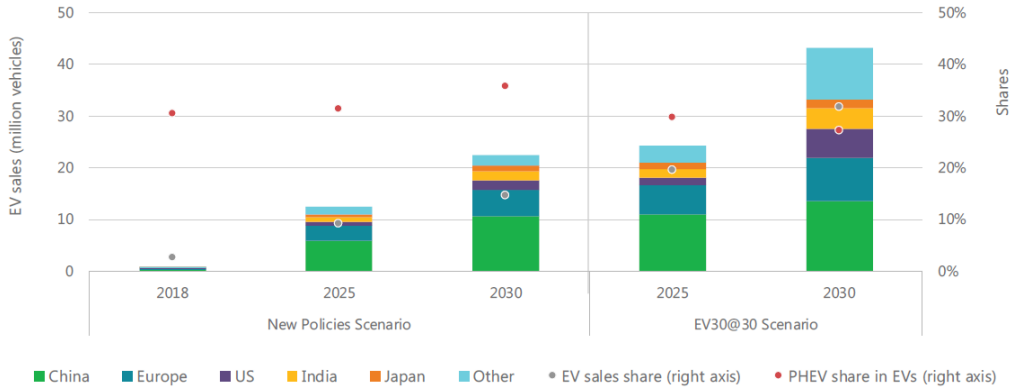

Figure 1.4. Projections of future global EV sales according to the New Policies Scenario and the EV30@30 Scenario by scenario, between 2018 and 2030 [8].

Plug-in hybrid electric vehicles (PHEVs) will account for about 38% of EV sales. In the EV30@30 scenario, the EV stock nearly doubles to 250 million vehicles in 2030, of which about 70 million are hybrids. PHEVs will account for about 28% of EV sales. The projections in both scenarios confirm that the ICE will continue to exist alongside electric vehicles in the automotive market.

Although the market trend is towards electrification of vehicles, the growing market of hybrid vehicles confirms the need for the optimization and improvement of GDI engines to meet new emission regulations, while improving engine efficiency and fuel economy.

1.2 Objectives of the thesis

This work aims at studying the formation and evaporation of liquid fuel films and the interaction between the deposited liquid fuel-films and the premixed flame under controlled thermodynamic environments and engine relevant conditions.

The objective of this thesis is to understand experimentally, using optical diagnostics, the mechanisms behind the high nanoparticle emissions in GDI engines.

With direct injection, the fuel spray impinges on the engine surfaces, resulting in the formation of liquid fuel-films. The presence of unevaporated liquid fuel-films inside the engine after ignition results in an interaction between the deposited liquid fuel-films and the premixed flame, accompanied by significant soot formation. High levels of PN and PM are produced by GDI engines, requiring further investigation of the phenomenon and the mechanisms involved. Spatio-temporally resolved measurements of the film and the related phenomena are particularly useful to validate the corresponding simulations, which necessarily rely on a variety of models for the underlying complex multi-phase physics. In engine-relevant cases, evaporating fuel films have been studied mainly by optical imaging techniques.

The next part of the thesis presents some fundamentals about gasoline engines and optical diagnostics used in the literature to study fuel-film thickness and soot extinction: the two experimental parameters we chose to study fuel-film formation, evaporation and interaction with the premixed flame. The third part is a state of the art review of fuel-film formation in GDI engines. Experimental studies in the literature on the interaction between the fuel-film and the premixed flame are presented.

The fourth part of the thesis presents the materials and methods corresponding to the two experimental campaigns carried out at IFPEN and UDE. All the experimental conditions and optical setups are presented here. The experiments at IFPEN were performed in a constant volume cell. The UV-absorption technique and DBI were used to measure fuel-film thickness and soot extinction, respectively. At UDE, a UV-vis absorption technique was developed to quantify the liquid fuel-film thickness in the presence of vapor and soot. An experimental study of fuel mixture evaporation is presented at the end of this chapter.

The last part of the thesis presents the experimental results. A morphological algorithm was developed to distinguish liquid fuel-films from vapor and soot contributions in the absorbance images. Estimation of vapor absorbance above liquid fuel-film regions was obtained by the developed algorithm. At IFPEN, the fuel-film thickness was measured after a parametric variation of the pressure and temperature of the cell under non-reacting conditions. The relationship between deposited fuel-films and soot was investigated. Simultaneous measurements of fuel-film thickness and soot extinction were performed under different experimental conditions. At UDE, quantitative results of fuel-film thickness were

obtained using the developed UV-vis absorption technique under non-reacting and reacting conditions. Additional information on soot extinction in the regions surrounding the liquid fuel-film were obtained quasi-simultaneously at different wavelengths. Fuel-thickness images and mean fuel-mass were calculated.

This work provides a better understanding of the mechanisms involved during gasoline direct injection, from the formation of liquid fuel-films and their evaporation, to combustion and the interaction between the deposited liquid fuel-films and the premixed flame, to soot formation.

2 Fundamentals

The objective of this thesis is to experimentally study the interaction between liquid fuel films and premixed flame in GDI engines. In this chapter, we first present the difference between the two main injection systems used in gasoline engines. In our study, two experimental parameters were investigated: liquid fuel-film thickness and soot extinction. Common optical diagnostics used in the literature to measure liquid fuel-film thickness and soot extinction are presented here. The advantages of using absorption technique for liquid fuel-film thickness measurement and DBI technique for soot extinction measurement over other optical diagnostics are presented at the end of this chapter.

2.1 Gasoline engines

2.1.1 Port-fuel injection

Figure 2.1 shows an example rendering view of a gasoline port-fuel injection (PFI) system. In PFI systems, the injector sprays the fuel into the intake manifold, where the fuel mixes with air before being sucked down into the combustion chamber during the intake stroke. The injection pressure is low compared to the GDI system, at about 4 bar [10]**.** The PFI system has the advantage of mixing the fuel and air well before it enters the cylinder. This causes the fuel mixture to vaporize. As a result, PFI engines do not have the problem of liquid fuel-film formation and particulate emissions. However, the injection timing cannot be controlled according to the appropriate combustion operating regime. As a result, combustion in the PFI system cannot be properly maintained at stoichiometry in the cylinder.

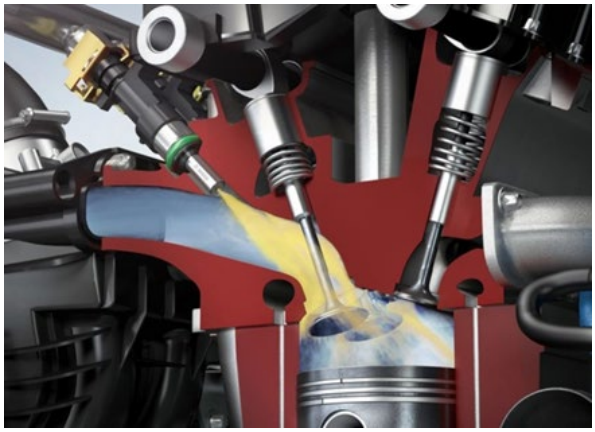

Figure 2.1. Example rendering view of the injection process in a PFI gasoline engine [11].

2.1.2 Direct injection

In the GDI system, fuel is injected directly into the combustion chamber, where the injector sprays fuel from the cylinder head. Depending on the engine regime, the injection timing is controlled and adjusted between the intake stroke and the combustion stroke. Injection timing control can be used in two different charge systems: homogeneous and stratified.

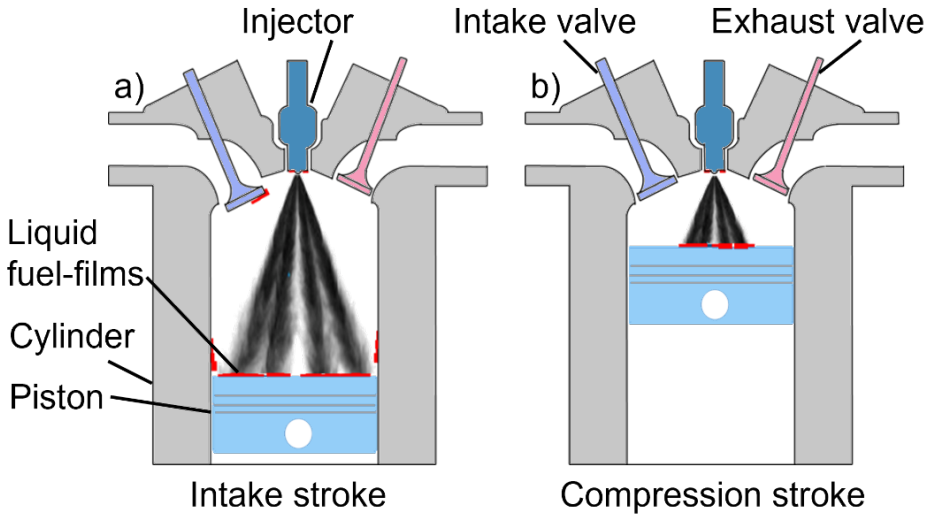

Figure 2.2. Sketch of a GDI engine operating in a homogeneous (a) and a stratified (b) charge system.

Figure 2.2a shows a sketch of a GDI engine operating in homogeneous mode. In this charge system, the fuel spray is injected as the piston moves down from the top dead center (TDC) to the bottom dead center (BDC) during the intake stroke. At high to medium loads, the GDI engine is operated in a homogeneous mode, with the injector spraying fuel during the intake stroke to ensure proper vaporization and mixing of the fuel spray with the air. In this mode, the spray has a larger spreading volume. The cylinder surfaces are likely to be extensively wetted. The intake valve, which is open during the intake stroke, is also subject to wetting, depending on the targeting of the injector. **Figure 2.2**b shows a sketch of a GDI engine operating in stratified mode. In this charge system, the fuel spray is injected as the piston moves up from the BDC to the TDC during the compression stroke. At low loads, low speeds, engine idle, and during the engine cold start conditions, the engine is operated in a stratified combustion mode late in the compression stroke [12]. This reduces fuel consumption and improves combustion stability. In both combustion modes, the fuel has less time to mix with the air.

The injection pressure in GDI engines ranges from 30 to 200 bar. Operating at a high injection pressure results in improved vaporization of the fuel spray and provides a cooling effect inside the cylinder with the ability to withstand high pressures in the combustion chamber [10]. **Figure 2.3** shows the effect of the injection pressure of a swirl injector on the droplet size. The droplet size decreased from about 20 to 15 μm by increasing the injection pressure from 50 to 150 bar [10]. Although the gas pressure and temperature are higher in stratified mode than in homogeneous mode, the fuel spray does not have enough time to mix well with the hot gases and evaporate. As a result, liquid fuel-films form mainly on the piston head and injector tip.

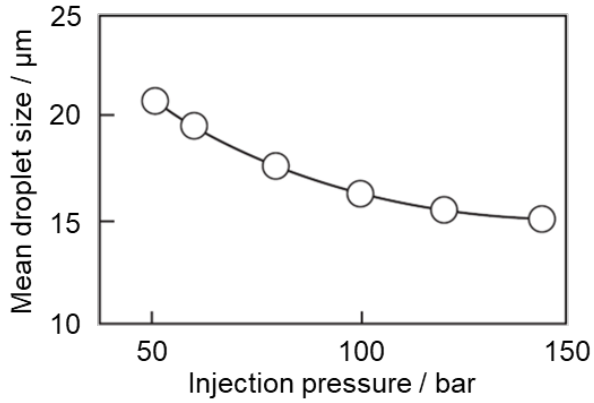

Figure 2.3. Effect of injection pressure on mean droplet size diameter [10].

In GDI engines, direct injection of the spray into the cylinder cools the air charge, reducing knock problems and increasing the compression ratio, which improves engine efficiency. In contrast, the direct injection system is more sophisticated, requiring a high-pressure fuel pump with a special injector to handle the high temperatures and pressures in the combustion chamber.

GDI engines provide a high-performance system that combines high injection pressures with precise injected fuel-mass for stoichiometric regime. The fuel is more finely atomized, allowing the engine to operate in stratified combustion mode with near-instantaneous ignition after the injection. However, the reduced time between injection and spark ignition eventually contributes to poor fuel vaporization and deposition of liquid fuel-films on the cylinder surfaces, resulting in higher soot emissions. Fuel film formation occurs in GDI engines in both homogeneous and stratified modes. The piston, injector head, spark plug, intake valve, and inner cylinder surfaces are the regions of the liquid fuel-film impact. Further studies in GDI engines are needed to understand the relationship between the presence of liquid fuel-films and soot formation and to meet future emission regulations.

2.2 Soot formation

At stoichiometry, complete combustion of a hydrocarbon fuel produces carbon dioxide and water. Soot is an unwanted byproduct of incomplete combustion or pyrolysis of the fuel. Soot formation is a complex process that is not yet fully understood despite much research on the subject. This section presents a general mechanism of soot formation. In the case of fuel/flame interaction, the liquid fuel-film is subjected to interaction with the diffusive flame in a rich combustion mode.

Soot formation can be divided into two phases: a molecular zone where soot precursors are formed in the gas phase, and a particle zone, where soot surface growth takes place in the solid phase and the coagulation of primary particles into large aggregates occurs. This evolution of soot formation can be summarized in three steps: soot particle inception, surface growth and particle agglomeration [13]. Soot emissions are the resultant competition between soot formation and oxidation. The chemical and physical structure of soot is changing and not unique, and many morphological structures are obtained during soot formation.

Figure 2.4 shows a schematic of the soot formation process [14]. After flame propagation and thermal heating, large hydrocarbon molecules are mainly converted to acetylene radicals, which are considered to be the main initiator of soot. Through polymerization, large polyacetylene hydrocarbons are formed. These are then converted to aromatics with a more massive ring structure by cyclization. The combination of aromatics produces polycyclic aromatic hydrocarbons (PAHs), known as soot precursors. All of the above steps occur at the molecular length scale in the gas phase. Next, the PAHs are converted into particle nuclei. Coagulation of the particles initiates growth of the soot surface into larger aggregates with different sizes. Finally, some soot surfaces may oxidize at elevated temperatures. It is important to note that the extinction coefficient of soot during its formation process at a given wavelength depends on its maturity [15,16]. For example, small-size PAHs have a higher extinction coefficient at short wavelengths than at long wavelengths.

In a GDI engine, soot formation is initiated by two primary sources: premixed flame formation and fuel surface wetting. Lubrication oil and other metal residues in the cylinder are also a source of soot in a GDI engine. Many strategies were developed to control soot production in GDI engines under cold-start engine conditions. The main strategy for treating soot emissions is the use of an after-treatment system. The most common after-treatment system is the three-way catalytic converter (TWC). However, under cold-start engine conditions, it takes approximately 40 to 100 seconds to reach the TWC converter light-off

temperature of approximately 250°C to treat the exhaust gases [17]. Additional hardware components, such as air pumps and electric heaters, can be used to accelerate the heating of the TWC converter. Ignition timing and delayed injection can also be used to generate hot gases, as well. In this case, no additional hardware is required to heat the gases. However, fuel consumption and emissions are expected to increase, and engine efficiency is expected to decrease because the fuel does not have sufficient time to vaporize before combustion.

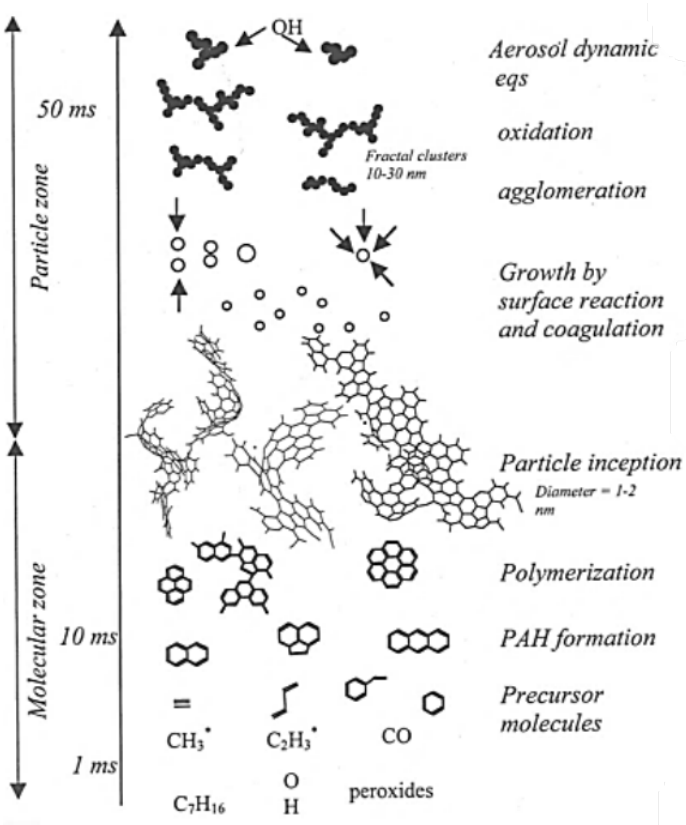

Figure 2.4. Schematic of the soot formation pathway [14].

After injection in homogeneous or stratified mode, reduced fuel evaporation results in an unevenly distributed mixture, which implies a fuel-rich zone responsible for soot formation. In a homogeneous system charge, poor air-fuel mixing can result in fuel droplets burning on spark ignition. In a stratified mode, where droplet evaporation time is short, the fuel-rich zone is formed primarily near to the injector tip and piston, resulting in high soot formation.

In GDI engines, unevaporated liquid fuel-films deposited on the internal cylinder surfaces cause soot formation. Evaporation of the liquid fuel films induces rich vapor zones near the wetted wall surfaces. After combustion, the interaction between the rich fuel-vapor zones above the liquid fuel-films and the premixed flame results in soot formation. Fuel pyrolysis may also occur at elevated

temperatures in the absence of oxygen in the zones between the premixed flame and the liquid fuel films, resulting in greater soot production [14,18,19]. Preliminary experiments performed previously by our own group at IFPEN demonstrated soot formation in GDI engines. These experiments were performed in an optical engine. **Figure 2.5** shows a sequence of light extinction images acquired from a single firing cycle. The raw extinction images show soot formation near the piston head. After injection, fuel films are deposited primarily on the piston head. The unevaporated liquid fuel films interact with the premixed flame propagating inside the combustion chamber, producing soot clouds above the fuel films.

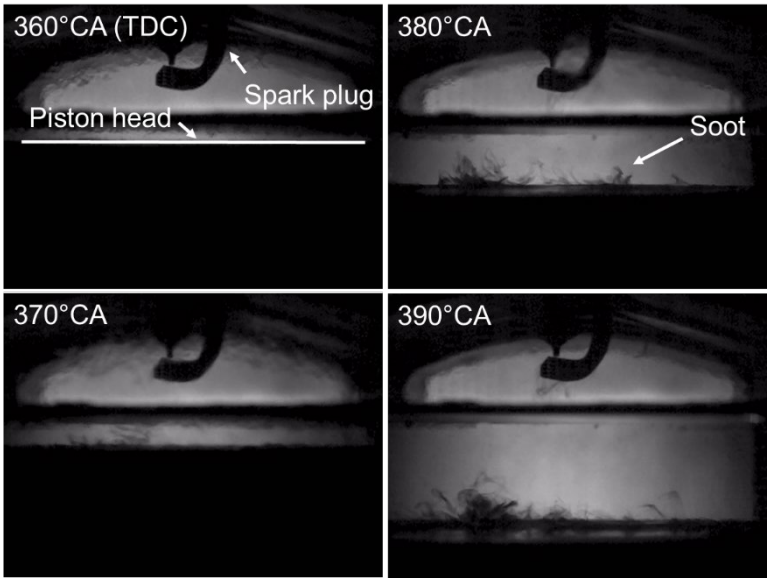

Figure 2.5. Sequence of raw light extinction images inside an optical GDI engine at 360°, 370°, 380°, and 390°CA. The images show the formation of soot clouds over the piston head early after ignition.

2.3 Optical diagnostics for fuel-film thickness measurement

Several diagnostics have been used to detect and quantify liquid-film thickness in engine-relevant cases. In this section, we present an overview of the main optical diagnostics used in the literature for liquid-fuel film thickness quantification.

2.3.1 Absorption

Absorption is the capacity of an absorbing molecule to absorb radiant energy in a specific wavelength range. During the interaction between light and the absorbing molecules, the valence electrons absorb the energy of the photons. Light absorption ranges from the far UV (180nm) to the near infrared (1100 nm) and it is based on the chemical and physical properties of the absorbing species.

The absorption technique, shown schematically in **Figure 2.6**, is used to obtain information about species identity, concentrations, temperatures, film thickness and flow in a gas phase environment [20,21].

Based on Beer-Lambert's law, the absorbance A is calculated via **Equation (2.1)** and is equal to the negative base-ten logarithm of the transmitted light I to the incident light I_0, which is equal to the product of the sample thickness d [cm], the tracer concentration c [mol l^{-1}] and the molar absorptivity ε [l mol^{-1} cm^{-1}]. It is important to note that the molar extinction coefficient ε is an intrinsic absorption property of the tracer at a given wavelength and depends on its chemical composition and structure [22].

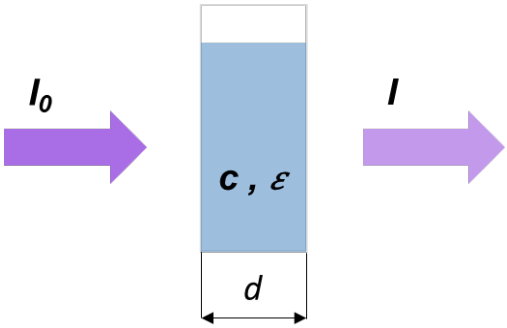

$$A = -\log\left(\frac{I}{I_0}\right) = d\,c\,\varepsilon \qquad (2.1)$$

Figure 2.6. Schematic of light absorption.

Most works in light absorption are on water films. Water has strong absorption bands in the infrared (IR), which can be used to determine the film thickness [23–28]. The thickness of evaporating water films on a heated quartz plate was measured via IR absorption in back-illumination [23]. Non-absorption losses (scattering) were accounted for by adding illumination and detection at a second wavelength for which absorption is low [24,25]. The thickness of water films and droplets on a heated quartz plate after high-pressure injection was imaged by simultaneous tracer LIF and IR absorption [26]. Compared to LIF, absorption is less sensitive to temperature, and it is not sensitive to the presence of oxygen. However, in both techniques, fuel vapor may interfere with the liquid-phase measurement.

Unlike water, most fuels are practically transparent in the easily accessible part of the IR wavelengths regions (and in the visible). However, in aromatic species – naturally present in mineral-oil based fuels or added to fuel surrogates – strongly absorb ultraviolet (UV) light.

The application of the absorption technique begins with the definition of the absorbing tracer and the illumination source to be used. The absorption spectrum of the tracer indicates the wavelength range of the appropriate illumination

source to be used, in which the absorbance is maximum. Absorption of light from a high-speed laser at 266 nm was used to image the fuel-film thickness in a rapid compression machine with GDI, of a toluene-containing fuel [29]. Toluene, which is a fuel derived, has a high absorbance in the UV range between 260 and 270 nm. The fuel composition used in their work (70%-vol. isooctane / 30%-vol. toluene) shows that the tracer concentration is high compared to that used in the LIF technique, where the fluorescent tracer is used in small percentages. Therefore, the tracer concentration is considered to be the main factor affecting the absorption technique. Ideally, in a multi-component fuel surrogate, co-evaporation of the components is desirable. However, the components of the fuel surrogate evaporate preferentially. The components with lower boiling temperatures evaporate first. As a result, the concentration of the tracer varies during evaporation, causing an error in the absorption measurements. The preferential evaporation of any fuel composition should be investigated when using the absorption technique to improve the accuracy of the absorption measurements.

2.3.2 Laser-induced fluorescence (LIF)

Laser induced fluorescence (LIF) is the red-shifted radiative emission after the excitation of an atom or a molecule by laser light that corresponds to the absorption-fluorescence wavelength range of the tracer. The laser light is absorbed by the molecule and causes its excitation from the stable level (ground level) to another excited level. Some of the energy is usually dissipated as vibrational, rotational, and electronic energy prior to any fluorescence or phosphorescence relaxation.

The fluorescence procedure is clarified by the Jablonski diagram, shown in **Figure 2.7** [20], which shows the electronic states of a molecule and the transitions between them. In general, a molecule has two excited states: S1, a singlet state, and T1, a triplet or forbidden state. When the molecule absorbs radiation, it is in an excited level in the singlet state.

If the molecule is in an excited level, it can return to the stable state by emitting fluorescent light (radiative relaxation). It can also return to the nearest excited level by rotation or vibration through internal conversion within the singlet state, facilitated by inelastic collisions between the atoms of the molecule (intramolecular collisions). Collisional quenching, i.e., transfer of electronic energy to another molecule, is another route of de-excitation. A particularly effective quencher is oxygen, with the quenching efficiency depending on pressure and temperature. At this level, the excited molecule can either fluoresce

or transfer to the triplet state via intersystem crossing, followed by phosphorescence, which lasts longer than the fluorescence process [20,30,31].

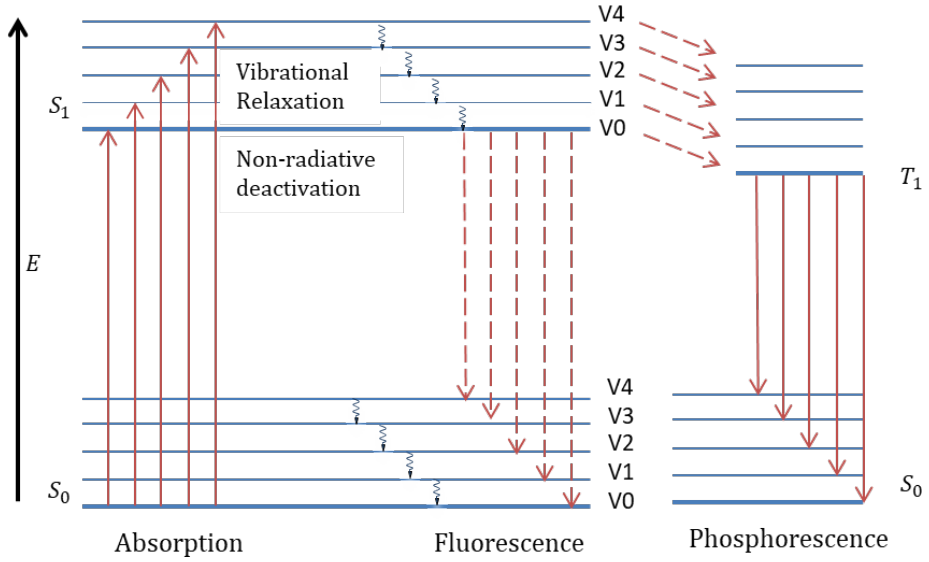

Figure 2.7. Jablonski energy diagram [20].

Equation (2.2) shows the proportionality relationship between fluorescence and absorbance.

$$I_f = \mu \Phi I_a = \mu \Phi I_0 \left(1 - 10^{-h\,c\,\varepsilon}\right) \tag{2.2}$$

where I_f is the fluorescence signal intensity, Φ is the quantum yield, which is the ratio of emitted to absorbed photons, μ is the efficiency of the detection system, and I_a is the absorbed signal intensity. Based on Beer-Lambert's law, I_a can be calculated from the incident signal intensity I_0, the sample thickness h, the tracer concentration c and the molar extinction coefficient ε.

For thin fuel films, weak excitation, and low tracer concentration, the LIF signal is linearly dependent on film thickness [32–36], as shown in **Equation (2.3):**

$$I_f = \mu \Phi I_0 \, h \, c \, \varepsilon \tag{2.3}$$

LIF is commonly used to measure species concentrations, temperature, and flow visualization. LIF has also been frequently used to quantify liquid-film thickness ranging from 5 μm to 1.5 mm as early as 1964 [32]. Typically, a fluorescent marker ("tracer") is added to a non-fluorescent base fuel at a specific concentration to the liquid under study. The physical properties of the tracer determine the wavelength at which it fluoresces. The tracer must also match the physical and chemical properties of the sample. LIF has high sensitivity, but

quantification can be challenging due to the complex photophysics of fluorescence.

The fuel film thickness was measured by Geiler et al. [32] in a DISI engine using LIF. **Figure 2.8** shows the variation of fluorescence intensity as a function of liquid-film thickness for different concentrations of toluene in isooctane. The LIF signal of toluene is non-linearly dependent on the tracer concentration.

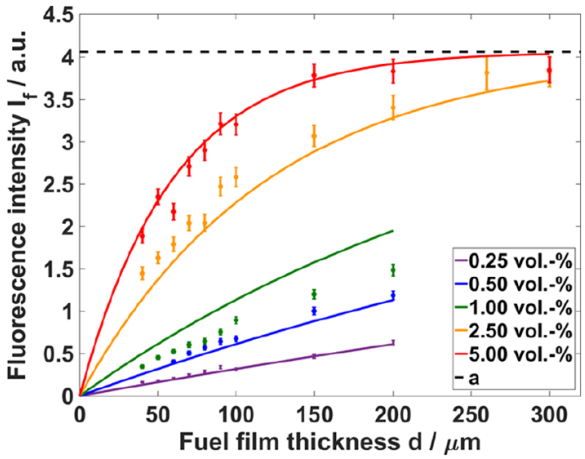

Figure 2.8. Variation of fluorescence intensity as a function of liquid-film thickness for different concentrations of toluene in isooctane [32].

They found a moderate dependence of fluorescence intensity on pressure but a significant dependence on temperature [32]. **Figure 2.9** shows the temperature dependence of the fluorescence of toluene and 3-pentanone, normalized to the fluorescence values at room temperature. The fluorescence intensity decreases with increasing temperature, but much more so for toluene.

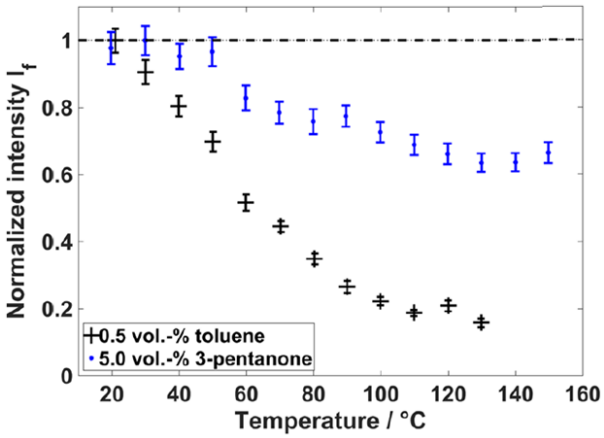

Figure 2.9. Temperature dependence at 14 bar of toluene and 3-pentanone fluorescence normalized to fluorescence values at room temperature [32].

In addition, dissolved oxygen was found to quench the fluorescence in the liquid fuel [32,37]. These dependencies on often unknown parameters make quantitative measurements challenging.

To some extent, varying thermodynamic conditions perturb the non-radiative energy deactivation. Therefore, the quantum yield is highly dependent on the thermodynamic conditions. The fluorescence intensity, which is supposed to be proportional to the quantum yield, is no longer directly related to the liquid-film thickness. For example, Ghandi et al. [38] found that the assumption of a constant quantum yield resulted in a 50% error in the fluorescence intensity of ketones.

Another problem is photobleaching. In theory, a tracer is supposed to fluoresce indefinitely, but in reality, this is often not the case. The structural instability of the tracer during the excitation lifetime makes it susceptible to degradation. Long duration and high-intensity illumination can cause the fluorescent tracer to change its structure. In fact, even in the presence of the required illumination, the tracer is no longer promoted to the excited state and can no longer fluoresce. In LIF, photobleaching can cause a decrease in the fluorescence intensity over time, resulting in a biased distribution of the film thickness.

LIF is also subject to variations in the pulsed laser light used. The pulsed laser mode is not stable in terms of energy, frequency, and pulse duration. In fact, the variation of the pulsed laser energy is a critical factor in quantitative LIF measurements. An energy monitor can be added to the optical setup for subsequent correction of the LIF signal.

Among the techniques for measuring the thickness of a liquid film, LIF is the most frequently used due to its high sensitivity, but it is nevertheless accompanied by several problems and challenges, especially with respect to thermodynamic dependencies. In LIF, the fluorescent tracer is typically used in small amounts, typically 0.1 to 2% of the fuel surrogate composition. The remaining fuel components must be optically transparent at the wavelengths used so that absorption and emission are related only to the fluorescent tracer. For example, conventional fuels cannot be used for quantitative LIF film thickness measurements. These fuels are characterized by a high aromatic composition resulting in too much absorption.

2.3.3 Refractive Index Matching (RIM)

Refractive index matching (RIM), first developed by Drake et al. [5], allows imaging the liquid film thickness deposited on an illuminated, roughened

material surface. The variation in the scattered light between dry and wet surfaces is related to the fuel film thickness [5,39–42].

RIM proper is applicable only to transparent surfaces, but variations for opaque, reflective surfaces, e.g., rough metal, have been developed [43]. The main strengths of RIM are that it works for any fuel and is not affected by ambient conditions of temperature and pressure. However, the surface needs to be dry before the measurement, and the presence of any residue from a previous experiment decreases the measurement accuracy. For each surface roughness, film thicknesses can be measured only in a limited range.

Figure 2.10 shows a typical RIM optical setup [42]. The setup consists mainly of three elements: a light source with an illumination angle large enough to avoid reflections at the liquid-vapor medium [41], a roughened surface, and a detector (e.g., a high-speed camera). The reduction in the scattered light between dry and wet surfaces, ΔI, is expressed in **Equation (2.4)**.

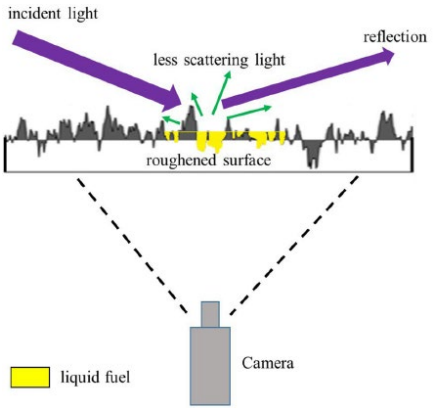

$$\Delta I(x,y) = \frac{I_{dry}(x,y) - I_{wet}(x,y)}{I_{dry}(x,y)} \tag{2.4}$$

Figure 2.10. Typical RIM optical setup [42].

where I_{dry} is the scattered light intensity without a liquid film and I_{wet} is the scattered light intensity with a liquid-film.

The liquid film thickness d at a position (x,y) is then calculated as a function f of $\Delta I(x,y)$ through an appropriate calibration:

$$d(x,y) = f(\Delta I(x,y))$$

2.4 Optical diagnostics for soot measurement

Since soot formation is the very reason that fuel films are of interest in an engine context, and soot absorbs (and scatters) broadband, it is to be expected that in particular line-of-sight integrated measurements suffer from interference by soot.

On the other hand, the soot near films is of immanent interest. Typical optical diagnostics for soot use light extinction, elastic light scattering, and laser induced incandescence (LII) [15,16]. In this chapter, a brief overview of the most commonly used soot measurement techniques in the literature is presented.

2.4.1 Extinction techniques

Light extinction

Light extinction is an optical diagnostic for soot mass fraction calculation. **Figure 2.11** shows a schematic of the light extinction technique used for soot measurement. It is a line-of-sight diagnostics that accounts for the attenuation of collimated light after passing through a soot cloud. Light extinction is a technique based on the Beer-Lambert law, where the soot optical density (KL) can be calculated from the ratio of transmitted to incident intensities via **Equation (2.5)**.

$$\frac{I}{I_0} = e^{-KL} \tag{2.5}$$

where I_0 is the incident light intensity, I is the transmitted light intensity through the soot cloud, K is the extinction coefficient, and L is the path length of the soot cloud.

KL is proportional to the mass fraction of soot along the line-of-sight [44]. From the extinction coefficient K, soot mass fraction f_v can be calculated via **Equation (2.6)**.

$$f_v = \frac{\lambda}{k_e}.K \tag{2.6}$$

Where λ is the illumination wavelength and k_e is the dimensionless optical extinction coefficient.

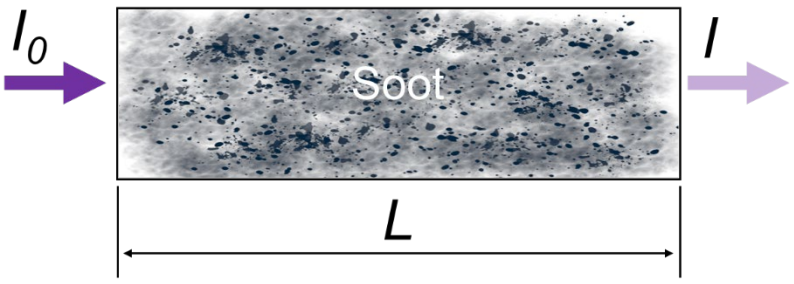

Figure 2.11. Schematic of the principle of light extinction technique.

Diffused back illumination (DBI)

The diffused back-illumination (DBI) technique is a line-of-sight light-extinction based technique. The principle of the DBI technique is similar to the light extinction technique but with the use of a diffused light source instead of a collimated light source. In the light extinction technique, beam steering by index-of-refraction gradients degrades the accuracy of the imaging measurements. This can be mitigated by the DBI technique [45,46].

In light extinction based techniques, coefficient of soot is dependent on soot maturity and wavelength [15,16]. Polycyclic aromatic hydrocarbons (PAHs), which are soot precursors, also absorb light. Distinguishing between PAHs and soot becomes difficult, especially at shorter wavelengths where PAHs have high light absorbance.

2.4.2 Laser Induced Incandescence (LII)

In laser induced incandescence (LII), a high-power laser with short duration pulses (nanosecond order) heats soot particles to more than 4000 K to the point of sublimation. This temperature is much higher than the average soot temperature, which is around 2000 K. The resulting incandescence is observed, enabling the detection of soot point-wise or two dimensionally. LII can be used for both qualitative and quantitative soot measurements.

The LII signal increases rapidly for about 10 ns due to the heating of the soot particles by the laser pulses. The signal then begins to decrease slowly for about 100 ns as the soot particles begin to cool by thermal conduction to the surrounding gas, sublimation and radiative emission [47]. **Figure 2.12** shows a schematic of the energy balance in the LII technique. With sufficient laser fluence, the soot volume fraction (f_v) is roughly proportional to the LII signal as shown in **Equation (2.7)**.

$$f_v = \alpha I_{LII} \tag{2.7}$$

where f_v is the soot volume fraction, I_{LII} is the LII signal and α is the proportionality factor. The spatial distribution of the soot mass fraction was measured in a GDI engine using a combination of LII and light extinction after calibration of the LII signal and determination of α [47]. Niklas et al. used LIF and LII to study the formation of PAH and soot, respectively, near evaporating fuel films in a constant flow facility. PAH and soot were seen in intermittent filaments, some very close to the evaporating films [48,49].

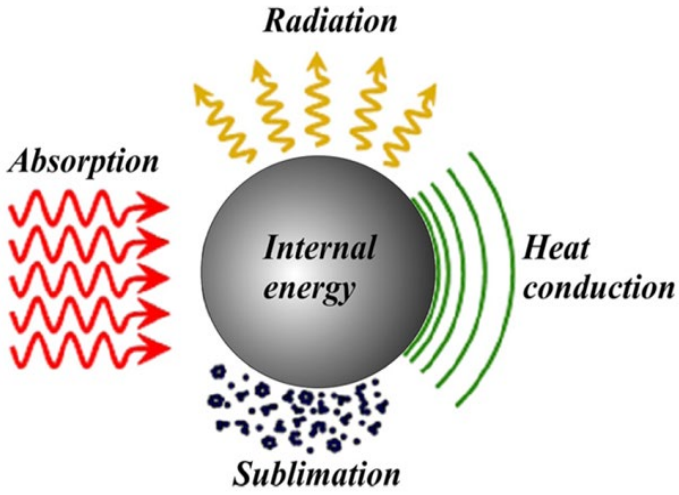

Figure 2.12. Schematic of the LII energy balance [50].

LII is dependent on laser fluence (the energy delivered by a laser pulse per unit area), which in turn affects the heating and incandescence of soot particles. In LII, the laser pulses heat the soot particles to a high temperature, resulting in rapid soot decomposition. This affects the local bath gas temperatures, which also affects both the spectral intensity and the temporal evolution of the LII signal. Soot present outside the measurement area can absorb the LII signal. Unwanted excitation and fluorescence from any species can affect the accuracy of this technique [18,51].

2.5 Optical diagnostics for the experiments

For liquid fuel-film thickness measurements, the absorption technique was used in our experiments. Compared to LIF imaging, the absorption technique has the advantage that the underlying photophysics of absorption are much simpler than those of fluorescence. Broadband UV absorption is not affected by pressure or oxygen quenching. It could be dependent on temperature, but in the case of toluene, our measurements showed this to be not significant over the relevant temperature range. However, in LIF, fluorescence quenching by oxygen can help to suppress signal from fuel vapor, which is one of the chief interferences in absorption imaging. In our study, the absorption imaging uses inexpensive LEDs that can be pulsed at very high repetition rates, while all documented LIF fuel-film imaging is based on laser illumination.

Both LIF and UV absorption require a fuel with aromatic content, but at different concentrations - much lower for LIF. The high aromatic content of the fuel surrogate used in the absorption technique is more representative of the gasoline fuel composition. However, preferential evaporation is more important in the

absorption technique than in the LIF technique, where the tracer concentration in the fuel mixture is higher than in the LIF technique. For any fuel surrogate composition, the error of preferential evaporation on the absorption measurements must be investigated.

Concerning RIM, it is not affected by ambient conditions and can be performed with nearly any fuel, but it is quite dependent on the roughness of the substrate surface. The presence of any liquid residues or soot deposits remaining on the surface can affect the accuracy of the technique. No tracer has to be added. This technique can be employed with commercial fuels.

In all three techniques, film-surface scattering, soot incandescence, and extinction by soot and soot precursors potentially interfere with the thickness measurement, depending on the exact implementation. In our work at UDE, a UV-vis absorption technique was developed to distinguish and correct these contributions. In its current implementation, the absorption technique requires optical access from two opposite sides of the film, but a configuration for reflection imaging may also be possible [25].

For soot measurements, DBI technique was chosen in our study. It is a non-intrusive technique that provides direct -but only line-of-sight integrated- imaging of the spatial distribution and morphology of soot particles. LII provides local information on soot properties in the region illuminated by the laser but is more complex and harder to implement with high repetition rates. In DBI technique, the beam steering encountered in other extinction-based techniques is mitigated by using diffused light illumination. However, for quantitative measurements of soot mass fraction, uncertainties resulting from assumptions about soot properties must be considered in DBI technique [52].

2.6 UV-absorption light sources

There are several sources of UV illumination on the market, such as lasers, light-emitting diodes (LEDs) and lamps [22]. Most UV lamps, such as deuterium, mercury, and xenon arcs, are not widely used in optical diagnostics because they have low power and slow warm-up. In addition to that, they show degradation at low temperatures, and some may contain toxic elements like mercury [53]. Nd:YAG lasers are the most common UV-light source used in optical diagnostics applications. They have high output power, spatial and temporal coherence, and a very narrow bandwidth emission spectrum. In our UV-absorption application, evaporation and burning of fuel-films occurs at kHz speeds. A “high-speed” Nd:YAG laser provides a high-speed UV-absorption imaging but is quite

expensive. However, less expensive “low-speed” lasers (at Hz rates) allow only a single temporal acquisition of the fuel-films per repetition.

Fluorescence technique depends on many factors such as quantum yield, detection system efficiency and absorbed light intensity. The energy of the fluorescence emission is lower than the absorbed energy due to energy losses such as vibrational relaxation. In addition, the fluorescence emission is detected at a different angle to the illumination source. A higher intensity illumination source is required to stimulate as much fluorescence emission as possible. In the absorption technique, the measurement is based on the attenuation of light as it passes through the sample. Since the absorption is calculated from the ratio of transmitted to incident light, a low power illumination source can be used. The current work is based on the absorption technique. Inexpensive LEDs can therefore be used instead of the Nd:YAG lasers, which are typically used in fluorescence applications. LEDs are a cheap and easy to handle UV light source compared to lasers. They have sufficient power, high modulation frequencies, low noise, and a spectral and spatial power distribution with a Lambertian profile [54].

3 State of the art

This chapter presents a state of the art on the liquid fuel-film formation after direct injection and the interaction between the deposited liquid fuel-films and the premixed flame that causes soot emissions inside GDI engines. The mechanisms of liquid fuel-film formation, evaporation, interaction between liquid fuel-films and premixed flame, and soot formation in GDI engines as found in the literature are presented.

3.1 Formation of fuel films in GDI engines

During direct injection, the fuel that is not evaporated impinges on the internal surfaces of the combustion chamber. The injector sprays liquid fuel into the cylinder at high pressure. This causes the spray to atomize into a combination of liquid-fuel droplets and fuel vapor. The liquid fuel droplets mix with the hot gases in the chamber and evaporate. However, the remaining unevaporated spray impinges the cylinder walls and piston.

Fuel film formation depends on many factors such as wall temperature, injection pressure, injection timing, combustion chamber aerodynamics, and other physical and chemical conditions. Payri et al. [55] studied Spray-G-injector injection in a constant volume cell. Liquid fuel penetration, spray angle and morphology and vaporization were affected by cell density, temperature, injection pressure inside the chamber, and by spray collapse, which also affected spray mixing and evaporation behaviors.

Flash boiling, cavitation, and spray collapse are possible phenomena encountered during injection [55–57]. Flash boiling occurs when the local fuel pressure drops below the vapor pressure, which makes the fuel superheated and produces vapor and bubbles [58]. Under flash boiling conditions, evaporation and bubble production increase within the spray cone, while pressure decreases, resulting in a small cone angle, known as ‘‘spray collapse’’. On the one hand, flash boiling increases spray evaporation and reduces droplet size. However, on the other hand, the reduced spray cone angle reduces the contact of the droplets with the outside air, which reduces the evaporation of the remaining liquid fuel droplets inside the spray cone, causing liquid fuel-film deposits on the internal surfaces of the cylinder. Schulz et al. [57] found that at high fuel temperature, fuel spray collapse increases, and the mass of the remaining fuel film accumulates on the surface using infrared thermometry. Payri et al. [55] visualized an increase in spray collapse at high density and temperature, and an increase in spray penetration at high injection pressure.

Numerical codes for 3D-flow and combustion simulation were developed for studying fuel-film formation. **Figure 3.1** shows a schematic of impingement regimes of a droplet impacting a wall surface adopted in these codes. Four regimes are shown here: stick, spread, rebound, and splash [59].

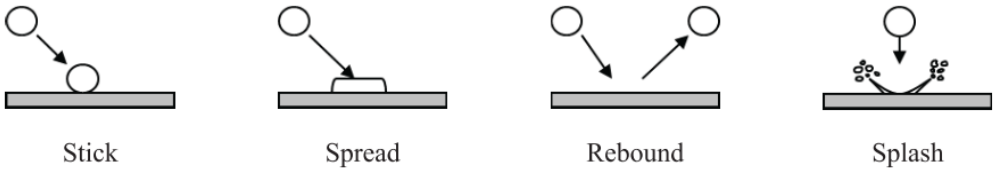

Figure 3.1. Schematic of impingement regimes when a droplet impacts a surface [59].

After injection, the deposited liquid fuel is entrained on the surfaces towards the edge of the fuel film. Xueong et al. [60] studied the entrainment of the fuel pattern on a controlled heated plate and calculated the liquid fuel-film thickness using the refractive index matching (RIM) technique, shown in **Section 2.3.3**. They divided the development of the liquid fuel-film on a surface into three steps: wave propagation, spread, and breakup, as shown in **Figure 3.2** [60].

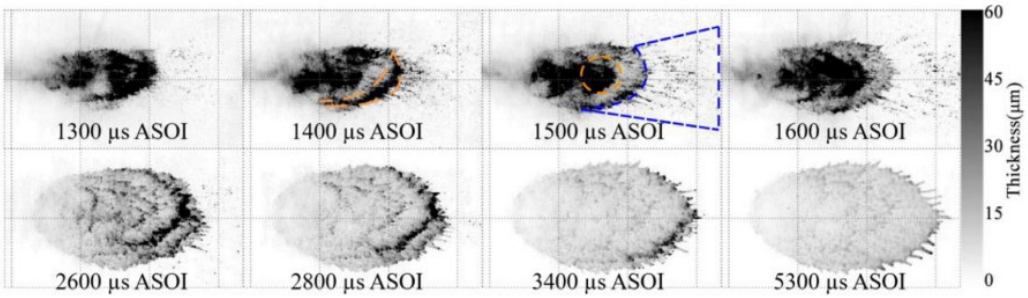

Figure 3.2. Liquid film developments by Xueong et al. at a plate temperature = 20°C. The first row of figures shows liquid wave propagation and breakup with co-flow air induced by the spray. The second row of figures shows liquid wave propagation and fuel film spreading on the surface without breakup [60].

The evaporation rate of the liquid fuel-film deposited on a wall exhibits a non-monotonic dependence on the wall temperature. **Figure 3.3** shows different evaporation regimes in which the liquid film evaporates and reacts differently, from liquid film evaporation to nucleate boiling, transition boiling and film boiling [61]. Before the saturation temperature is reached, the evaporation rate increases with temperature. However, at temperatures above the saturation temperature, this trend changes: the evaporation rate increases or decreases depending on the wall temperature and the evaporation regime.

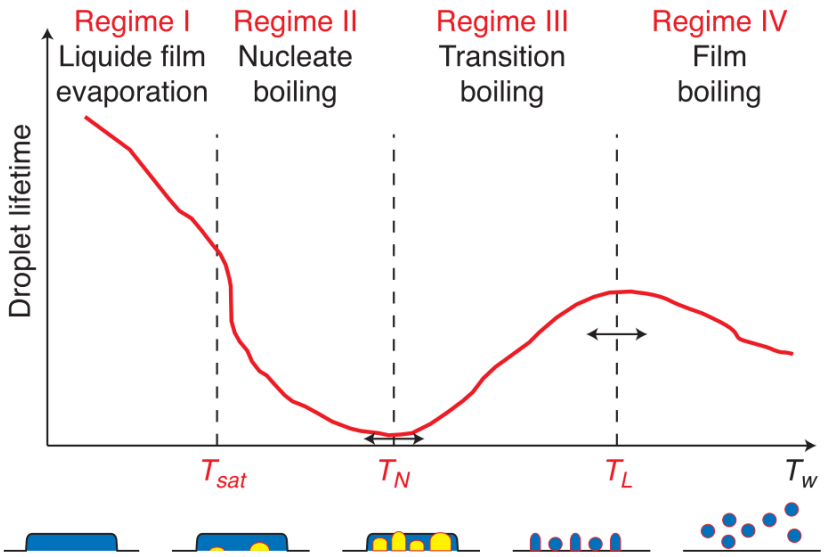

Figure 3.3. Droplet lifetime curve and schematics illustrating the boiling states near the limits of the boiling regimes [61].

In a DISI engine, Drake et al. [5] found soot formation from fuel-rich zones that formed after ignition from liquid fuel films. Numerous experiments in optical engines have validated the formation of the fuel film on the internal cylinder surfaces after direct injection. Stevens et al. [6] studied piston wetting in an optical engine using the LIF technique. **Figure 3.4**a (side and top views) shows the spray impinging the upper surface of the piston during the compression stroke. The liquid fuel accumulated near the center before ignition. After several firing cycles, the presence of liquid fuel films on the piston caused black carbon deposits, as shown in **Figure 3.4**b [6].

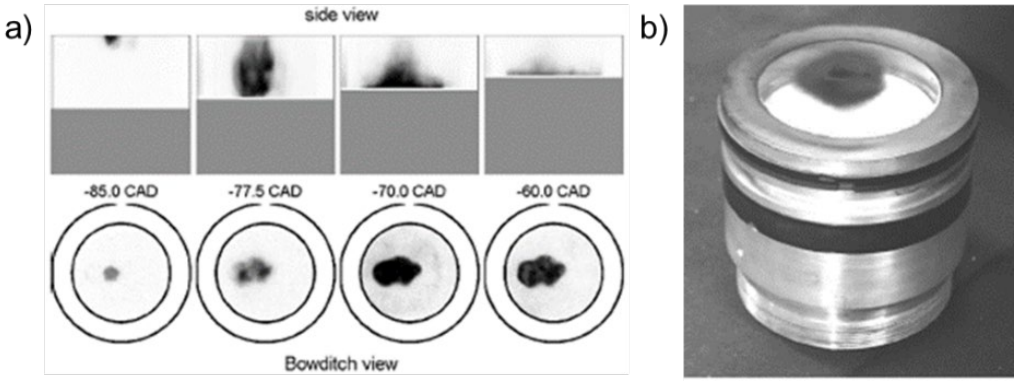

Figure 3.4. Spray impingement on (a) the piston head, and (b) soot deposit in a late injection firing cycle [6].

Previous studies in our own research group used LIF to image GDI fuel film formation on a quartz plate placed inside a constant volume cell. Liquid fuel-film

formation was qualitatively assessed in an optical engine using a five-hole injector. **Figure 3.5** shows the detection of fluorescent liquid fuel-films on (a) the piston head as well as on (b) the cylinder walls. Pilla et al. found that spray targeting, injection pressure, multi-injection strategy, and in-cylinder aerodynamics affected the fuel film formation [12,62]. Bardi et al. [63] qualitatively assessed the fuel film formation in an optical engine at cold-start conditions (T_{wall} = 30°C and 80°C), and detected liquid fuel on the valve seat, the injector nozzle, the top of the piston, and the cylinder walls. **Figure 3.6** shows fluorescence images at different crank angles and wall temperatures of (a) 30°C and (b) 85°C, captured from the bottom of the piston [63].

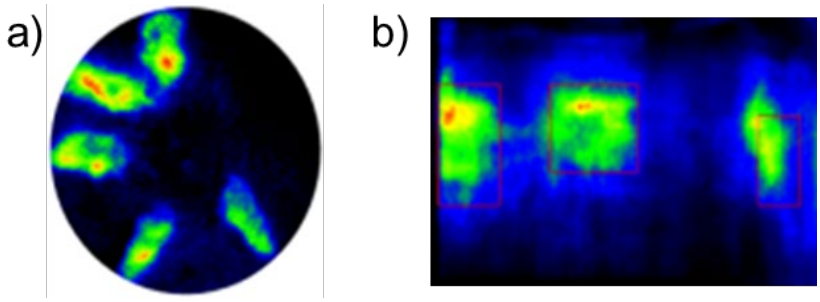

Figure 3.5. Fuel film on (a) the top of the piston and (b) the internal surfaces of the cylinder [62].

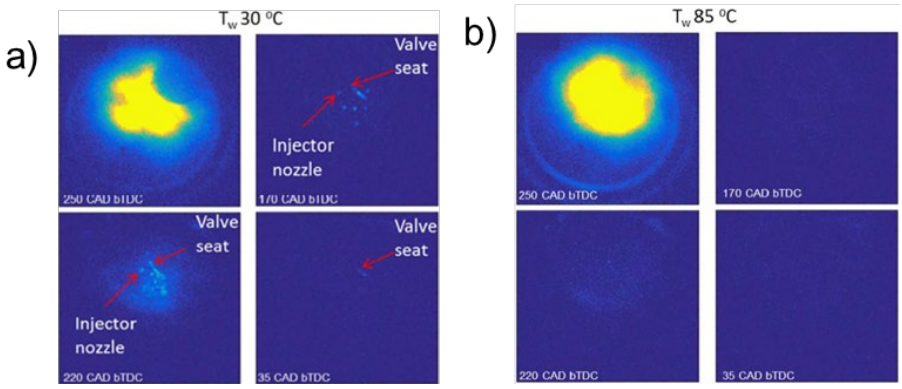

Figure 3.6. Liquid fuel-film detection at (a) 30°C and (b) 85°C (using LIF technique) [63].

3.2 Fuel film evaporation and combustion

Prior to the combustion phase, the deposited liquid fuel-films begin to evaporate before the arrival of the premixed flame, which interacts with the remaining unevaporated liquid fuel-films present on the wall, causing soot formation. Ketterer et al. [17] proposed a conceptual model describing soot formation due to the interaction between liquid fuel-films and the premixed flame in GDI engines under cold-start conditions. **Figure 3.7** shows the four steps of the proposed

fuel/flame interaction model. After injection, liquid fuel-films are deposited on the wall (**Figure 3.7**a). After ignition, the premixed flame propagates inside the combustion chamber. Evaporation of the deposited liquid fuel-film creates a rich zone of vapor cloud surrounding the liquid surface (**Figure 3.7**b).

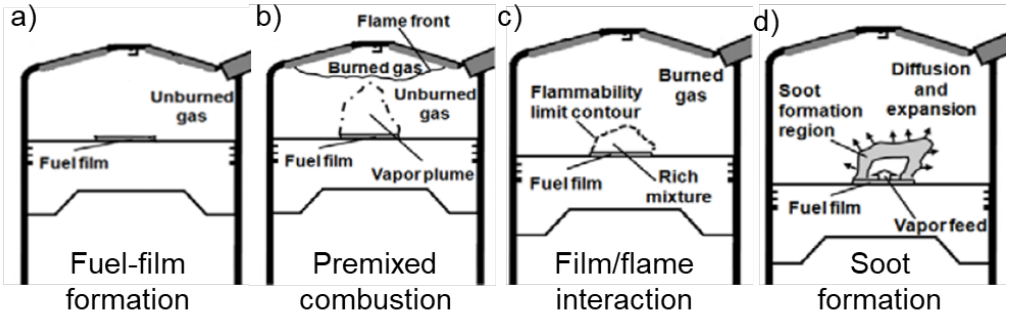

Figure 3.7. Conceptual model of fuel film-premixed flame interaction [17].

Since GDI engines operate in a stoichiometric combustion mode, most of the oxygen present in the combustion chamber is consumed during the propagation of the premixed flame from the top of the cylinder towards the piston head where the liquid fuel-films are deposited. After reaching the wall, the premixed flame interacts with the fuel vapor, generated by the evaporation of the liquid fuel-film, which burns in a rich operating mode accompanied by a high soot formation (**Figure 3.7**c). Despite the presence of oxygen inside the combustion chamber during flame propagation, the continuous evaporation of the liquid fuel film produces rich fuel vapor zones. In their model, they suggested that heat conduction from the burned gases to the vapor cloud above the liquid fuel-films increases the temperature of the rich mixture and contributes to soot emissions under thermal pyrolysis. Temperatures near the wall increase by conduction, causing more liquid fuel to evaporate and burn, producing more soot emissions (**Figure 3.7**d) [17].

Fuel film formation was studied in a constant-flow facility using LIF. **Figure 3.8** shows the corresponding ensemble averages of soot LII images [33]. This figure shows that the persistence of the fuel film after combustion causes soot formation close to the wall. Fuel vapor mainly emerges from deposited fuel films. The hot gases mix with the evaporated liquid fuel films and that leads to soot formation.

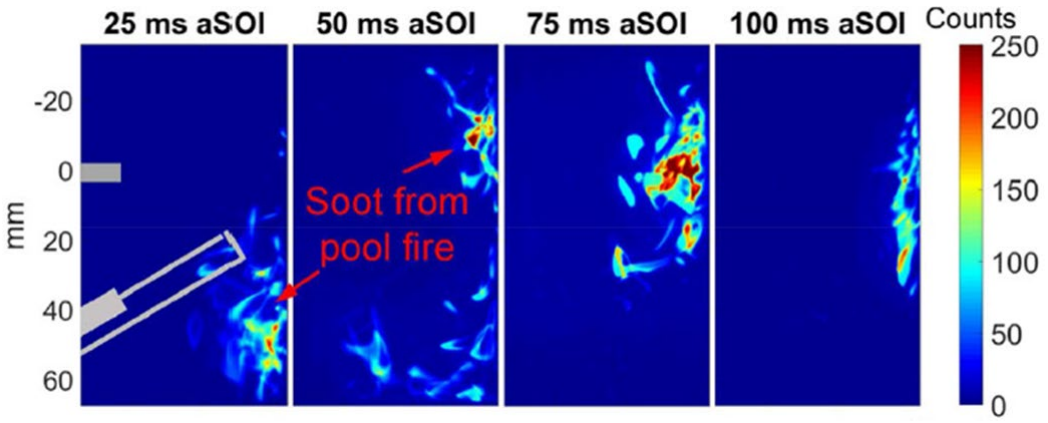

Figure 3.8. Ensemble averages of soot LII images showing soot formation close to the wall [33].

The evaporation of liquid films was also studied in a constant volume cell at different plate temperatures [64]. Fuel-rich vapor regions close to the plate were produced at temperatures below 200°C and caused soot formation.

In this work, the interaction between the premixed flame and the deposited liquid fuel-films was studied by measuring the fuel-film thickness and soot extinction in different experimental environments and at different experimental conditions.

DBI for soot measurement

This technique was originally developed for spray measurements [65] and later adopted for soot mass fraction measurements [44,66,67]. Ghandhi and Heim [68] used the light extinction technique for soot measurement. They worked on the quality of the collimated light and its transmission to the region of interest. However, under harsh conditions of pressure and temperature, collimated light is not the right illumination source to reduce beam steering issues encountered in extinction-based techniques. Collimated light is deflected away from the collector due to refractive index gradients, resulting in an overestimation of the soot mass fraction [44,46].

To reduce beam steering, Nakakita et al. [45] demonstrated the importance of using a diffused light instead of a collimated light. An engineered diffuser was used to diffuse collimated light at a specific angle with a Lambertian intensity profile [69]. An optical setup was designed to cope with harsh conditions. **Figure 3.9** shows an example of a DBI optical setup that includes the parameters of **Equation (3.1)** to mitigate the effect of beam steering [18,46,70].

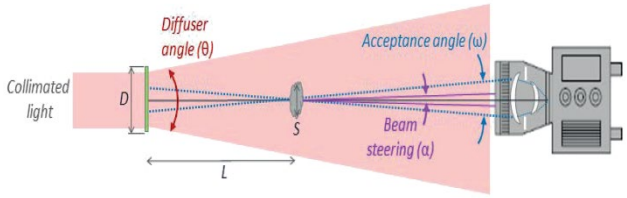

$$\Theta \geq \alpha + \omega \tag{3.1}$$

$$D \geq S + \tan(\alpha + \omega)\, L$$

Figure 3.9. Example of a DBI optical setup with the parameters of Equation (3.1) [18].

Where θ is the diffuser angle, α is the beam steering angle, ω is the acceptance angle of the camera objective, D is the diameter of the diffuser, S is the size of the probe volume, and L is the distance between the diffuser and the probe.

4 Materials and methods

In this chapter, we present the experimental methods used to assess the fuel-films formation and evaporation, and the interaction between the fuel-films and the premixed-flame. The experimental conditions, as well as the experimental setups, will be presented in this chapter. UV-visible absorption and DBI techniques were used to determine the liquid fuel-film thickness and soot extinction, respectively. The experiments were caried out in two thermodynamically-controlled environments: a pressure-controlled constant-volume cell at IFPEN and an atmospheric-pressure constant-flow facility at UDE. Tests were performed under non-reacting and reacting conditions. In addition, an experiment was designed to investigate the effect of preferential evaporation on the film thickness measurement uncertainty and it is presented at the end of this chapter. Parts of this chapter were published by Shway et al. [71,72], in particular **sections 4.1.1**, **4.1.3**, **4.1.4**, **4.2**, and **4.4**.

4.1 Constant-volume cell experiments

4.1.1 Optics and experiments

The experiments were carried out in a constant-volume cell at IFPEN [44,73]. The cell features a near quiescent gas volume of which temperature and pressure conditions can be controlled accurately. For a target pre-mixture gas density and equivalence ratio, the control system introduces gases at specific partial pressures. The initial temperature of the bath gases is controlled by the cell wall heating. Fuel temperature is also controlled using an external cooling system. The temperature of the injector tip is measured for the different coolant temperatures by means of a dummy injector [73]. The cell has a volume of 1.3 L, and four optical windows of 80 mm diameter. The fuel films that are investigated here are formed by the spray plumes injected at 200 bar, impacting onto a transparent plate positioned 30 mm below the tip of the injector. The plate is made of quartz, having an excellent transmittance in the UV spectral range, a high thermal shock resistance, and excellent mechanical properties under elevated temperatures. The impact surface is perpendicular to the injector axis, a configuration similar to that found in most GDI engines.

Under non-reacting conditions, only N_2 was introduced into the cell. Under reacting conditions, the premixture bath gases, consisting of C_2H_2, H_2, O_2 and N_2, were introduced. The experimental layout and the experimental conditions are shown in **Figure 4.1**. The spray-wall impact configuration, described in the steps below, is shown in **Figure 4.2**.

1. Filling: The vessel was sequentially filled with the ignitable mixture, consisting of hydrogen (H_2), acetylene (C_2H_2), nitrogen (N_2) and oxygen (O_2). The pressure and temperature of the mixture at the end of the filling process define its density. The proportions of the gases are controlled during the filling process: the gases are introduced sequentially, controlling the pressure increment related to each gas which is equivalent to their partial pressures. The proportions between N_2 and O_2 are set to obtain the desired O_2 fraction after the pre-combustion event [44], the gases are mixed with a fan stirrer during 30 seconds after the end of the gases introduction.
2. Injection: When the desired pressure is reached, the injection of the surrogate fuel is triggered, with the fan off. A reference fuel surrogate consisting of 70% isooctane - 30% toluene was used.
3. Premixed combustion: After fuel injection, a spark plug was used to ignite the mixture. The premixed flame propagates from the spark plug towards the quartz plate and interacts with the deposited fuel film.
4. Film/flame interaction: the flame interacts with the liquid fuel and nearby fuel-rich regions, and soot is eventually produced.

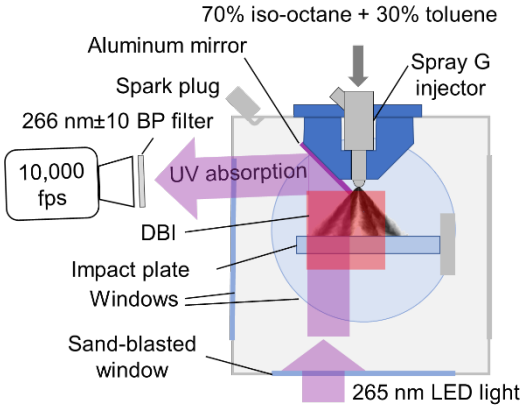

Injector	Spray G AV67 – 022 [74] 8-hole injector
Fuel surrogate	30% toluene + 70% iso-octane
p_{cell}	0.5, 1, 6 bar
T_{wall}	50, 100, 150, 200°C
$p_{injection}$	200 bar
T_{fuel}	90°C
$t_{injection}$	0.78 ms

Figure 4.1. (left) Schematic of the constant volume cell and the imaging optics, and (right) a summary of the experimental conditions.

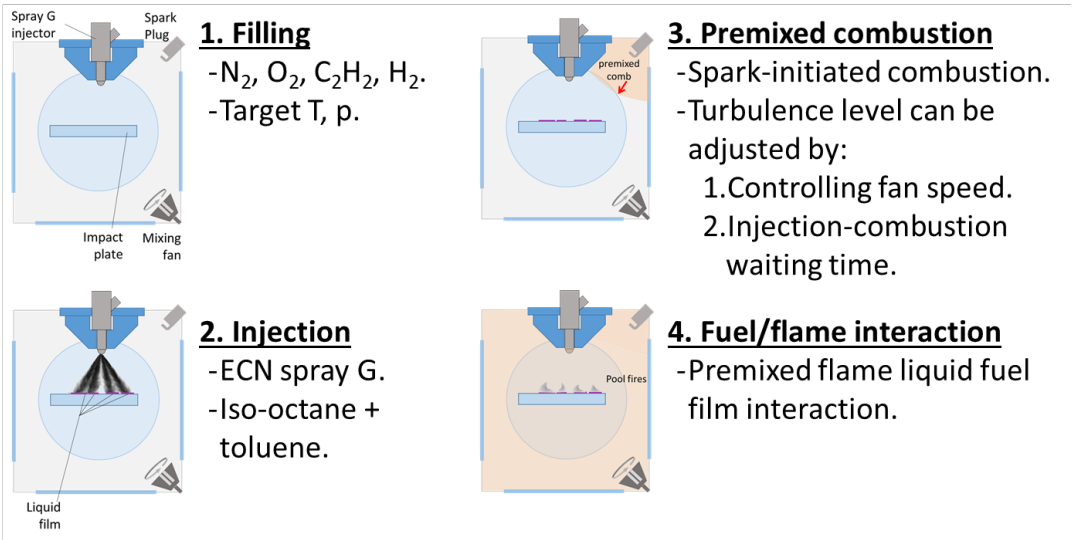

Figure 4.2. Spray wall impact configuration in the constant volume cell.

The injector used in these experiments, shown in **Figure 4.3** (top), is an eight-hole spray G injector developed by Delphi for the Engine Combustion Network (ECN). The specifications of the injector are provided on ECN webpage [74] and are summarized in **Figure 4.3** (bottom).

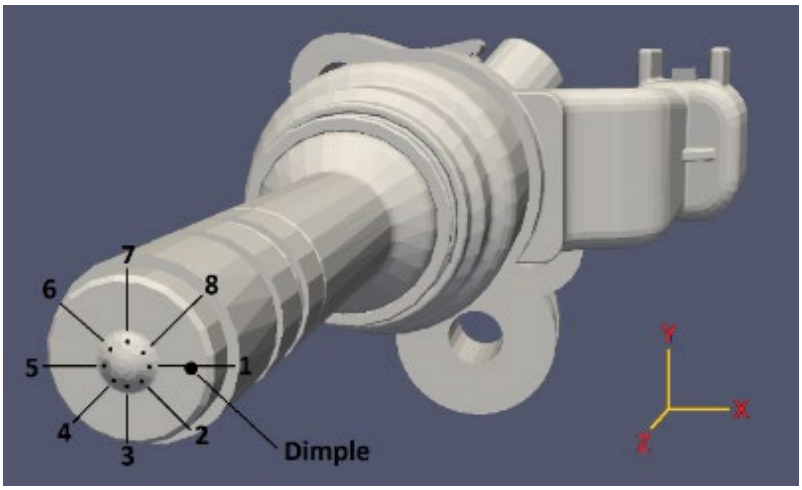

Number of holes	8
Spray Shape	circular
Bend Angle	0°
L/D ratio	1.4
Hole shape	straight
Manufacturing	EDM
Flow rate	15 cc/s @10 MPa
Fuel injector	Delphi solenoid-activated
Nozzle type	Valve-covered orifice (VCO)

Nozzle shape	Step hole
Orifice diameter	0.165 mm specification (0.170 mm measured)
Orifice length	0.16-0.18 mm
Step diameter	0.388 mm specification
Orifice drill angle	37° relative to nozzle axis
Full outer spray angle	80°

Figure 4.3. (top) 3D configuration of a spray G injector [74] and (bottom) spray G injector specifications [74].

4.1.2 Residual oxygen excess

As described above, the combustible gas-mixture consisting of C_2H_2, H_2, O_2 and N_2 is introduced into the constant-volume cell at defined gas partial pressures for a target cell density. The residual oxygen excess and partial pressures are first set in the software that operates the cell. The combustible gas-mixture is ignited with a spark plug, creating a high-temperature, high-pressure environment in the cell.

The equation for the premixed combustion of the pre-ignitable gas mixture that takes place in the cell is as follows:

$$3C_2H_2 + 0.5H_2 + \alpha O_2 + \beta N_2 \rightarrow 6CO_2 + 3.5H_2O + \beta N_2 + \zeta O_2 \quad (4.1)$$

Where α and β are the oxygen and nitrogen compositions of the reactants, respectively. ζ is the residual oxygen excess remaining in the cell after combustion of the gas-mixture.

The constant volume cell at IFPEN has been frequently used for premixed combustion applications. In our study, the premixed combustion is used for a gasoline direct injection application. After the introduction of the combustible gas mixture to the constant volume cell, ignition and injection of the fuel surrogate are synchronized to start simultaneously. Inside the cell, the combustible gas-mixture is mixed with a fan installed inside the cell for 60 seconds. The fuel surrogate is either injected immediately and the gas-mixture is ignited (case with a fan, turbulent conditions) or injected 60 seconds after the gas mixing is completed (case without a fan, non-turbulent conditions). The premixed flame propagates inside the cell consuming the combustible-gas mixture and the evaporated fuel-surrogate.

Here, the evaporated fuel surrogate is one of the reactants in the premixed combustion equation. Therefore, ζ, which is initially defined in the cell software and represented in **Equation (4.1)**, does not represent the actual residual oxygen excess present above the plate during the premixed-flame fuel-film interaction.

Therefore, a different residual oxygen excess ζ_{fuel} can be deduced if we take the evaporated fuel-surrogate into account in the premixed-combustion equation. Since the percentage of evaporated fuel-surrogate is not known yet for the calculation of ζ_{fuel}, we assumed that the fuel surrogate was completely evaporated. The fuel surrogate, used in the IFPEN experiments and consisting of 70% iso-octane and 30% toluene, was then represented by the empirical formula $C_{7.16}H_{13.97}$ in the following premixed-combustion equation:

$$3C_2H_2 + 0.5H_2 + \alpha O_2 + \beta N_2 + \gamma\,(C_{7.16}H_{13.97}) \rightarrow 6CO_2 + 3.5H_2O + \beta N_2 + \zeta_{fuel}O_2 \qquad (4.2)$$

Under reacting conditions, two experimental conditions at $p = 1$ bar and $T = 100$°C were tested with two residual oxygen excesses $\zeta = 2\%$ and $\zeta = 15\%$ corresponding to $\zeta_{fuel} = 0\%$ and $\zeta_{fuel} = 13\%$, respectively. The first case corresponds to stoichiometric premixed combustion where all oxygen is consumed by the premixed flame. The second case corresponds to a lean combustion.

4.1.3 Optics and experiments

A UV absorption technique was used to measure the liquid fuel film thickness. The absorbing species used in the fuel surrogate is toluene. Fuel surrogate composition and components' physical properties are presented in **section 4.3**. The choice of the illumination source was based on the fact that toluene has a strong light absorption at wavelengths below about 270 nm. The molar absorptivity of toluene is shown in **Figure 4.4**.

The main spectral features of the UV LED chosen for this work and toluene UV absorption, measured with a fibre-pickup spectrometer (Ocean Optics USB 2000+) and a UV-visible spectrophotometer (Varian Cary 400 Scan), respectively, are shown in **Figure 4.4.** A schematic of the UV absorption optical setup is shown in **Figure 4.1**. A LED array (OLM-046A-c, made by OSA Opto Light) emits UV light at 268 nm center wavelength (CWL) with a full width at half maximum (FWHM) of 15 nm. The hexagonal-shaped array is shown in **Figure 4.4**. It has 72 LEDs (OSA) arranged under an array of parabolic reflectors that deliver the light at a narrow angle, a total optical power of 2 W, an emission angle of 25°, and was applied in continuous mode. The incident light was diffused by a sandblasted sapphire window installed in the bottom of the cell. After passing through the quartz plate and the liquid fuel films, the transmitted light was then directed to the detection system by a mirror installed inside the cell. The mirror is made of aluminum. Aluminum reflects UV light and has a high resistance to heat.

Figure 4.4. Image of the LED array (OLM-046A-c, made by OSA Opto Light), at 268 nm CWL with 15 nm FWHM of 15 nm, used as a source of UV illumination.

A metal window was installed on one of the four sides of the cell to hold the mirror and the quartz plate. The other three windows were made of sapphire. An injector holder was manufactured so that the part of the holder inside the constant volume cell was as close as possible to the back-side of the mirror to avoid any interference between the spray and the mirror. A band pass filter (CWL 266 nm, FWHM 20 nm) was mounted in front of the f/2.8 camera lens. The camera was tilted slightly downward to optimize the field of view of the camera with the present window geometry. The frame rate of the intensified CMOS camera was set according to the experimental conditions (2500, 5000, 10,000 fps) with an intensifier gate time (effective exposure time) of 98 µs.

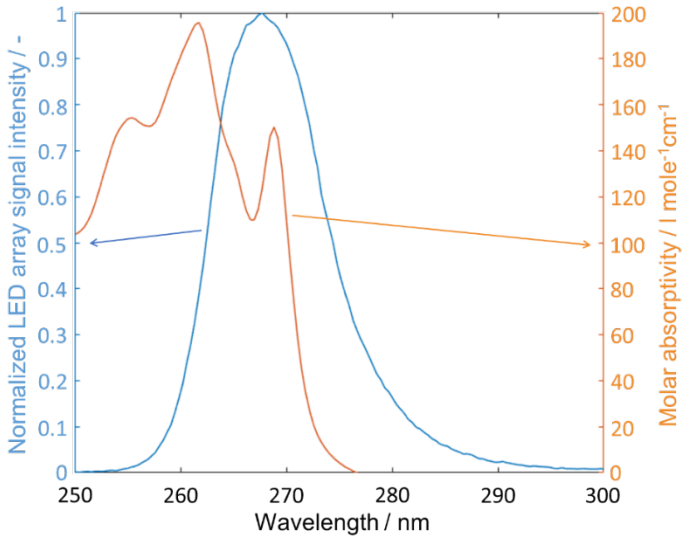

Figure 4.5. Spectra of the LED emission (left axis) and of toluene UV absorption (right axis).

An 810 nm LED ("CAVILUX HF for High-Speed Illumination", 500 W, 1 µs pulse duration) was used as a source of illumination in the DBI setup. The light was projected towards the constant-volume cell through an optical system consisting of a diffuser, a neutral density (nd) filter and an 810 nm bandpass filter. The transmitted light was collected by a high-speed CMOS camera (SA5 Photron) with a Nikon objective lens (f = 85 mm, f/1.8). The acquisition rate of the camera was set between 2500 and 5000 fps with an exposure time of 10.7 µs. The optical setup of the DBI diagnostics and light path (red) are shown in **Figure 4.5**. The UV absorption light path is shown in blue with the vertical axis of the cell.

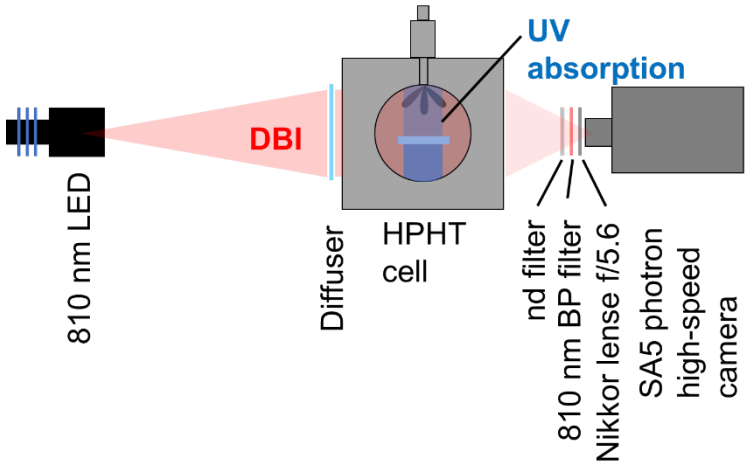

Figure 4.6. Schematic of the DBI technique through the horizontal axis of the constant-volume cell. The UV absorption optical path is orthogonal to the view plane and is represented by the blue color in the vertical axis of the cell.

4.1.4 Photometric image quantification

The absorption technique measures the absorbance "A" of the incident light by the absorbing tracer (toluene, in our application) after passing through the deposited fuel-film containing the absorbing tracer. This technique is based on Beer-Lambert's law [20,75]. Toluene, the absorbing tracer, absorbs UV light between about 230 and 280 nm wavelength, while its absorption above 300 nm is negligible. Iso-octane is transparent over the whole relevant wavelength range. The Beer-Lambert law relates the measurable absorbance A and the desired film thickness d via **Equation (4.3)** [20]:

$$A = -\log_{10}\left(\frac{I}{I_{ref}}\right) = -\log_{10}\left(\frac{I_t - I_{dark}}{I_{ref} - I_{dark}}\right) = d\ c\ \varepsilon \qquad (4.3)$$

where I_t is the image at time t, I_{ref} is a reference image, and I_{dark} is a dark image. d is the thickness of the film, c the concentration of the absorbing species, and ε

its molar absorptivity. In reality, ε and c might vary with the thermodynamic conditions and due to preferential evaporation, respectively [76]. In general, in a heated film consisting of a multi-component mixture, ε might vary with temperature and c due to preferential evaporation. The effects of temperature and preferential evaporation on ε and c will be shown in **sections 4.1.6** and **4.3**, respectively.

DBI is an extinction-based diagnostic widely used for soot measurement. This technique is also governed by Beer-Lambert's law. It measures the extinction (absorption and scattering) of incident light by soot particles after passing through a soot cloud, which is related to the soot volume fraction, as indicated in **2.4.1**. In this work, light extinction was calculated and converted into optical thickness *KL* via **Equation (4.4)**:

$$\frac{W_t - W_t^{dark}}{W_{ref} - W_{dark}} = -\exp(KL) \tag{4.4}$$

In **Equation (4.4)**, W_t is the image at time *t*, W_{ref} is a reference image, and W_t^{dark} is a dark image acquired just before W_t at time *t*, and W_{ref} is a reference image.

4.1.5 Synchronization

Figure 4.6 shows the synchronization scheme for one injection repetition. The UV absorption and DBI image acquisitions were triggered simultaneously. In each case, two images were acquired before start of injection (bSOI): a dark frame image and a reference image, denoted by I_{dark} and I_{ref}, respectively. Injection and ignition were triggered simultaneously. After start of injection (aSOI), UV absorption images with UV light ON were acquired, and denoted by I_t as indicated in **Equation (4.3)**. For DBI, images were collected by alternating dark images and images with light ON. These images were denoted by W_t^{dark} and W_t, respectively, in **Equation (4.4)**, respectively. The dark images were used to correct for the soot incandescence in the extinction images. The acquisition rate was dependent on the evaporation rate corresponding to each experimental condition and varied between 500 and 10,000 fps.

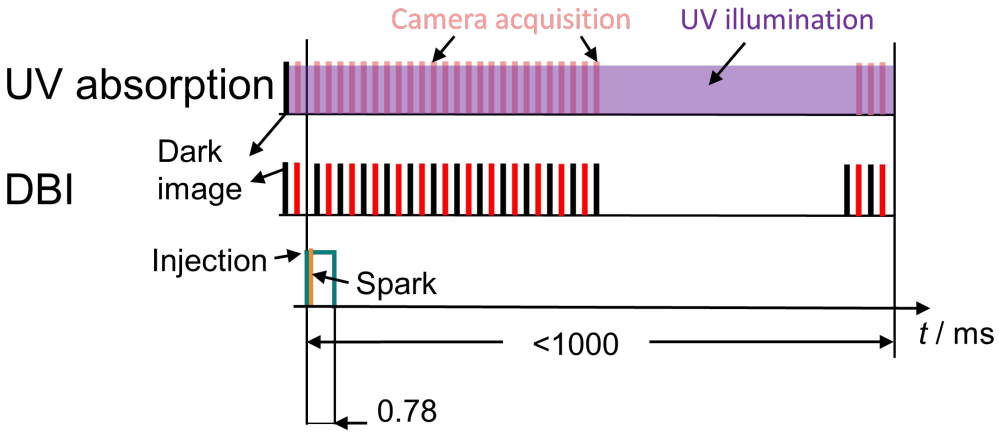

Figure 4.7. Synchronization scheme of the UV absorption and the DBI, injection, and spark.

4.1.6 Effect of temperature

As shown in **Equation (4.3)**, the absorbance depends on tracer concentration, the thickness of the liquid-fuel and the molar extinction coefficient. The molar extinction coefficient might be affected by temperature and pressure. Here, the effect of pressure on the molar extinction coefficient was not investigated and is assumed to be negligible. The effect of temperature will be shown in this section.

Samples of 70% iso-octane – 30% toluene fuel surrogate were placed in a UV-visible spectrophotometer (Varian Cary 400 Scan). The temperature was varied from 298 to 338 K. The molar extinction coefficient was calculated at different temperatures. The traces, shown in **Figure 4.7**, show a slight dependence of the molar extinction coefficient on temperature. The molar extinction coefficient increased by 7% maximum when increasing the temperature from 298 to 338 K. Since the molar extinction coefficient is slightly dependent on temperature, we did not take into account the error related to temperature on the absorbance images.

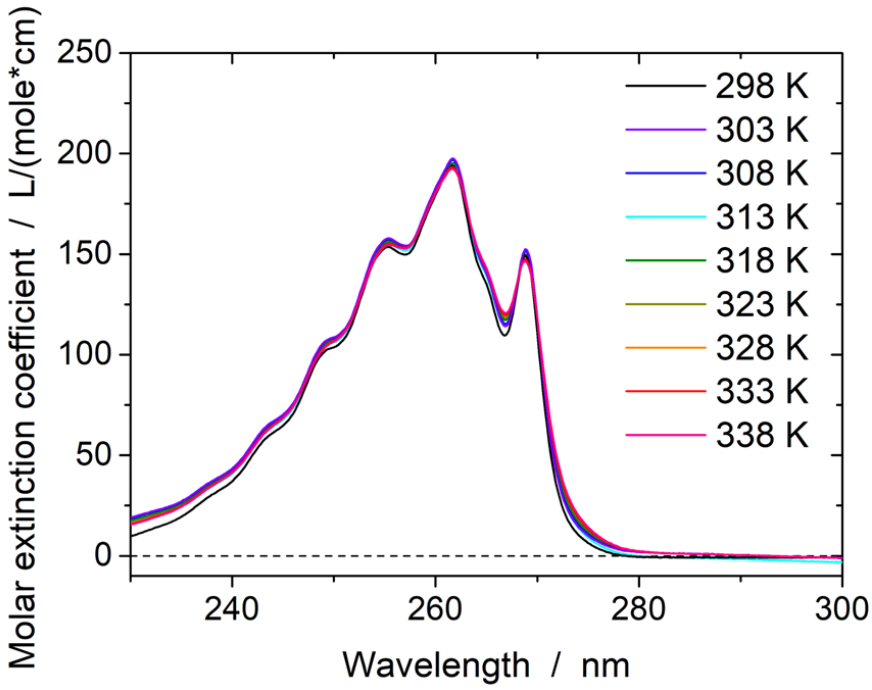

Figure 4.8. Molar extinction coefficient of toluene (70% iso-octane - 30% toluene fuel surrogate) with respect to wavelength at different fuel temperatures.

4.1.7 Interference by soot, vapor, and scattering

In this section, the interference by soot, vapor, and scattering in the absorption images is shown qualitatively. Preliminary experiments with iso-octane injection indicated the importance of using diffused light rather than collimated light in the absorption technique. In these tests, iso-octane was injected onto a quartz plate installed in a constant flow facility, shown in **section 4.2.1**, at ambient conditions from a six-hole Bosch injector at an injection pressure of 100 bar for an injection duration of 1 ms. A 670 nm LED was used as the illumination source. At 670 nm, iso-octane is transparent and does not absorb light. Therefore, the contribution of light scattering without and with a diffuser can be evaluated. **Figure 4.8** shows raw images of the iso-octane fuel-film illuminated by (a) collimated light and (b) by diffused light. Without a diffuser, the image shows a well-defined structure of the fuel-film related to the light-scattering at the fuel-film interface, but this sharp structure becomes less significant with a diffuser. The use of a diffuser reduced the effect of light scattering in the fuel-film images. The interference by light scattering in the fuel-film thickness images will be analysed more quantitatively in **chapter 5**.

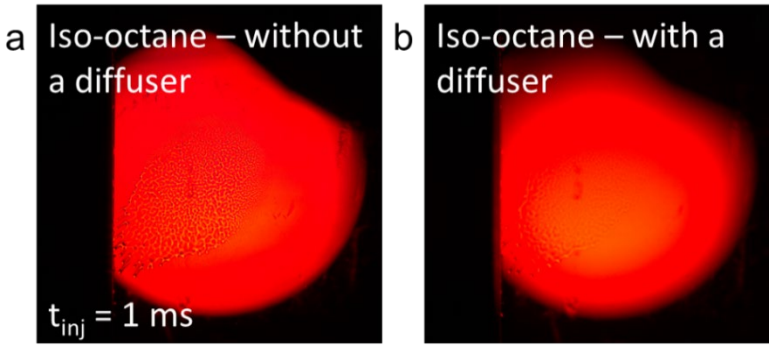

Figure 4.9. Raw absorbance images of iso-octane fuel-films illuminated by collimated light (a) and by diffused light (b) showing that diffused light reduces the effect of light scattering interference in absorbance images.

Figure 4.9 shows raw UV-absorption images after direct injection of 70% iso-octane – 30% toluene into the constant volume cell. **Figure 4.9**a shows deposited liquid fuel-films with vapor contribution interfering with the liquid absorption. The vapor was generated early aSOI from the evaporating fuel spray along the injector axis and the evaporating liquid fuel-film. **Figure 4.9**b shows a significant contribution from soot after combustion, making the field of view optically dense. Distinguishing between the absorption of the liquid fuel-film, soot and vapor becomes difficult during combustion.

Figure 4.8 and **Figure 4.9** show that with the single wavelength UV-absorption technique (at 265 nm), contributions from light-scattering, vapor, and extinction by soot and soot precursors make quantification of liquid-fuel film thickness more difficult. To distinguish between liquid fuel-film and vapor fuel contributions, an algorithm was developed to approximate fuel-vapor absorption above the liquid fuel-film regions. It will be presented in **section 5.1.2**. It is based on the observation that the changes in the vapor cloud and the liquid fuel-films present clear distinct spatio-temporal features in their appearance in the image sequences. At UDE, a time-multiplexed multi-spectral UV-visible absorption technique was developed on the basis of the single wavelength UV-absorption technique to take into account the contributions from light scattering and the extinction by soot and soot precursors for the quantification of fuel-film thickness. It is based on the quasi-simultaneous use of different wavelengths, taking advantage of the wavelength dependence of these phenomena. This technique will be presented in **section 4.2**.

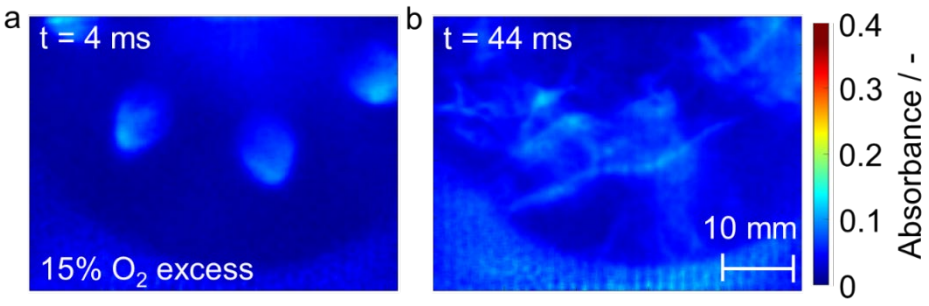

Figure 4.10. Absorbance images during fuel-film (a) evaporation and (b) combustion of 70% iso-octane - 30% toluene at p = 1 bar and T = 100°C.

4.2 Constant-flow facility experiments

In this section, a time-multiplexed multi-spectral UV-visible absorption technique will be presented. This technique was developed at UDE and was based on the UV absorption technique presented in **section 4.1**. In the single wavelength UV absorption technique, it was not possible to distinguish the absorption of the liquid fuel-film from the contributions of light scattering, vapor and extinction by soot and soot precursors. Here, additional wavelengths (other than 265 nm) were used to differentiate scattering and absorption in the liquid-fuel film as well as light extinction by soot and soot precursors [72].

4.2.1 Facility and experimental conditions

The experiments were carried out in the optically accessible constant-flow facility shown in **Figure 4.10** [33,48,49,77].

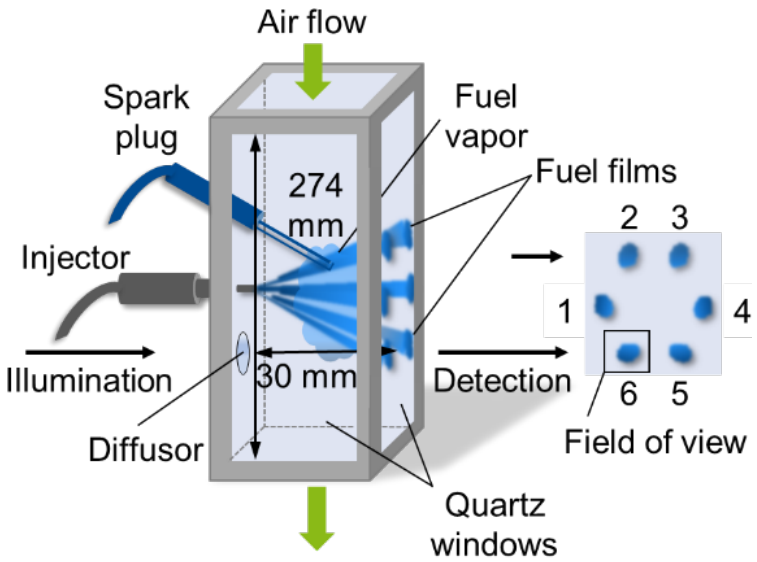

Figure 4.11. Optically accessible atmospheric-pressure constant-flow facility with injector and spark electrodes.

Heated air entered at a flow velocity of 1.8 m/s and a temperature of T_{air} = 376 K, heating the walls to an inner temperature of T_{wall} = 352 K. Before spray impingement, heat is transferred conductively in steady state through the wall resulting in a linear temperature profile. The inner wall temperature is 352 K and the outer wall temperature is 344 K. The wall temperatures were measured with a sheathed thermocouple (Type K, NiCr-Ni) temporarily attached to the wall with thin heat resistant tape [49]. Two fuel surrogates were used. The first fuel surrogate, denoted by FS1, is the reference fuel surrogate used in the constant-volume cell experiments. FS1 was a mixture of 30% toluene and 70% iso-octane. The second fuel surrogate, denoted by FS2, consisted of 30% toluene, 60% iso-octane and 10% n-octane (boiling points 383, 372, and 398 K, respectively). 9.3 mg of fuel were injected at $p_{inj.}$ = 100 bar from a six-hole injector. The injection duration was 1 ms. A custom-built spark plug ignited the evaporated fuel 0.7 ms after the end of injection. The distance between the tip of the injector and the impact plate was 30 mm. As described in detail in the next section, one of the films was back-illuminated via a diffuser mounted in the wall holding the injector and igniter, and the transmitted light was detected by a camera.

4.2.2 Multi-spectral absorption imaging

Fuel-film thicknesses were measured from toluene's absorbance near 265 nm, but at this wavelength, there is not only absorption by liquid toluene, but also other sources that are listed here along with the strategy to take it into account:

(1) Absorption by toluene vapor is spectrally indistinguishable from that by liquid toluene. However, because of its different diffusive-convective properties, the vapor appears visually different from the liquid film in image sequences. Based on that, in the experiments performed at IFPEN we developed a morphological post-processing to differentiate between these two signal contributions [71]. The algorithm is presented in **section 5.1.2**.

(2) Scattering (comprising refraction and reflection) at the film surface re-distributes the signal on the sensor, causing locally positive or negative bias in the absorbance measurement. This can be corrected if the transmittance is additionally measured at a wavelength where toluene does not absorb. Measurements at 310 nm were chosen here.

(3) Soot and soot precursors, forming near the evaporating fuel films, also absorb and scatter the UV light. As for scattering, this can be corrected by measurements at an additional wavelength, but as opposed to interface scattering, extinction is expected to be strongly wavelength dependent. Thus, we acquired information on that dependence with additional measurements at 365 and 520 nm.

(4) Soot incandescence (thermal radiation of hot soot particles) adds to transmitted illumination, decreasing the measured "absorbance". This broadband, continuous source of interference can be partially suppressed with spectral filtering and short sensor exposure times. The remainder is quantified from measurements without illumination.

4.2.3 Optics and image acquisition

Figure 4.11. shows a top view of the optical layout while important spectral features are shown in **Figure 4.12**. A cage-mounted system of collector lenses and beam splitters (BS310, BS325, BS376, all from Semrock) collimated and combined the light from LEDs at 265 (OSA, 2.2 mW continuous output power), 310 (OSA, 1.9 mW), 365 (Nichia, 750 mW), and 520 nm (Nichia, 1000 mW). The illumination was diffused by a sandblasted fused-silica window (40 mm diameter) before passing through the test section of the flow facility and the fuel film.

The transmitted light was collected with a high-speed intensified CMOS camera (LaVision High-Speed IRO + Photron SA-Z) via a UV camera lens (f = 100 mm, f/2.8). The intensifier gain was set to 47 (in LaVision's DaVis software) for the reacting case and to 50 for the non-reacting case. The spectral response of the S-20 photocathode of the intensifier is between 10 and 25% in the relevant spectral range. A Schott UG5 filter in front of the objective suppressed some of the soot incandescence, represented in **Figure 4.12** by blackbody emission at a typical flame temperature T = 1800 K. This filter also blocks most of the light from the 520-nm LED, but that LED was driven with the longest pulse duration and has much more power than the deep-UV ones.

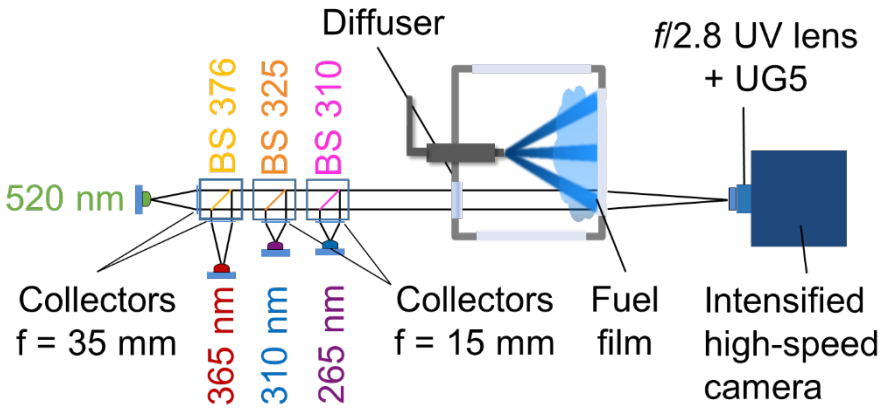

Figure 4.12. Optical layout around test section of flow facility.

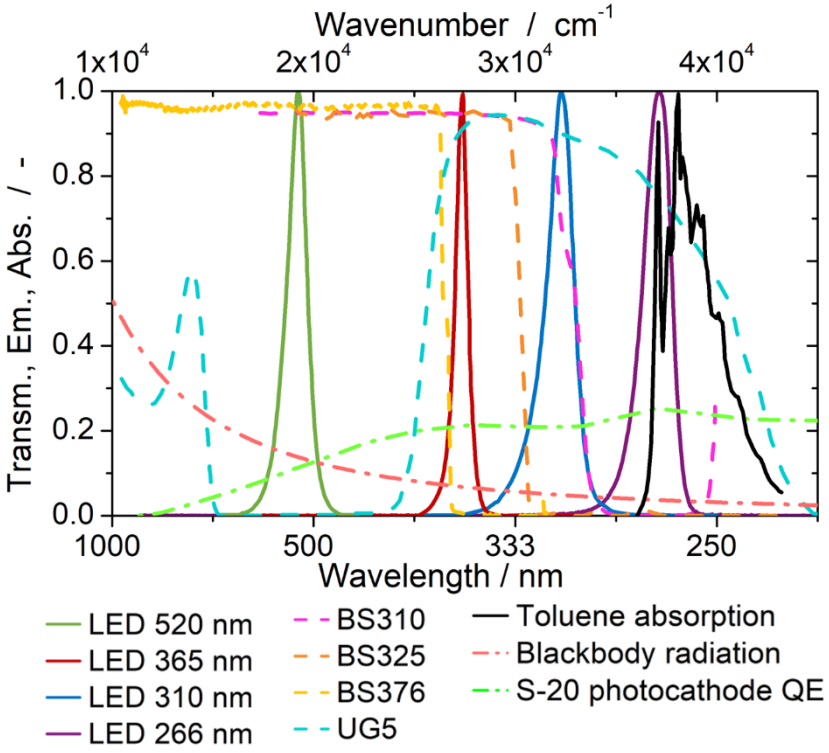

Figure 4.13. Main spectral features of the experiment: Transmittance of the optics, emission spectra of the LEDs, absorption spectrum of toluene [75], blackbody radiation spectrum at 1800 K, quantum efficiency (QE) of the intensifier's photocathode.

Figure 4.13a shows the temporal acquisition strategy for one imaging cycle, a sequence of 5 images. The high-speed camera was operated at 32 thousand frames per second (kfps). The intensifier gate was set to 3.5 µs, thus entirely capturing each LED's emission while keeping the interference from soot incandescence at a minimum. The four LEDs were pulsed and imaged consecutively at 6.4 kHz, plus one "dark" frame without any LED on (32/5 kHz). The pulse durations, indicated in **Figure 4.13**a, were chosen to use the full dynamic range of the camera and to yield similar signal intensities for all LED "colors" in the raw images.

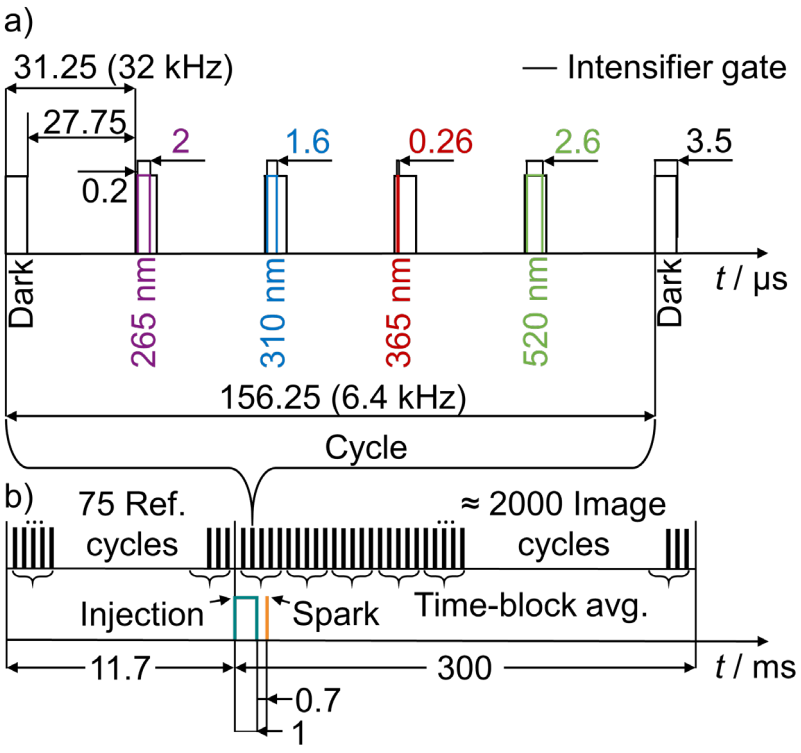

Figure 4.14. (a) Acquisition time diagram for one imaging cycle, (b) synchronization scheme of reference and imaging cycles, injection, and spark.

Figure 4.13b shows the synchronization scheme for one injection repetition. 75 (5-image) cycles were acquired before start of injection (bSOI), followed by about 2000 cycles after start of injection (aSOI), i.e., with the fuel film on the wall. The 75 reference images at each wavelength were averaged to yield bright-field reference images $\langle I_{0,\lambda} \rangle$. An average dark image $\langle I_{\mathrm{dark}} \rangle$, calculated from the average of the dark images bSOI acquired just before the LEDs were pulsed, was subtracted from the reference images at each wavelength.

4.2.4 Image processing

For each LED wavelength and for the dark images, the raw images were first 2×2-binned (increasing the projected pixel size from 0.024 to 0.048 mm/pixel), and then time averaged in blocks of five imaging cycles, the resulting block average denoted $\langle I_\lambda^t \rangle_5$. The data was averaged primarily to increase the signal-to-noise ratio in the 265 nm absorbance images. At the mean air flow of 1.8 m/s, the convective movement over one 5-image acquisition cycle is 5.9 binned pixels, or 0.28 mm. The block-average of 5 cycles then corresponds to 1.4 mm movement blur. In these experiments, the nominal cycle time t is that at the temporal center of each five-cycle block.

Figure 4.14 shows raw images at all four LED wavelengths and the corresponding dark images. The images in the top rows are from shortly after injection while the ones in the bottom rows show the film in combustion with soot nearby. Images at 265 nm show the deposited absorbing fuel film. Before soot formation, images at 310, 365 and 520 nm show the scattering on the fuel film. After soot formation, the effect of scattering on the film becomes negligible compared to the light extinction by soot precursors and soot. The dark image in the second row shows significant soot incandescence.

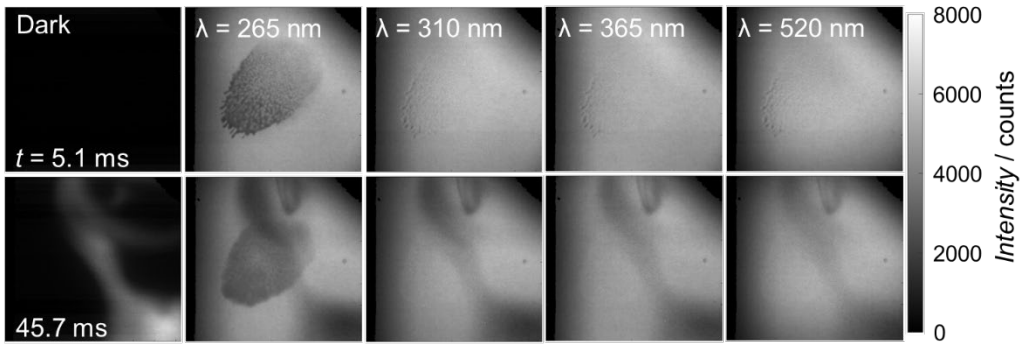

Figure 4.15. Example raw image sequences from two nominal cycle times before (5.1 ms aSOI) and after (45.7 ms aSOI) the onset of soot signal. First column: raw dark images. Four columns to the right: Dark-subtracted raw images at 265, 310, 365, and 520 nm. All images are block-averaged and 2x2 binned.

The averaged dark image $\langle I^t_{dark}\rangle_5$ at time t, showing soot incandescence, was subtracted from $\langle I^t_\lambda\rangle_5$.

In the absorbance equation (**Equation (4.1)**), I_{ref} and I are then represented by $(\langle I_{0,\lambda}\rangle - \langle I_{\mathrm{dark}}\rangle)$ and $(\langle I^t_\lambda\rangle_5 - \langle I^t_{\mathrm{dark}}\rangle_5)$, respectively. Thus, the absorbance image A at time t and wavelength λ is:

$$A = -\log_{10}\left(\frac{\langle I^t_\lambda\rangle_5 - \langle I^t_{dark}\rangle_5}{\langle I_{0,\lambda}\rangle - \langle I_{dark}\rangle}\right) \qquad (4.5)$$

However, as it will be presented in **section 8.1.1**, the intensity of the raw images varied with respect to time. This phenomenon, which was caused by the detection system, was found at all wavelengths and all experimental conditions. The absorbance images at time t and wavelength λ are calculated from the ratio of the raw images to the reference image. Any variation in the intensity of the raw images over time will result in an error in the absorbance images.

After calculating the correction coefficient k^t_λ, the intensity variation in the raw absorbance images was corrected. The absorbance in **Equation (4.5)** was

corrected by k_λ^t. The intensity corrected absorbance A (calculated in the UDE experiments) at time t and wavelength λ was then calculated via **Equation (4.6)**:

$$A = -log_{10}\left(\frac{\langle I_\lambda^t\rangle_5 - \langle I_{dark}^t\rangle_5}{\langle I_{0,\lambda}\rangle - \langle I_{dark}\rangle} \times \frac{1}{k_\lambda^t}\right) \tag{4.6}$$

Figure 4.15 shows the corrected intensity absorbance images, calculated from raw images shown in **Figure 4.14**.

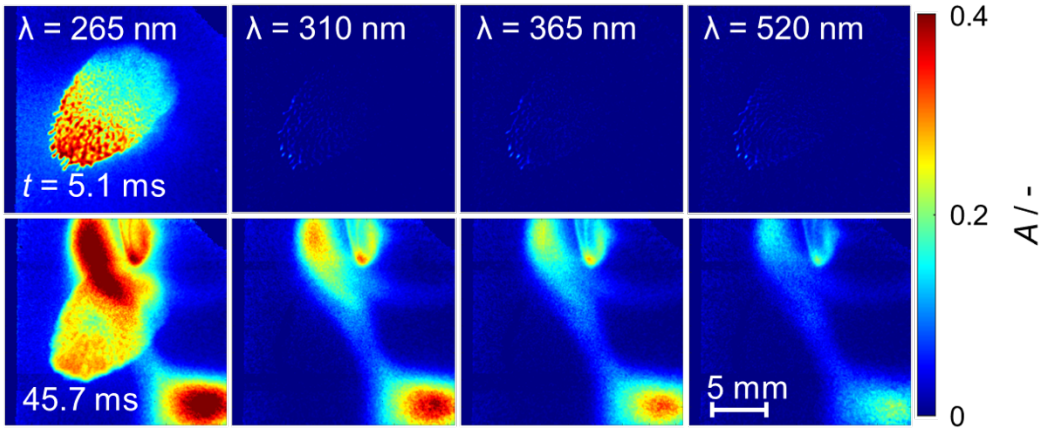

Figure 4.16. Example absorbance image sequences from two nominal cycle times before (5.1 ms aSOI) and after (45.7 ms aSOI) the onset of soot signal (calculated from raw images shown in Figure 4.14. Columns (from left to the right): Dark-subtracted absorbance images at 265, 310, 365, and 520 nm. All images are block-averaged and 2x2 binned.

4.3 Fuel surrogates and preferential evaporation

After injection and formation of the liquid fuel-film, the tracer (e.g., toluene) is assumed to co-evaporate with the other components of the fuel surrogate, keeping its concentration constant. In reality, the fuel surrogate components evaporate preferentially according to their evaporation characteristics. Therefore, the tracer concentration may change during evaporation. At constant fuel film thickness and molar extinction coefficient, any change in tracer concentration will contribute to a difference in absorbance, resulting in uncertainty in the measurement of the liquid fuel-film thickness. In the following, we present a simulation and experimental study of a quasi-steady evaporation of a fuel mixture. The objective of the following study was to determine the uncertainty error associated with preferential evaporation on absorbance. Another objective was to find a fuel mixture composition that would reduce the variation of toluene concentration during the evaporation, and therefore the preferential evaporation effect on the liquid fuel-film thickness measurements.

4.3.1 Simulations of a quasi-steady evaporation of a fuel mixture

A numerical model has been developed at IFPEN [76] for the evaporation of a multicomponent mixture at equilibrium state. This model is based on the Predictive SRK (PSRK) model which couples the cubic SRK equation with the UNIFAC activity model via excess Gibbs free energy mixing laws, which allows to take into account possible non-idealities between the components. The model is a succession of equilibria at imposed temperature and evaporated fraction. Each time step is simulated by completely eliminating the vapor phase until the initial fuel mixture is evaporated. The model determines the evolution of the volume fraction of components in the fuel mixture with respect to the evaporated percentage.

This model was used to study the quasi-steady evaporation of two fuel surrogate compositions. The reference fuel surrogate FS1 was composed of 70% iso-octane and 30% toluene (boiling points of 372 and 383 K, respectively). Iso-octane with its lower boiling point is expected to evaporate first. Therefore, the concentration of toluene in the evaporating mixture is expected to increase, resulting in an increase in absorbance. Adding a less volatile hydrocarbon to the iso-octane / toluene mixture is expected to reduce the variation in toluene concentration during the evaporation process. Therefore, with the volume fraction of toluene fixed at 30%, 10% of a less volatile hydrocarbon, n-octane (boiling point 398 K), was added. The second fuel surrogate FS2, was then composed of 60% iso-octane, 30% toluene and 10% n-octane.

4.3.2 Experiments and comparison to numerical results

After the study of the evaporation of the two fuel surrogates FS1 and FS2 numerically, the slow evaporation of both fuel surrogates on a heated plate was also studied experimentally.

Figure 4.16 shows the four steps of the experimental protocol for evaporation and absorbance measurements of the liquid fuel surrogates. The first step is to prepare the fuel mixture. 300 ml of the fuel mixture is then poured into a continuously stirred glass beaker, placed on a plate heated to T = 353 K inside a fume hood. This plate temperature is representative of a typical wall temperature in the constant-volume cell or in the constant-flow facility. Fuel vapor was continuously exhausted by a fan located about 1 m above the glass beaker. Samples were extracted with a pipette before and during evaporation from the remaining fuel mixture at different evaporated volume fractions, 0, 25, 50, 75, and 90%. The samples were then diluted by a factor of 1000 in UV-transparent iso-octane. The final step is the absorption measurement. The diluted evaporated

fuel mixture was poured into a 10 mm cuvette, which was then placed in a UV-visible spectrophotometer (Varian Cary 400 Scan).

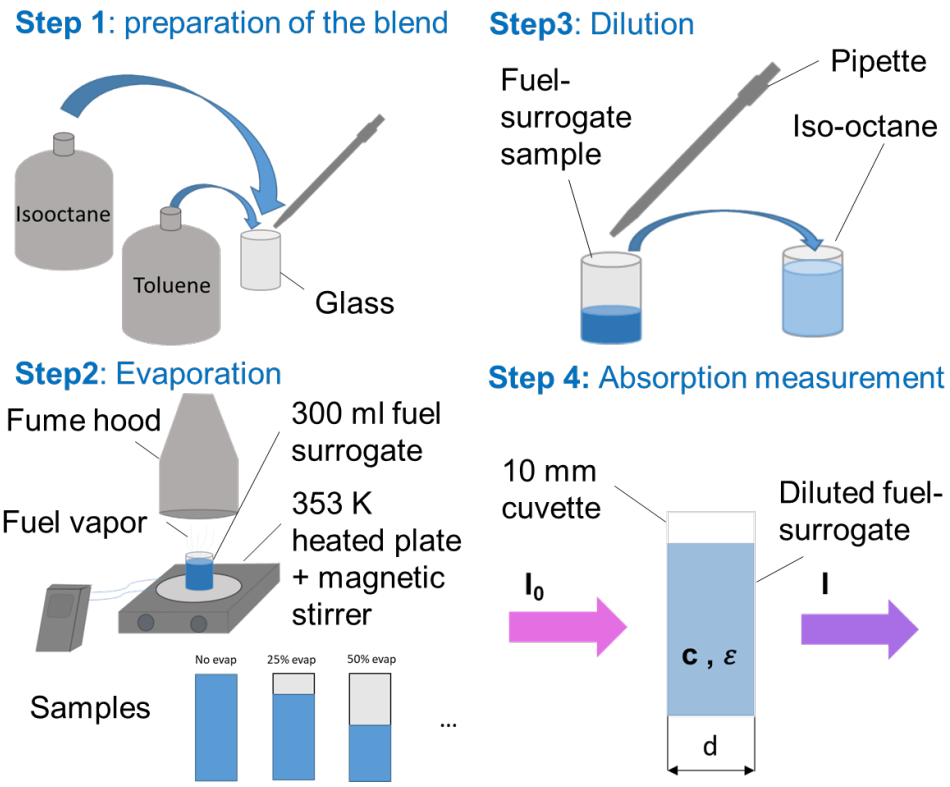

Figure 4.17. Steps of the experimental protocol of liquid fuel evaporation and absorbance measurement. A pipette was used to prepare the fuel surrogate and extract the evaporated fuel samples.

The absorbance spectra were calculated based on Beer-Lambert's law, see **Equation (4.3)**. The optical path d and the molar extinction coefficient ε are constant for all samples. The change in absorbance is directly proportional to the concentration of toluene. **Figure 4.17** shows the absorbance traces of (a) 70% iso-octane - 30% toluene (FS1) and (b) 60% iso-octane - 30% toluene - 10% n-octane (FS2) as a function of wavelength. In both cases, the absorbance increased as the evaporated percentage increased from 0% to 90%, indicating an increase in the concentration of toluene in the evaporating mixture due to preferential evaporation. This increase was reduced after the addition of n-octane (as shown in **Figure 4.17**b). The n-octane compensated for the high volatility of iso-octane and the large increase in toluene concentration in the mixture during evaporation, seen with FS1.

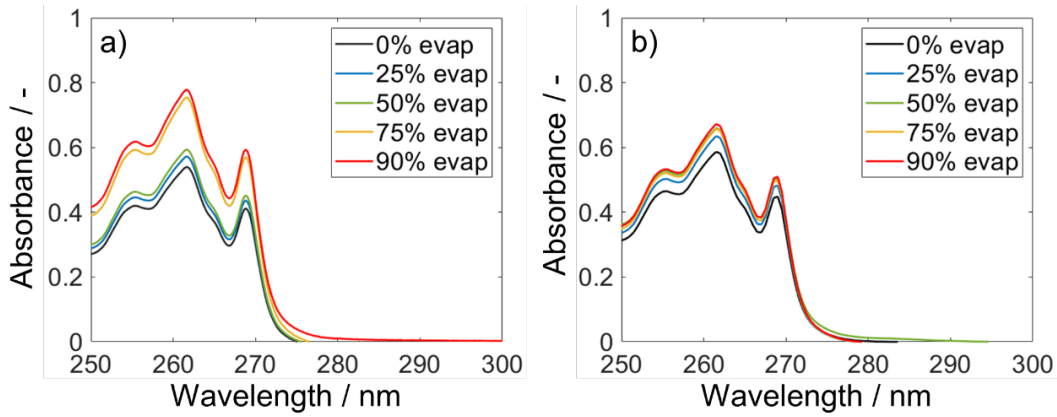

Figure 4.18. Absorbance of (a) 70% iso-octane - 30% toluene (FS1) and (b) 60% iso-octane - 30% toluene - 10% n-octane (FS2) versus wavelength.

To be representative of the 2D absorption measurements performed with a 265nm CWL LED, the absorbance was integrated between 260 and 270 nm, the spectral range where toluene has maximum absorbance. **Figure 4.18** shows the variation of the integrated absorbance at different evaporated percentages 0, 25, 50, 75 and 90%, normalized by the integrated absorbance calculated at 0% evaporated percentage for FS1 and FS2. At 90% evaporation, the toluene concentration in FS1 is about 30% higher than in FS2. Between 0 and 90%, an increase in toluene concentration of about 40% was found in FS1 while it was only about 10% in FS2. The addition of n-octane, which has a higher (but close) boiling temperature than both toluene and isooctane, reduced the effect of the preferential evaporation observed in FS1.

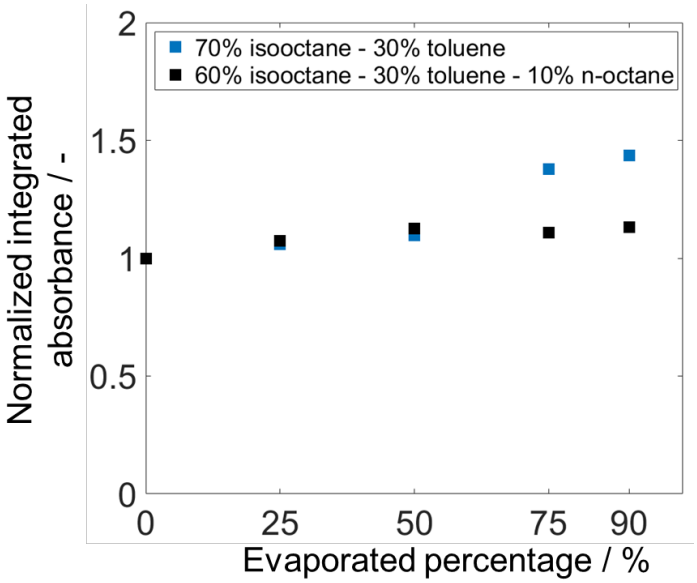

Figure 4.19. Evolution of the normalized integrated absorbance of FS1 and FS2 fuel surrogate mixtures versus the evaporated percentage.

The numerical (**section 4.3.1)** and the experimental toluene volume fractions obtained with FS1 and FS2 at different evaporated percentages are shown in **Figure 4.19**. The numerical results are consistent with the experimental results. These results show a significant effect of preferential evaporation on the variation of toluene concentration. In FS1, iso-octane evaporates faster than toluene ($T_{boiling\ iso\text{-}octane}$ = 372 K < $T_{boiling\ toluene}$ = 383 K). In this mixture, the volume fraction of toluene increased throughout the evaporation process. To reduce this large increase in toluene concentration, 10% of n-octane ($T_{boiling\ n\text{-}octane}$ = 398 K) was added to FS2. Comparing the numerically calculated toluene absorbance of the two fuel surrogates during evaporation, it increased by only 10% with FS2 versus 75% with FS1 when the evaporation reached 98%. Beyond this, the toluene concentration continues to increase in FS1 while it decreased to zero in FS2. Based on this result, the use of FS2 is expected to reduce the uncertainty of preferential evaporation by 65% at 98% of evaporated fuel mixture. The addition of the 10% n-octane to FS2 reduced the variation of the toluene volume fraction over much of the evaporation process.

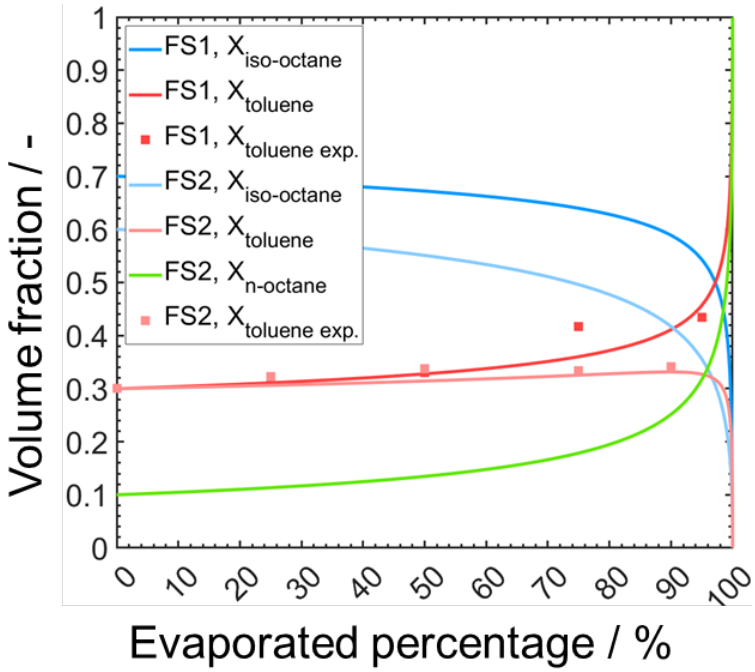

Figure 4.20. Evolution of the numerical and experimental volume fractions of FS1 and FS2 components with respect to the evaporated fuel mixture percentage.

4.4 In-situ calibration

As shown in **Equation (4.3)**, the absorbance A is directly proportional to the fuel-film thickness d, the tracer concentration c, and the molar extinction coefficient ε. Assuming that c and ε are constant, A and d are directly

proportional. On this basis, the absorbance of the liquid fuel-film can be converted to fuel-film thickness by calibration measurements relating A to d.

An in-situ calibration was performed by placing a cuvette with 10 mm thickness inside path length d in the constant-volume cell at 50°C. The fuel, consisting of 30% toluene in 70% iso-octane, was diluted 1:1000 in a non-absorbing solvent (UV transparent iso-octane). This corresponds to 10 µm of pure fuel thickness. Absorbance images were calculated via **Equation (4.3)**. **Figure 4.20** shows an absorbance image of 10 µm equivalent fuel-film thickness. The absorbance within the dashed white rectangle was averaged. The measured mean in-situ absorbance was A = 0.27 with a standard deviation of ±0.002 among three repetitions.

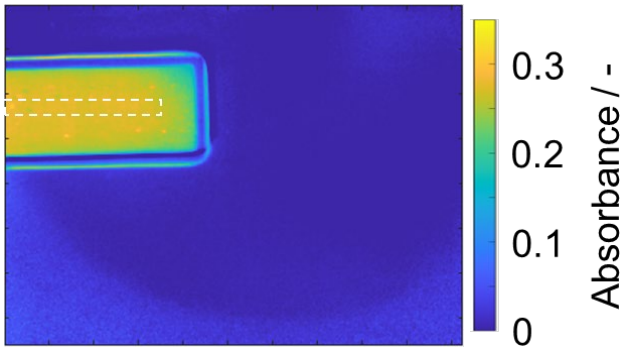

Figure 4.21. Absorbance of 30% toluene - 70% iso-octane fuel surrogate, diluted by 1:1000, in a 10 mm cuvette placed inside the high-pressure cell.

An in-situ calibration was also performed inside the constant-flow facility at ambient conditions. The in-situ calibration was performed for the two fuel surrogates FS1 (70% iso-octane – 30% toluene) and FS2 (60% iso-octane – 30% toluene – 10% n-octane). In both experiments and for both fuel surrogates, the absorbance at this thickness was equal to 0.27. From this, the proportionality constant 1 / (c ε) between d and A in **Equation (4.3)** was calculated to be 37 µm. The fuel film thickness is then calculated from the absorbance via $d = 37\ \mu m\ A$ in both the constant-volume cell and the constant-flow facility experiments.

5 Results

In this chapter, the results of the constant-volume cell and the constant-flow facility experiments will be presented. Quantitative results of liquid fuel-film thickness, mass and surface will be presented. The fuel film detection strategy, absorbance image correction post-processing and quantification of the liquid fuel-film will be presented. The extinction by soot and soot precursors will also be studied. Parts of this chapter were published by Shway et al. [71,72], in particular most of the results presented in **sections 5.1.1**, **5.1.2**, **5.1.3** were published in [71], and the results presented in **sections 5.2.1**, **5.2.2**, and **5.2.3** were published in [72].

5.1 Constant-volume cell experiments

5.1.1 Liquid fuel-film formation, evaporation and combustion

The experimental conditions in the constant-volume cell experiments were presented in **sections 4.1.1**, **4.1.2** and **4.1.3**. Under non-reacting conditions, the experiments were performed at initial cell temperatures $T = 50$, 100, 150 and 200°C and initial cell pressures $p = 0.5$, 1 and 6 bar. In total, twelve experimental conditions were used under non-reacting conditions. The initial cell temperature $T = 100$°C and cell pressure $p = 1$ bar were used under reacting conditions with two different residual oxygen excess percentages (2% and 15%). The role of residual oxygen excess in the experiments was clarified in **section 4.1.2**. Under both non-reacting and reacting conditions, ten repetitions were acquired for each experimental condition. The absorbance images were then averaged over the ten repetitions.

Figure 5.1 shows an example of fuel-film formation and evaporation under non-reacting conditions at $T = 100$°C and $p = 1$ bar**.** The example corresponds to a single repetition. In this figure, a series of eight non-corrected UV-absorption derived fuel-film thickness images is shown from 0.5 ms to 40 ms after (hydraulic) start of injection (aSOI). The image at 0.5 ms shows the fuel spray impinging on the quartz plate during injection. At 1 ms, the injection has stopped, and at 1.5 ms, the fuel film is completely deposited on the plate. Between 1 and 2 ms, the momentum of the spray causes movement of the fuel film on the plate. The airflow, created above the plate, induces shear forces pushing the liquid fuel film outward. After 4 ms, a vapor cloud, created from the evaporated fuel spray along the injector axis, is brought by the spray momentum from the top center of the image down over the deposited fuel films before it disappears after 10 ms. Between 4 and 10 ms this vapor is present in all images, and it causes an increase in the absorbance. The liquid-fuel film formation

features were similar under all experimental conditions. Some differences, which will be shown in the following sections, are related to the amounts of evaporated fuel, the masses of deposited liquid fuel, and the evaporation rate.

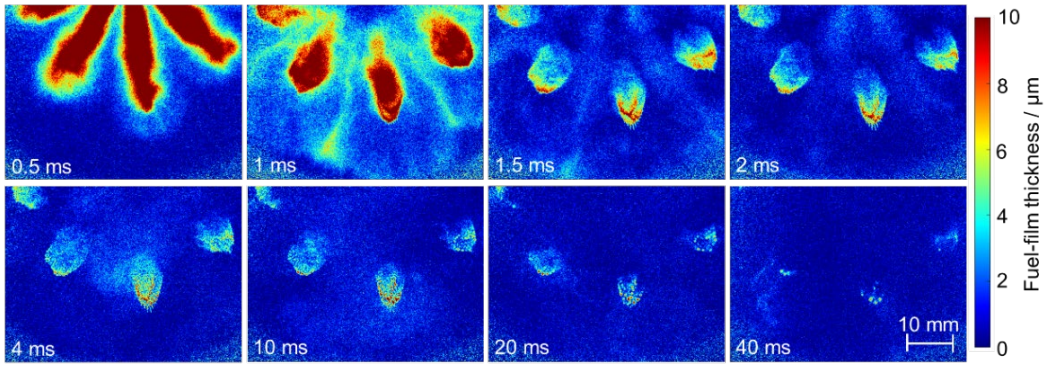

Figure 5.1. Time sequence of the UV-absorption derived fuel film thickness under non-reacting conditions at p = 1 bar and T = 100°C before masking out regions with significant vapor contribution in post-processing. Time are given with respect to hydraulic start of injection (aSOI).

Figure 5.2 shows images of the average liquid-fuel film thickness derived from UV-absorption images under non-reacting conditions at three selected times 4, 10 and 120 ms aSOI. Each set of twelve images at time t represents the twelve experimental conditions (T = 50, 100, 150, 200°C and p = 0.5, 1, 6 bar).

At 4 ms aSOI, not much liquid fuel-film thickness can be seen at 150°C and 200°C. Evaporation of the liquid fuel-film at the higher cell temperatures (150°C and 200°C) is fast compared to the lower cell temperatures (50°C and 100°C), and most of the liquid fuel-films evaporated before 10 ms aSOI. The evaporation of the fuel spray becomes more significant and less liquid fuel impinges on the quartz plate.

At 120 ms aSOI, only a small quantity of liquid fuel-films remains at p = 6 bar and T = 100°C. The evaporation time is longer at higher cell pressures. However, at 50°C, liquid fuel films are present on the plate at all three pressures, with larger quantities at 1 bar than at 0.5 and 6 bar.

At 4 ms, significant vapor clouds formed above the liquid fuel-film at 6 bar. This is due to increased evaporation of the fuel spray at high cell pressures. Compared to cell pressures of 1 and 0.5 bar where the fuel film is fully deposited on the plate at 4 ms aSOI, the fuel took longer time to completely deposit on the plate, and the evaporation of the fuel-film was slower. Small liquid fuel-film thicknesses are observed at 6 bar. Under sub-atmospheric pressure (0.5 bar), the

fuel film was deposited on the plate earlier and evaporated faster than at 1 and 6 bar.

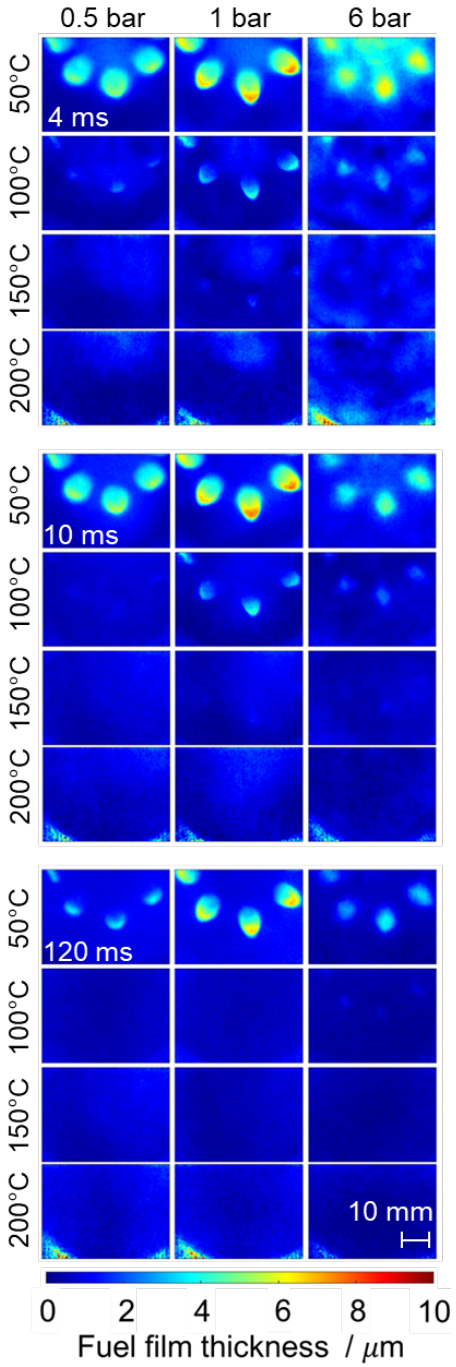

Figure 5.2. Time sequence of the UV-absorption derived fuel film thickness averaged among 10 repetitions under non-reacting conditions at 4, 10 and 120 ms aSOI. Each set of twelve images represents twelve experimental conditions at p = 0.5, 1, 6 bar (columns) and T = 50, 100, 150, 200°C (rows) before masking out regions with significant vapor contribution in post-processing. Times are given with respect to hydraulic start of injection.

The features of liquid fuel-film formation and evaporation were similar under the different experimental conditions. Vapor was observed early after injection in all experimental conditions. However, the mass of the deposited liquid fuel-film and the evaporation rate were different under different experimental conditions. The physics behind these results as well as the liquid fuel-film mass results will be presented in **section 5.1.4**.

Figure 5.3 shows a comparison of the UV-absorption derived fuel-film thickness averaged over 10 repetitions under non-reacting and reacting conditions (15% of residual O_2) at $p = 1$ bar and $T = 100$°C. The non-reacting and reacting cases show some similarities in the fuel-film thickness and morphology before soot formation (first row, at 4 ms aSOI). Under reacting conditions (second row at 44 ms), the extinction by soot and soot precursors interferes with the absorption of the liquid fuel-films still being detected on the plate under non-reacting conditions, and makes the quantification of the liquid fuel-film thickness difficult. In the constant-volume cell experiments, only the non-reacting cases and reacting cases before soot formation were evaluated quantitatively. The fuel vapor contribution was approximated by applying the morphological algorithm described next.

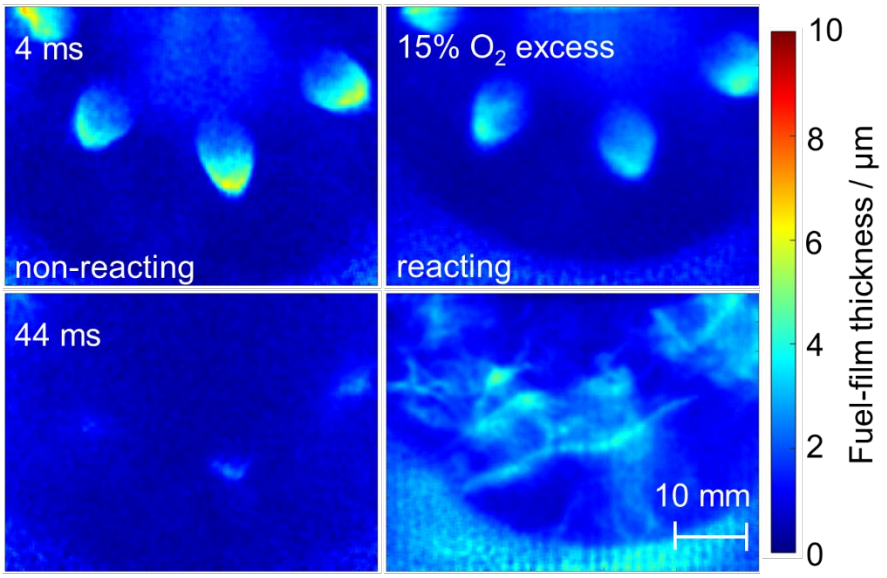

Figure 5.3. UV-absorption derived fuel-film thickness averaged over 10 repetitions at p = 1 bar and T = 100°C under non-reacting and reacting conditions at t = 4 ms and t = 44 ms aSOI without correction.

5.1.2 Morphological post-processing separating liquid and vapor

Vapor from the evaporating liquid fuel adds to the absorption by the liquid fuel films and is spectrally indistinguishable. To improve the accuracy of the liquid-

fuel film thickness measurement, a morphological post-processing algorithm, schematically shown in **Figure 5.4**, was developed and applied to images under non-reacting conditions. The algorithm segments the image into three levels: a background that represents the image noise, a mid-ground that represents the vapor, and a foreground that represents the liquid fuel-film. Based on that segmentation, the absorbance of vapor in liquid fuel-film regions was then approximated by interpolation, as indicated in **Figure 5.6**, and subtracted from the measured absorbance. The morphological processing proceeds through the calculation of three binary masks, as outlined below and in **Figure 5.4**.

To demonstrate the post-processing of liquid fuel-film detection, UV-absorption images containing the four fuel films at $T = 100°C$ and $p = 1$ bar are used. For preliminary work, the images were subsampled at a frame rate of 2 kHz to reduce computational time of first post-processing tests. If not mentioned otherwise, a dark image was calculated from the average of fifty dark images acquired before injection. The average dark image was subtracted from all images before any of the processing described here.

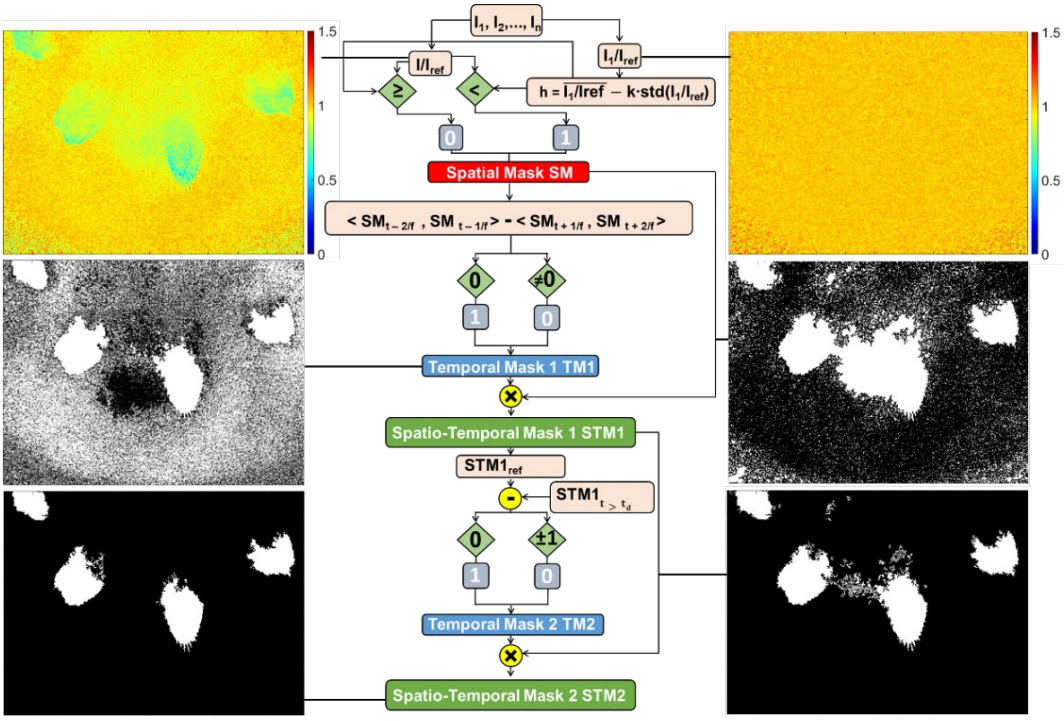

Figure 5.4. Flowchart of the morphological image processing for separating background, vapor, and liquid films. Images in the flowchart correspond to one repetition at $p = 1$ bar and $T = 100°C$.

Spatial mask: A reference image I_{ref} is calculated as the mean of several images acquired before injection. The shot noise was estimated from the ratio of I_1 to I_{ref},

where I_1 is a single image before injection. The spatial mean $\overline{I_1/I_{ref}}$, and the spatial standard deviation std(I_1/I_{ref}) were calculated. A threshold of $\overline{I_1/I_{ref}}$ - k·std(I_1/I_{ref}) represents the shot noise absorbance level (background) in the images and separates it from the absorbance levels of the fuel vapor and liquid film (mid-ground and foreground, respectively). k depends on the noise level related to the sensitivity of the optical setup (k = 2, in all IFPEN experiments). The result is a time series of binary masks SM.

First spatio-temporal mask: Starting from the approximate time t_d when the fuel film is completely deposited on the plate (1.5 ms aSOI, in the example of **Figure 5.4**), an inter-frame subtraction with a time base of 3/f is applied to the time series of spatial masks derived above (f is the acquisition frame rate). The physical idea behind this is that the liquid fuel film moves very little, but the vapor is transported significantly by convection in an interval of 3/f (1.5 ms, in this example). Therefore, in the result, all zero pixels are taken to correspond to the liquid fuel and are assigned the value 1, while non-zero pixels correspond to vapor and are set to 0. This "temporal mask" TM1 is multiplied with the "spatial mask" SM. We designate the result as "spatio-temporal mask" STM1 to reflect the nature of the operation that it resulted from, but in fact it is another sequence of binary spatial masks.

Second spatio-temporal mask: Each STM1 in the time sequence is subtracted from a "STM1 reference mask" ($STM1_{ref}$). This reference mask should be calculated from UV-absorption image acquired early aSOI corresponding to a reference time t_{ref} (t_{ref} = 2.5 ms aSOI, in the example of **Figure 5.4**) and having a well-defined sharp fuel-film structure. The calculation of the second spatio-temporal masks is based on the observation that the surface of the fuel film decreases during evaporation. In the resulting temporal mask TM2, again 0 corresponds to liquid and is set to 1, while non-zero indicates vapor and is set to 0. A second series STM2 of "spatio-temporal" mask representing the liquid fuel film (the foreground) is obtained by multiplication of the STM1 with TM2.

The ratio images I/I_{ref} are then multiplied by the corresponding mask STM2 and converted into absorbance, and then film thickness. A time sequence of the masked uncorrected fuel film thickness images is shown in **Figure 5.5**.

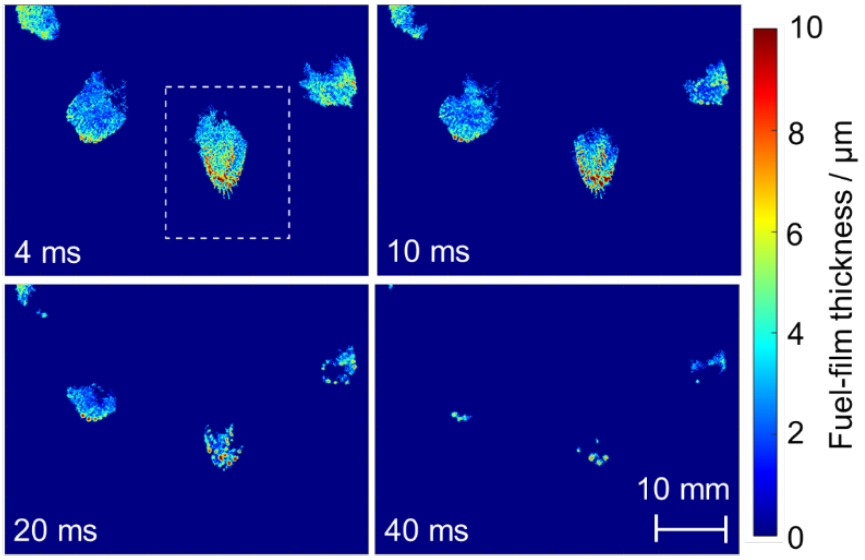

Figure 5.5. Time sequence of the UV-absorption derived fuel film thickness at p = 1 bar and T = 100°C (shown in Figure 5.1) after masking out regions with significant vapor contribution in post-processing. The white rectangle marks the region examined more closely in Figure 5.7 and Figure 5.8.

The morphological post-processing defines the regions of predominately liquid fuel films but does not account for the contribution of vapor absorbance in these regions. An algorithm to correct for that vapor-associated absorbance was developed and applied to the region within the dashed white lines in the first-row image on the left in **Figure 5.5** that contains one of the fuel films.

First, the spatio-temporal mask STM2 is dilated horizontally and vertically by 20 pixels. This dilated mask is then subtracted from the spatio-temporal mask STM2, yielding a 20-pixel thick edge mask around the liquid-film region. This edge mask is multiplied with the unmasked images of absorbance (**Figure 5.6**a) to yield an image of absorbance surrounding the liquid film, as shown in **Figure 5.6**b. The contribution of vapor absorbance inside of this edge is then approximated by bilinear interpolation between the mean absorbance values in the edge. **Figure 5.6**c shows the vapor-dominated region filled in with this interpolation, but in fact to obtain "vapor-corrected" images (**Figure 5.6**e), we simply subtract the interpolated image from the already masked images (**Figure 5.6**d) that were the output of the morphological processing described above.

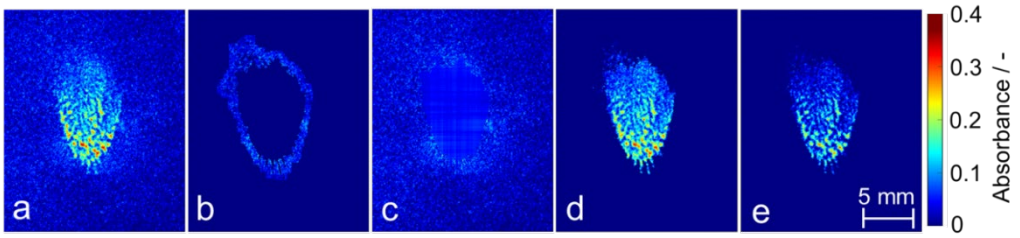

Figure 5.6. Approximation of the vapor contribution in the absorbance of the liquid fuel film (here at 7 ms aSOI). a) Absorbance as calculated via Equation(4.3), b) dilated edge of foreground mask, c) interpolation-based estimate of the vapor absorbance, d) foreground-masked absorbance, and e) vapor-corrected fuel-film absorbance. The absorbance scale indicated here corresponds to 0-15 µm equivalent liquid fuel-film thickness scale.

5.1.3 Liquid fuel-film thickness, mass and surface

Quantitative results of the subsampled corrected data at $T = 100°C$ and $p = 1$ bar are presented here**.** The top row of **Figure 5.7** shows selected images from a time sequence of the fuel film thickness after vapor correction. The fuel mass decreases by 68% between 4 and 20 ms aSOI. Only 7% of the initial fuel mass remains on the plate at 40 ms aSOI. The bottom row of **Figure 5.7** gives an impression of the reproducibility of the injection-induced fuel film, showing the film at a fixed time, 7 ms aSOI, for five other repetitions. While the overall structure of the film is always the same, small-scale differences between different injections are visible. The fuel mass at this time varied between 0.069 and 0.089 mg in the 6 repetitions represented in **Figure 5.7**.

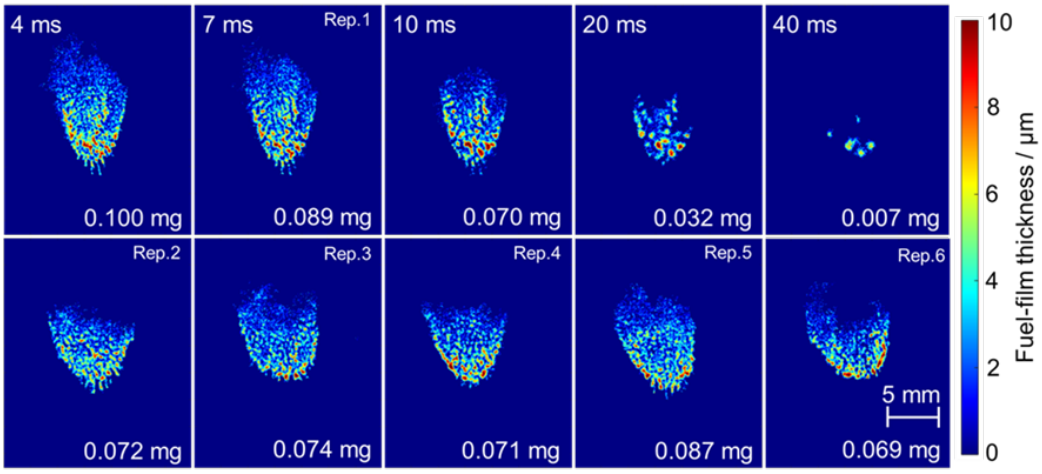

Figure 5.7. (top row) Selected images from a sequence of the vapor-corrected fuel film thickness between 4 and 40 ms. (Bottom row) images from another 5 repetitions of the experiment, each at t = 7 ms aSOI. The total mass of the film is given in the bottom-right corner of each image.

For this fuel film, **Figure 5.8**a plots the average fuel mass in eight injection repetitions. The overall fuel mass injected per spray plume is 1.25 mg. The average fuel mass deposited on the plate is 0.11 mg (at 2 ms aSOI), which is 8.8% of the total injected mass. From 2 ms to 30 ms, the fuel mass decreases by 89%. The maximum vapor mass above the film (i.e., the difference between corrected and uncorrected liquid film mass) peaks with 0.052 mg, or 39 % of the uncorrected liquid-film mass, at 7 ms. The vapor contribution to the absorbance remains significant throughout until the liquid film is no longer detectable at t = 70 ms. **Figure 5.8**b shows that the vapor correction reduces the surface area of the fuel film much less than its mass – less than 10% between t = 2 ms and 25 ms. Nevertheless, the decrease in the liquid surface by correction of vapor absorbance shows that some regions of the as-imaged film only correspond to the absorbance of vapor.

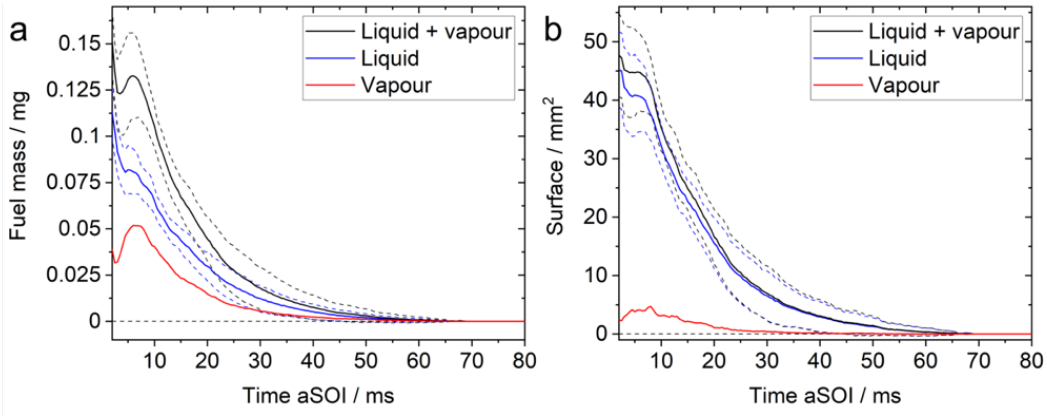

Figure 5.8. Evolution of a) the average fuel film mass, b) the average fuel film surface, each before and after vapor correction (black and blue trace), and the vapor above the film only, i.e, the difference between blue and black traces (red trace). The dashed lines indicate one standard deviation.

5.1.4 Effect of gas/plate temperature and gas pressure in non-firing conditions

A region of interest of 460×320 pixels containing a single liquid fuel-film was defined, as shown in the image of **Figure 5.9**a, and processed without time sub-sampling. The raw UV-absorption images were first filtered with a mean filter (3×3 kernel) to reduce image noise, as shown in **Figure 5.9**b. Then, they were 2×2 binned. Raw UV-absorption images of 230×160 pixels were obtained, as shown in **Figure 5.9**c. All raw images were then dark-subtracted, as shown in in **Figure 5.9**d. Liquid fuel film detection and fuel-vapor correction post-processing algorithms (shown in **Figure 5.4** and **Figure 5.6**, respectively) were applied to the averaged filtered, 2×2 binned, and dark-subtracted images of the selected fuel

film. This section and the next will present a comparison between the results of all non-subsampled data under different experimental conditions.

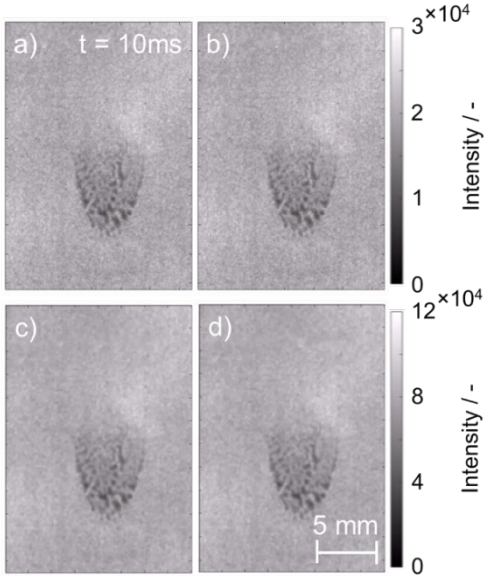

Figure 5.9. Single raw UV-absorption image of a single liquid fuel-film (a), mean filtered raw image (b), 2×2 binned raw image (c) and dark-subtracted raw image (d) at 10 ms aSOI under p = 1 bar and T = 100°C.

Figure 5.10 shows selected images of vapor-corrected fuel film thickness under non-reacting conditions. At ambient pressure, the liquid fuel-film thickness was greater than that at 0.5 and 6 bar. At 1 and 0.5 bar, the fuel-film has sharp defined blobs, and the fuel mass was more concentrated at the fuel-film boundaries, while at 6 bar, the fuel mass was more homogenously distributed over the plate. This is seen at both 50 and 100°C.

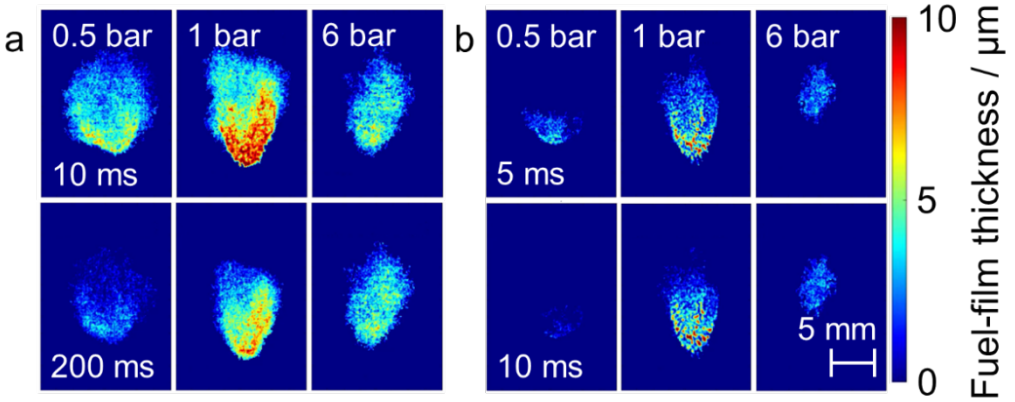

Figure 5.10. Selected images of the vapor-corrected fuel film thickness in single repetitions at three experimental conditions at p = 0.5, 1 and 6 bar (columns from left to right) and two cell temperatures (a) T = 50°C at 10 (top row) and 200 ms (bottom row) aSOI, and (b) 100°C at 5 (top row) and 10 ms (bottom row) aSOI.

Figure 5.11 shows the evolution of the average vapor-corrected liquid fuel-film mass at (a) $T = 50°C$ and (b) $T = 100°C$. At 1 bar, the initial fuel-mass was the highest of the three cell pressure cases. The lowest initial fuel-mass was found at 6 bar. At high cell pressure, atomization is better, resulting in faster spray vaporization, slower spray penetration, and low initial fuel masses. At 0.5 bar, the evaporation rate is high because the cell pressure is close to the saturation pressure of the fuel surrogate (as will be shown in **Figure 5.12**).

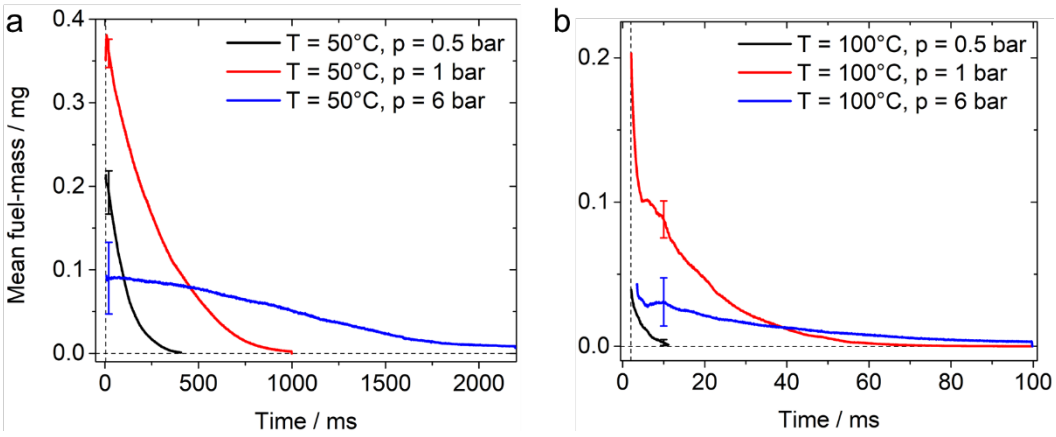

Figure 5.11. Evolution of the average vapor corrected liquid fuel-film mass at $T = 50°C$ (a) and 100°C (b), and $p = 0.5, 1, 6$ bar.

At higher cell temperatures, less liquid fuel-film is deposited on the plate due to increased evaporation of fuel-spray. Temperature has a direct effect on the evaporation rate. At $T = 100°C$, fuel-film evaporation was faster than at $T = 50°C$ due to less fuel film deposited on the plate and greater heat transfer between the fuel films and the plate. Early after injection, the curve of vapor corrected liquid fuel-film mass shows an increase in fuel-mass over time. This physically implausible increase in fuel-film mass might be due to the presence of non-corrected fuel-vapor brought by the spray momentum from the top center of the image out of the field of view down over the deposited fuel film.

Figure 5.12 shows the saturation vapor pressure curve of iso-octane and toluene as a function of temperature. The dots correspond to the experimental cell conditions ($p = 0.5$, 1, and 6 bar). This curve shows the non-linear dependence of the saturation vapor pressure on the temperature. At 100°C and 0.5 bar, the cell pressure is below the saturation vapor pressure. Under these experimental conditions, a fast evaporation time of the liquid fuel-film can be expected. The evaporation time increases when the cell pressure becomes close (1 bar) or higher (6 bar) than the saturation vapor pressure. The cell pressures used at 50°C (0.5, 1, 6 bar) were all higher than the saturation vapor pressure of iso-octane and toluene. The evaporation time of the fuel-film in these cases increases

significantly as the cell pressure increases from 0.5 to 6 bar. At high cell temperatures (150 and 200°C), the cell pressure was below the saturation pressure, except for the experimental condition at T = 150°C and p = 6 bar (close to the saturation pressure). Under these conditions, where the cell temperatures are higher than the boiling temperature of the fuel surrogate, we can expect a different impact regime, and a fast evaporation of the fuel film due to the direct effect of temperature on the evaporation rate.

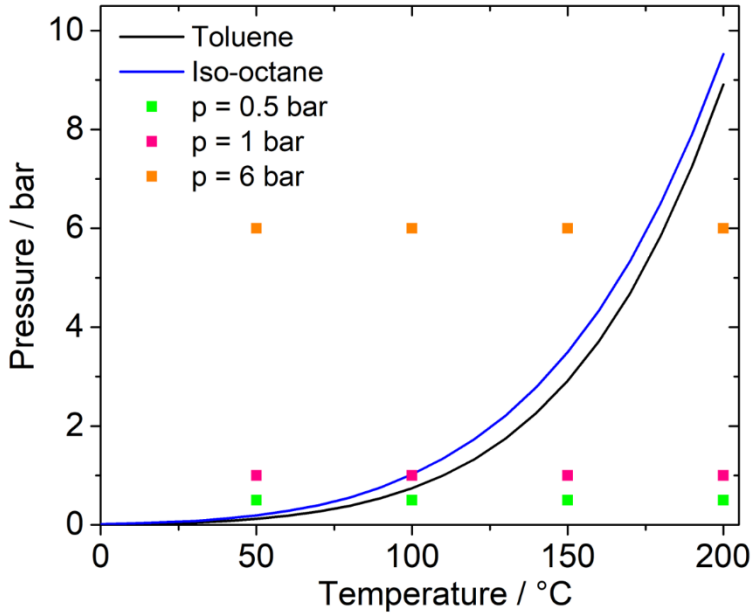

Figure 5.12. Saturation vapor pressure curve of toluene and iso-octane [78].

5.1.5 Non-reacting and reacting cases

Figure 5.13 shows a comparison between fuel-film thickness images under non-reacting (first column) and reacting conditions with a residual oxygen excess ζ = 2% and 15% (second and third columns, respectively). After soot formation under reacting conditions, distinguishing between liquid fuel-film absorbance and the extinction by soot and soot precursors was not possible, as discussed in **section 5.1.1**. Therefore, a quantitative comparison of the fuel-film thicknesses between non-reacting and reacting conditions was only possible before soot formation which occurs at about 32 ms aSOI.

The fuel-film detection algorithm was applied to cases under non-reacting and reacting conditions before soot formation. Under non-reacting conditions, **Figure 5.13** shows sharp well-defined fuel-film blobs. Under reacting conditions, the fuel film appears blurrier than in the non-reacting case. This may be due to the formation of soot precursors. The blurring may also be due to refractive index

gradients caused by the cold film evaporating fuel into the hot post-combustion gases.

Figure 5.13 shows some similarities between the non-reacting (first column) and reacting (second and third columns) cases in terms of fuel-film morphology and evaporation rate. However, the fuel film appears more spread out on the plate under reacting conditions. Greater liquid fuel-film thicknesses are obtained under non-reacting conditions than under reacting conditions. This apparent difference may be due to a reduction in the signal-to-noise ratio under reacting conditions, that could be due to the reduced sensitivity of the camera sensor. Another cause could be the increase in cell temperature due to the propagation of the premixed flame. This would lead to more evaporation of the fuel-surrogate during injection and less liquid fuel-film deposited on the plate. The fuel-film thicknesses in the two reacting cases shown in **Figure 5.13** (second and third columns) are similar. This means that the mass of the deposited fuel film is not affected by the premixed flame and the percentage of excess oxygen.

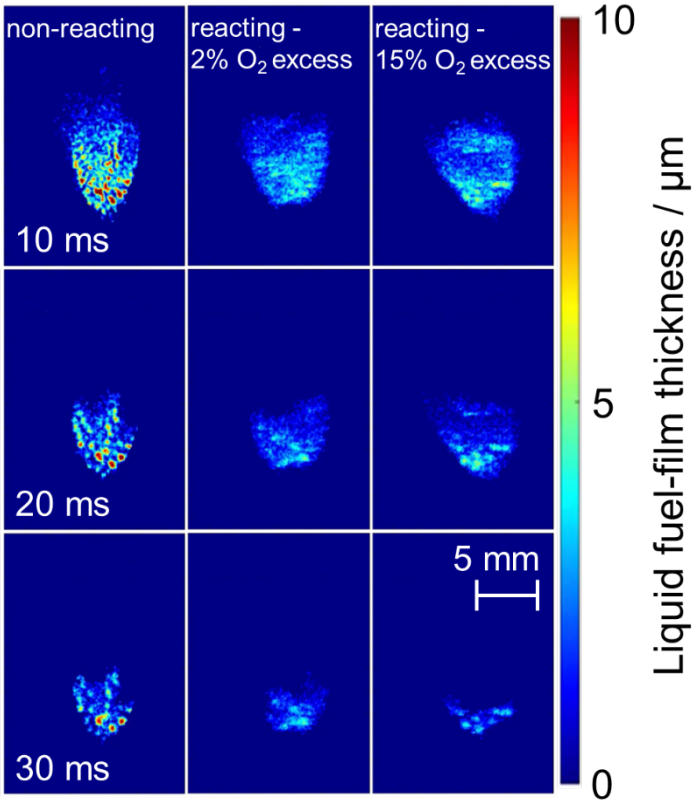

Figure 5.13. Selected images from a sequence of a single repetition vapor-corrected fuel film thickness images at three experimental conditions between 10 and 30 ms aSOI (from top to bottom row, before soot formation) at p = 1 bar and T = 100°C under non-reacting (first column), reacting with 2% of residual O_2 excess (second column) and reacting with 15% of residual O_2 excess conditions (third column).

Figure 5.14 shows the evolution of the mean vapor-corrected liquid fuel-film mass at $T = 100°C$ and $p = 1$ bar under non-reacting (black trace) and reacting conditions with $\zeta = 2\%$ and 15% (red and blue traces, respectively), with and without a fan (solid line and dashed line traces, respectively). The difference in the fuel-film thickness images between the non-reacting and reacting cases was shown in **Figure 5.13**. This difference resulted in a difference in the mean fuel-mass between the two cases, as shown in **Figure 5.14**. The mean fuel-mass under reacting conditions was less than that under non-reacting conditions (about half). However, the evaporation rate between the two cases looks similar. For the reacting case, only the fuel-mass data before soot formation can be quantitatively evaluated. After soot formation (which occurs at about 32 ms aSOI), the extinction by soot and soot precursors added to the absorbance by the liquid fuel-film resulting in a non-physical increase in fuel-mass. In the constant-volume cell experiments, quantitative data of fuel-mass after soot formation cannot be obtained.

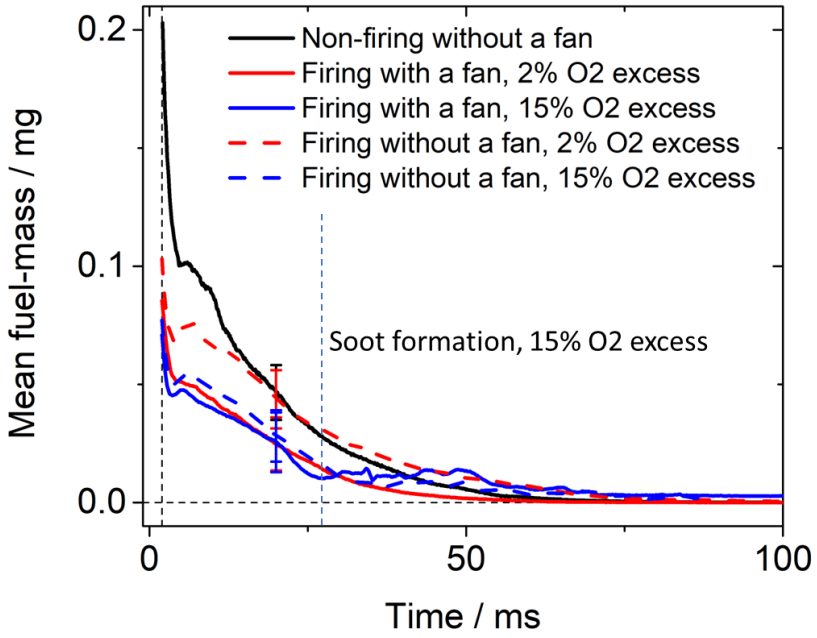

Figure 5.14. Evolution of the average vapor-corrected liquid fuel-film mass at T = 100°C and p = 1 bar under non-reacting and reacting conditions at ζ = 2 and 15% of residual oxygen, with and without a fan (reacting cases).

5.1.6 Soot extinction measurements

Figure 5.15 shows simultaneous measurements of (a) liquid fuel-film thickness and (b) soot-extinction with (c) the horizontal projections of the soot extinction images. The images correspond to two residual oxygen excess ratios, $\zeta = 2\%$ (first row) and 15% (second row), at two times when there is high soot extinction at 124 and 52 ms aSOI, respectively. Under reacting conditions, the premixed

flame propagates towards the plate after ignition. The flame front reaching the wall is quenched. All UV-absorption images show the presence of a fuel film when the premixed-flame front reaches the plate. The flame encounters a locally rich vapor plume above the fuel-film. The interaction between the premixed flame and the evaporating fuel-film develops into a diffusion-like flame, powered by the residual oxygen excess remaining in the premixed flame burnt gases. Chemak [79] studied numerically the interaction between the premixed flame and the deposited fuel film and found the formation of rich vapor regions above the fuel films causing soot formation.

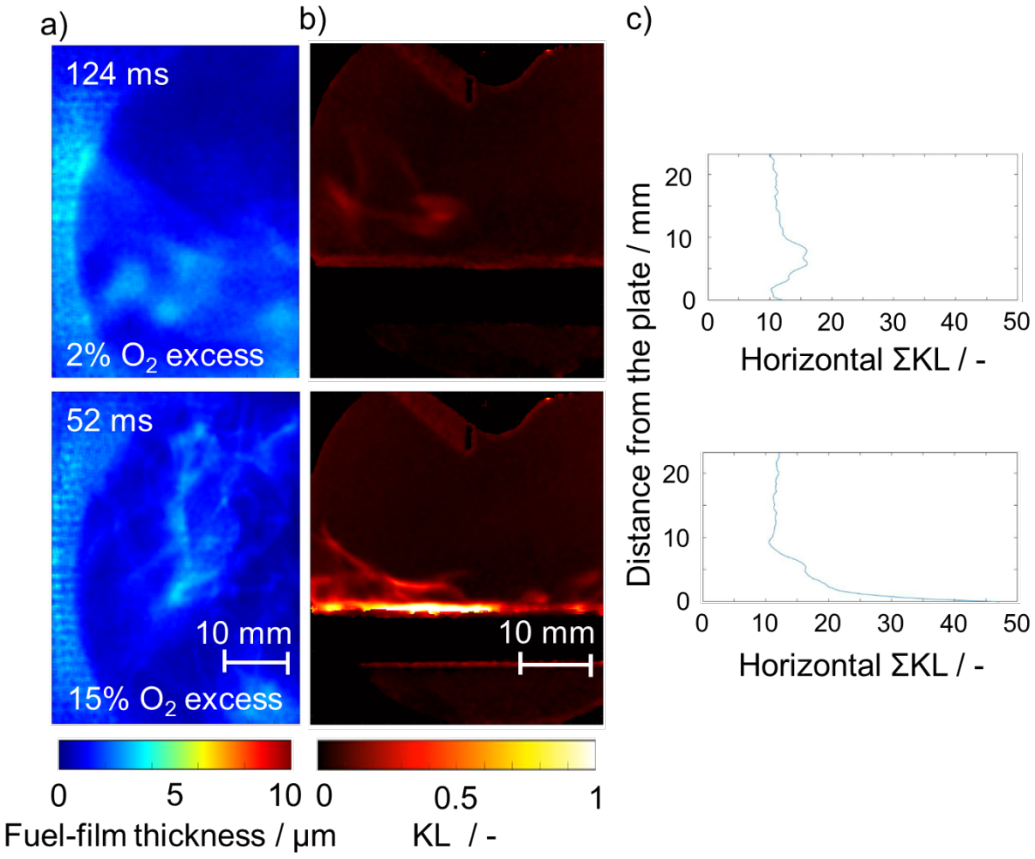

Figure 5.15. Simultaneous acquisition of (a) liquid fuel-film thickness (top view) and (b) DBI soot extinction (side view) images at 2% (first row) and 15% (second row) of residual oxygen excess, and (c) their horizontal *KL* profile projection.

The soot extinction images show that the percentage of oxygen-excess affected the flame arrival time and the spatial distribution of soot above the plate: the premixed flame arrived earlier, and soot formed closer to the plate at high residual oxygen excess with higher soot extinction than at low residual oxygen excess. From direct visualization of the average DBI images, the flame arrived at about 32 ms aSOI at $\zeta = 15\%$ with high soot extinction concentrated near the

plate, between 0 and 10 mm from the plate (**Figure 5.15**c, bottom row). At $\zeta = 2\%$, the flame front arrived at the plate at about 70 ms aSOI with low soot extinction forming far away from the plate, between 5 and 10 mm from the plate (**Figure 5.15**c, top row).

In the case of a low residual oxygen excess ($\zeta = 2\%$), the premixed flame consumes the fuel-vapor in a quasi-stoichiometric condition, resulting in low soot extinction. In the case of a high residual oxygen excess ($\zeta = 15\%$), the diffusion flame is driven by more oxygen excess in the presence of locally rich fuel vapor. This allowed the flame with a high residual oxygen excess to propagate closer to the wall before quenching, resulting in greater interaction between the flame and the fuel vapor with greater soot extinction formed near the plate.

5.2 Constant-flow facility experiments

5.2.1 Soot and soot-precursor extinction

First, liquid fuel-film regions were detected using the morphological algorithm previously developed for the constant-volume cell experiments and adapted later to the constant-flow facility experiments as demonstrated in **section 8.1.2**

Extinction by soot and soot precursors is wavelength-dependent. Since the idea is to correct for the soot extinction at 265 nm based on the images at the other three wavelengths, we need to find this dependence for our case. This is achieved by identifying regions next to the film where the extinction at all four LED wavelengths is only from soot. To this end a specific algorithm was put in place to detect automatically the soot “pockets” not interfering with liquid film absorption.

After STM2 masks are calculated and the liquid fuel-film is detected in the absorbance images at 265 nm, the corresponding region of liquid fuel-film is then masked out in the images at all wavelengths, as indicated in **Figure 5.16**. The remaining soot-absorbance regions are narrowed further by a threshold based on the background noise, and soot regions covering less than 300 pixels are discarded. Sensitivity studies were performed to check the intermediate and final outputs of the algorithm, such as fuel-film and soot masks, by visual inspection.

As an example, **Figure 5.16** shows the resulting masked absorbance images in a single injection repetition (rep. 1) at $t = 45.7$ ms aSOI obtained with FS1. Clearly, the soot absorbance decreases as the wavelength increases.

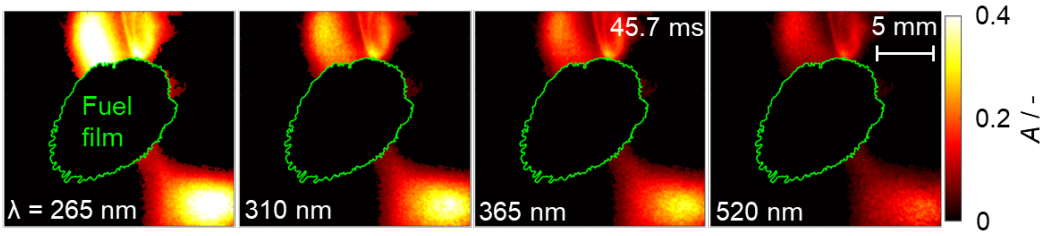

Figure 5.16. Example of absorbance images show sooting regions near the fuel film at 265, 310, 365, and 520 nm and at 45.7 ms aSOI. The green line indicates the outline of the liquid film found by image segmentation [71].

The absorbance in different regions may vary not only due to differences in concentration but also in soot maturity or particle size [66]. To isolate the influence of the latter two, the soot absorbance images were normalized to the soot absorbance at $\lambda = 265$ nm and time t. **Figure 5.17** shows an example with thresholded soot regions near the fuel film from top to bottom at three different times aSOI. Two soot regions can be distinguished: a soot region at the top of the image formed near the fuel film and another at the bottom of the image formed outside from a different fuel film but displaced in the image field of view. The soot region at the top of the image has low $A_\lambda/A_{265\,nm}$ values, corresponding to nascent soot forming near the fuel-film, compared to the high $A_\lambda/A_{265\,nm}$ values of the soot regions at the bottom of the image, corresponding to aging soot formed from a different fuel-film located outside the image field-of-view. In each sequence, the $A_\lambda/A_{265\,nm}$ normalized absorbance values at 265, 310, 365, and 520 nm were averaged spatially (within the thresholded regions) and temporally (while aSOI soot is present).

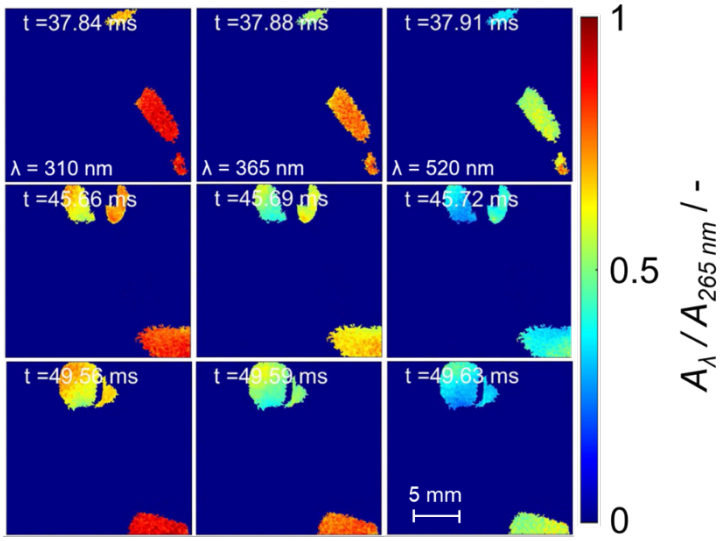

Figure 5.17. Example of absorbance images at λ = 310, 365, 520 nm normalized to the absorbance image at 265 nm showing thresholded soot regions near the fuel film at 37.9, 45.7, 49.6 ms aSOI (from top to bottom).

Figure 5.18 shows the spatio-temporally averaged absorbance with respect to that at 265 nm, averaged over all 16 injection repetitions with FS1 and FS2. The trend of decreasing extinction with increasing wavelength with both fuel surrogates is consistent with the literature [16,80]. The data from **Figure 5.18** are used to infer the soot extinction at 265 nm from that at a longer wavelength, as discussed next.

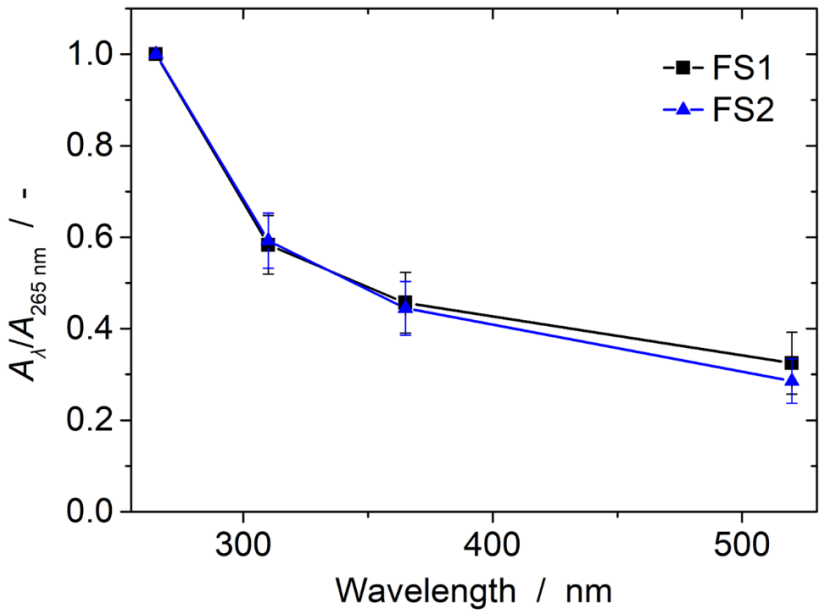

Figure 5.18. Spatio-temporally averaged absorbance A with respect to that at 265 nm. The error bars indicate the standard deviation among 16 injection repetitions with FS1 (black) and FS2 (blue).

5.2.2 Correction of absorbance interferences

The fuel-film thickness is determined from the absorbance images (see **Equation (4.6)**) at 265 and 310 nm. Column a in **Figure 5.19** shows uncorrected absorbance images at 265 nm and the two times aSOI already considered in **Figure 4.14**. The flame front passes through the test section between 2 and 12 ms aSOI such that soot is not present at 5.1 ms aSOI (row I), but is at 45.7 ms aSOI (row II).

Column b shows “absorbance” from scattering at the fuel-film surface (b I) and soot (b II) at 310 nm. Before soot absorbance appears in the images (row I) or under non-reacting conditions, the absorbance image at 310 nm is simply subtracted from that at 265 nm (a I), yielding c I. When soot interferes with the fuel signal (row II), the image at 310 nm (b II) is multiplied by factor A265 / A310 and then subtracted from the image at 265 nm (a II) yielding the image shown in c II. The factor A265 / A310 (A265 / A310 = 1.71 and 1.69 for

FS1 and FS2, respectively) is the reciprocal of the relative extinction A310 / A265, as shown in **Figure 5.18**. The absorbance images at 310 nm were chosen because 310 nm is closest to 265 nm, and signal-to-noise is good in these images.

In a last step, the absorbance of toluene vapor is subtracted. Distinguishing between slowly drifting vapor clouds and the stationary, ever-shrinking liquid film in image sequences was the original purpose of the morphological algorithm schematically shown in **Figure 8.6 (Appendix section)**. The fuel-vapor approximation algorithm was applied to the scattering- or soot-corrected image sequence represented by column c in **Figure 5.19**. Similarly as in **section 5.1.2**, it interpolates the vapor absorbance found just outside of the edges of the fuel film bilinearly into the interior of the film, yielding the images in column d which are then subtracted from those in c, and multiplied with the calibration constant of 37 µm, calculated in **Section 4.4**, yielding the final film thickness images in column e. Note that all corrections except for dark subtraction were done after converting the images to absorbance, making the variation in the intensifier's spectral response irrelevant.

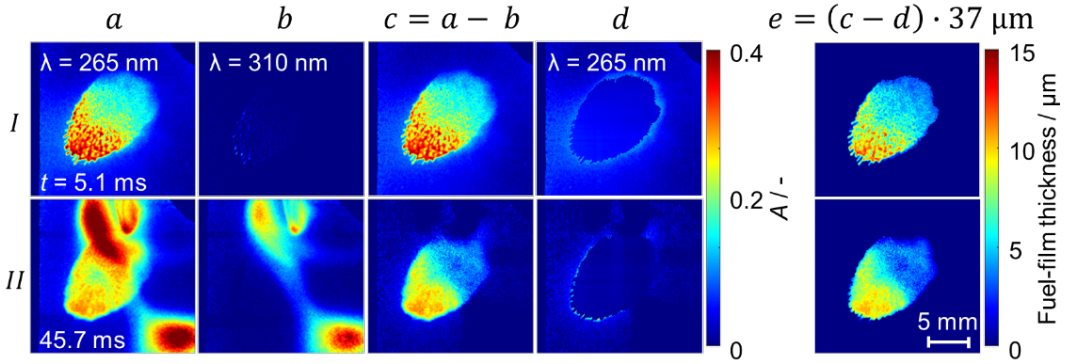

Figure 5.19. Absorbance images at 265 nm (a), adjusted absorbance images at 310 nm, representing scattering (b I) and scattering and soot (b II), corrected absorbance images (c), interpolated vapor absorbance (d), and film-thickness images (e) corrected for scattering, soot, and fuel vapor, and calculated via the in-situ calibration equation, $d = 37\ \mu m\ A$.

5.2.3 Non-reacting and reacting cases

Figure 5.20 shows selected single-shot images from sequences of film images under reacting and non-reacting conditions with FS1 (the latter achieved by not igniting). For the reacting case, uncorrected and corrected images are shown. Between 3 and 10 ms aSOI, the fuel films in both cases are very uneven, with thick fuel "blobs", consistent with the literature [36,60]. In the reacting case, the uncorrected images show fuel vapor representing an equivalent film-thickness of

up to 4 µm at early times aSOI. From 20 ms aSOI onward soot is detected. Soot formation increases with time, resulting in strong absorbance near and over the fuel film between 45 and 60 ms aSOI before soot vanishes 100 ms aSOI. Nevertheless, the extinction by soot and vapor absorbance appears to be accurately removed in the corrected images.

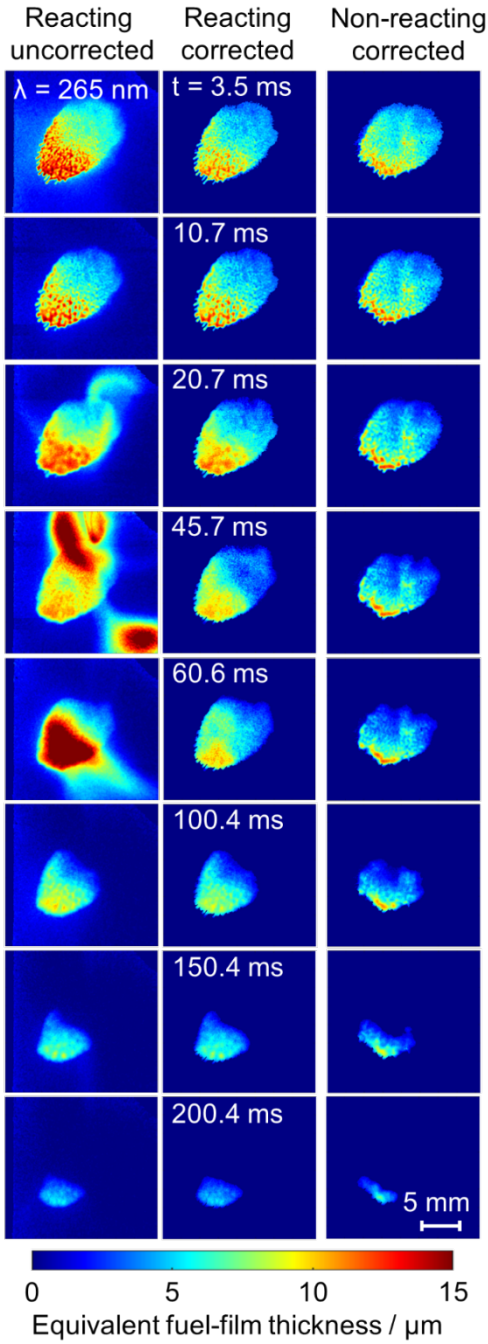

Figure 5.20. Single-shot sequences of equivalent fuel-film thickness images for fuel surrogate FS1 under reacting (uncorrected and corrected images) and non-reacting conditions.

In the reacting case, from 20 ms aSOI onward the film surface structure appears blurry in contrast to the images from non-reacting conditions, where the film retains its sharply defined blobs. The difference in the fuel-film structure between reacting and non-reacting conditions might come from PAH and other soot precursors forming just above the film. If these species absorb light relatively stronger at 265 nm than the soot next to the film, on which the correction factor A265 / A310 is based, they are not properly taken into account in the "soot" correction. This is in fact likely, since small PAH strongly absorb in the deep UV [75,81]. The blurring may also be caused by index-of-refraction gradients caused by the cold film evaporating fuel into the hot post-combustion gases.

Figure 5.21 shows the evolution of the film mass from uncorrected, soot-corrected, and soot + vapor-corrected images under reacting conditions, and from uncorrected and vapor-corrected images under non-reacting conditions with FS1. The effect of scattering was little under all conditions (< 3%) and is thus not separately shown in **Figure 5.21**. The data represents averages from 16 single injection repetitions. Image correction before the appearance of soot at about 3.5 ms aSOI (i.e., accounting solely for vapor absorption) reduces the film mass by about 25% under both reacting and non-reacting conditions, yielding similar initial masses of 0.42 and 0.38 mg, respectively. Under reacting conditions, substantial interference from soot causes an artificial increase in the film mass derived from the uncorrected images between 10 and 30 ms aSOI. In contrast, the film mass derived from corrected images monotonically decreases. It is 30% lower than that from uncorrected images at 34 ms aSOI. The variation among injection repetitions is also reduced.

From around 10 ms aSOI onward, the fuel mass measured under reacting conditions is greater than under non-reacting conditions. This physically implausible result is most presumably due to absorbance by small-size PAH close to the film surface, which is not properly corrected, as discussed above. This effect was observed in the fuel-mass data in the constant-volume cell results but late aSOI. An increase in fuel-mass was observed after soot formation (when t was greater than 32 ms aSOI). However, from about 50 ms aSOI on, in **Figure 5.21**, the evaporation rates (the slope of the traces) become similar again and the fuel films have completely evaporated at 280 ms aSOI under both reacting and non-reacting conditions.

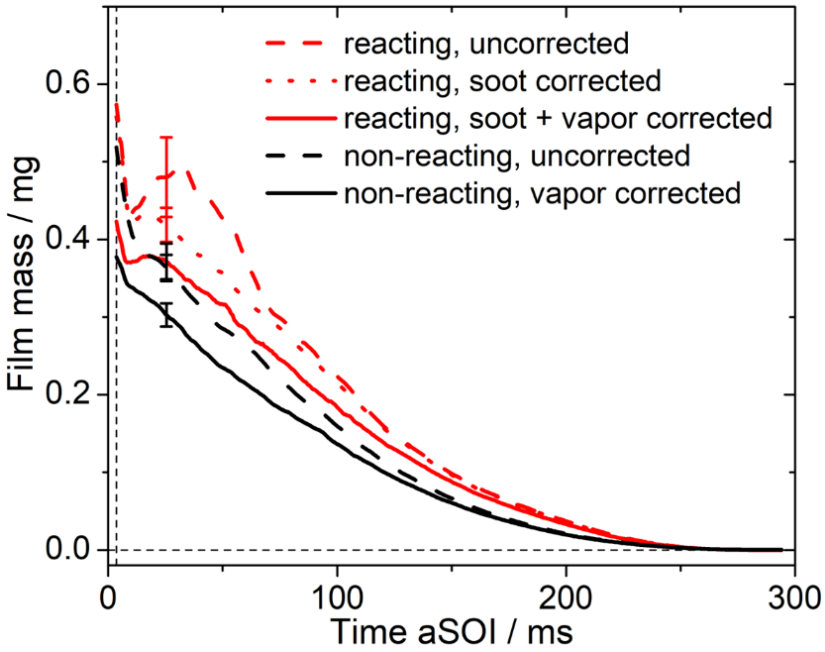

Figure 5.21. Fuel-film mass versus time aSOI, from uncorrected and corrected images, under reacting and non-reacting conditions with FS1. Error bars indicate the standard deviation among 16 individual injections.

5.2.4 Comparison of film evaporation between two fuel-surrogates

All results discussed so far correspond to fuel-surrogate FS1, consisting of 70% iso-octane - 30% toluene. FS2, consisting of 60% iso-octane – 30% toluene – 10% n-octane, was also used as a fuel surrogate to reduce the variation in toluene concentration during the evaporation process. Experiments under non-reacting and reacting conditions were performed in the constant flow-facility. Absorbance images of FS2 were calculated and corrected as for FS1.

Figure 5.22 shows selected single-shot images from sequences of film images under reacting and non-reacting conditions with FS2. Prior to soot formation (before 10 ms aSOI), the fuel thickness images show a significant contribution from vapor similar to that found with FS1 (up to 4 µm). Under non-reacting conditions, the contributions from vapor and scattering were maximal at 3.5 ms aSOI (up to 5 µm). Soot is detected from 20 ms aSOI. Soot formation results in strong absorbance near and over the fuel film between 20 and 100 ms aSOI before soot disappears at 100 ms aSOI. Under reacting conditions, soot and vapor contributions were maximum at 34 ms aSOI (up to 5 µm).

The corrected reacting and non-reacting cases show a thin fuel blob structure during evaporation of the fuel-film. FS2-film retains its well-defined blob structure even under reacting conditions. This could be related to the composition

of the deposited fuel mixture during the fuel-flame interaction. Toluene is an aromatic hydrocarbon and is known to produce high levels of soot during combustion. Higher toluene concentrations in the fuel mixture may result in higher levels of soot formation. **Figure 4.19**, shown in **section 4.3.2**, shows an increase in toluene concentration in the mixture during evaporation of both fuel surrogates. For FS2, the toluene concentration increases by only 10%, compared to 75% for FS1, until 98% of the fuel mixture is evaporated before it starts decreasing. This means that higher levels of toluene might be present in FS1 composition during the fuel-flame interaction, resulting in higher soot formation, which explains higher levels of PAH and other precursors forming above FS1-film and blurring its structure. However, FS2 showed less soot formation above and near the fuel-film compared to FS1. The blurring of the FS2 film structure was less significant, which might be related to low levels of PAH forming above the fuel-film. Soot was accurately corrected and removed in the FS2 corrected thickness images, where the correction factor A265 / A310 = 1.69, a factor close to that found with FS1.

Figure 5.23 shows a time sequence of averaged equivalent fuel-film thickness images for the two fuel surrogates FS1 and FS2. These images show the repeatability of the experiments performed under reacting and non-reacting conditions and for both fuel surrogates. The fuel-film was impinged in the same region, with a similar order of thickness from one repetition to another. For one fuel surrogate (FS1 or FS2), the fuel-film morphology was similar between reacting and non-reacting conditions, with high fuel thicknesses accumulated on the outer boundaries of the fuel-film.

Comparing the thickness images of FS1 and FS2, the thickness of FS1 was generally twice that of FS2. The surface of FS2 appears smaller and thinner than FS1. During the fuel-film evaporation, the evaporation rate of both fuel surrogates was similar. At 200 ms aSOI, the FS2 film evaporated completely in both reacting and non-reacting cases. However, the FS1 film was still detected on the plate until about 270 ms aSOI. A detailed comparison of the evaporation rate evolution over time between the two fuel surrogates will be presented in **section 5.2.5**.

The averaged fuel thickness images show that the difference in thickness between FS1 and FS2 is not related to the repeatability at a given experimental condition, but could be related to the composition of the fuel-surrogate after deposition on the plate and during evaporation. The difference in fuel thickness between FS1 and FS2 will be further investigated at the end of this section.

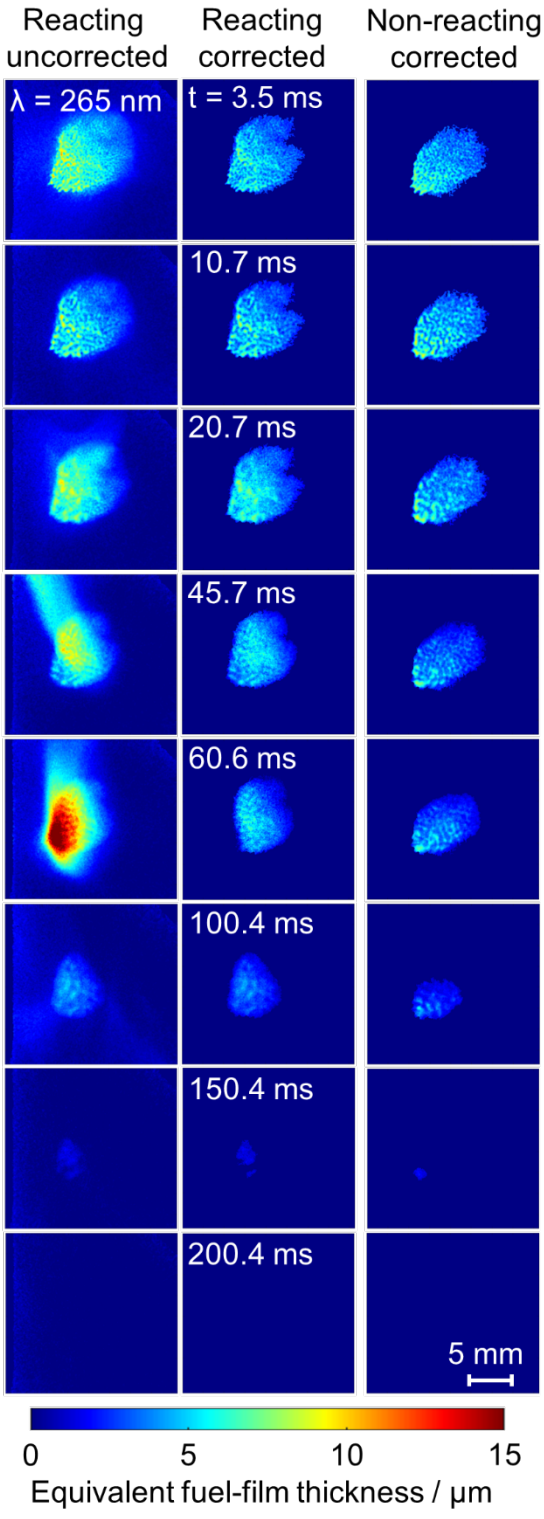

Figure 5.22. Single-shot sequences of equivalent fuel-film thickness images for fuel surrogate FS1 under reacting (uncorrected and corrected images) and non-reacting conditions.

Figure 5.24 shows the temporal evolution of the corrected fuel-mass with the two fuel surrogates FS1 and FS2 under reacting and non-reacting conditions. In general, the mass of FS1 was about 50% greater than that of FS2. This difference in fuel mass between the two fuel surrogates will be evaluated in the following paragraph. Under reacting conditions, FS2 did not show an increase in fuel-mass early after injection. This is may be due to less soot produced with FS2 than with FS1, which adds less soot contribution to the absorbance images and therefore does not affect the evolution of fuel-mass as much. As with FS1, the fuel mass of FS2 was higher under reacting conditions than under non-reacting conditions, again possibly due to small-size PAHs.

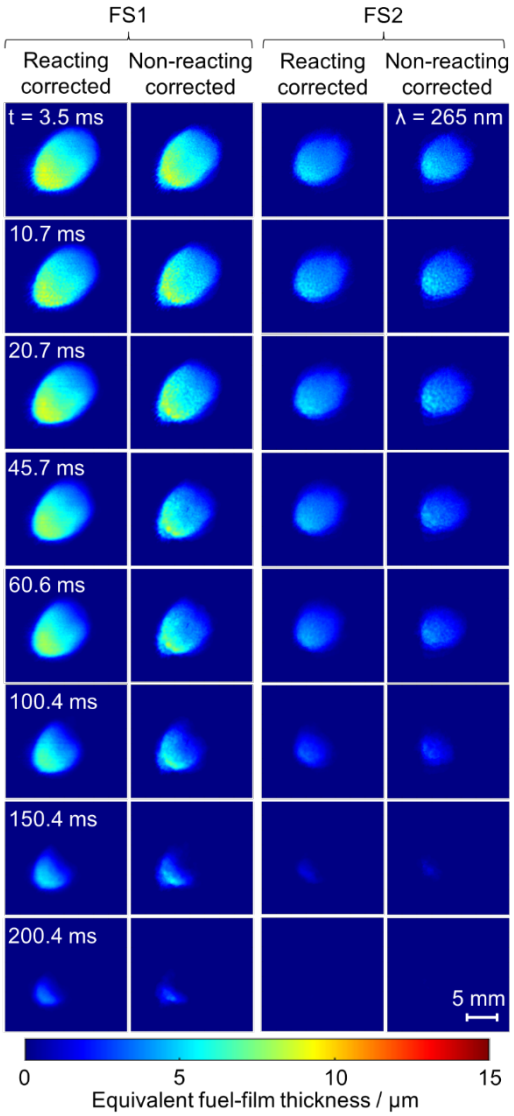

Figure 5.23. Time sequence of equivalent fuel-film thickness images for fuel surrogate FS1 (first and second columns) and FS2 (third and fourth columns) averaged among 16 repetitions under reacting conditions and 10 repetitions under non-reacting conditions.

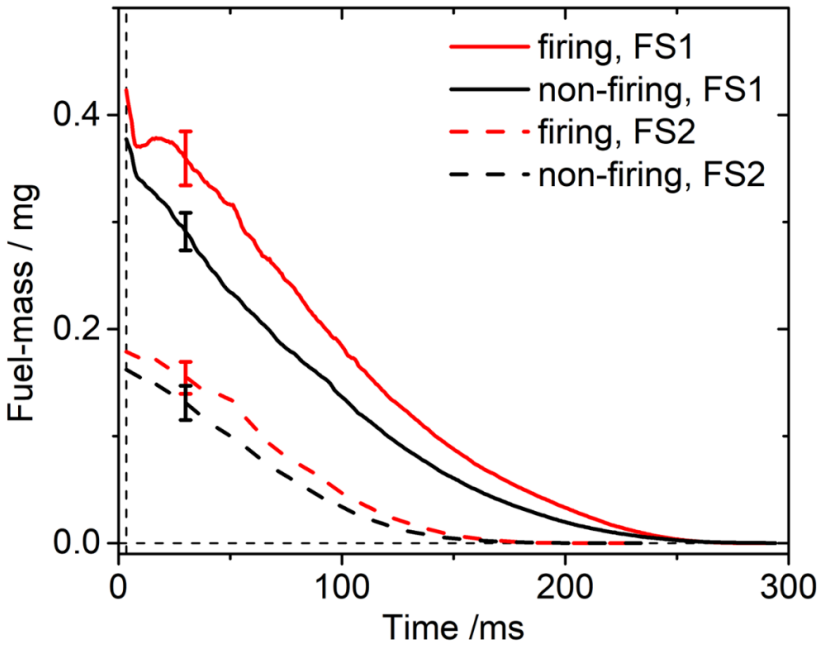

Figure 5.24. Fuel-film mass versus time aSOI, from corrected images, under reacting and non-reacting with FS1 and FS2. Error bars indicate the standard deviation among 16 (reacting) and 10 (non-reacting) individual injections.

The total injected mass was determined by mass flow rate measurements [49] as 9.3 mg for an injection duration $t_{injection}$ = 1 ms and an injection pressure p_{inj} = 100 bar. Assuming that the total injected fuel mass of 9.3 mg is distributed evenly over the six single sprays, each spray contains approximately m_{spray} = 1.55 mg. The initial fuel-masses were determined from the images of the liquid fuel-film thickness after fuel was fully deposited on the plate at 3.5 ms. The fuel masses in the four studied cases were $m_{FS1,\ comb}$ = 0.42 mg, $m_{FS1,\ inert}$ = 0.38 mg, $m_{FS2,\ comb}$ = 0.18 mg, $m_{FS2,\ inert}$ = 0.16 mg. This means that 73, 76, 88, and 90 % of the fuel is evaporated before reaching the wall. For these evaporated fuel percentages, the toluene volume fraction is expected to be different from its initial value of 0.3 due to preferential evaporation. However, the toluene volume fraction can be approximated from the preferential evaporation trace, shown previously in **Figure 4.19**. The new initial toluene volume fractions obtained from the trace will correspond to different evaporated fuel percentages. Assuming that all the liquid that impacts the plate, remains on the wall (no rebound, no slip), and that the deposited fuel-film evaporates at equilibrium, an iterative algorithm was developed to take the effect of the preferential evaporation on the variation of toluene concentration into account for the initial fuel-mass. In this case, data from the preferential evaporation trace at equilibrium in **Figure 4.19** can be used to calculate the volume fraction of toluene at a certain evaporated fuel percentage.

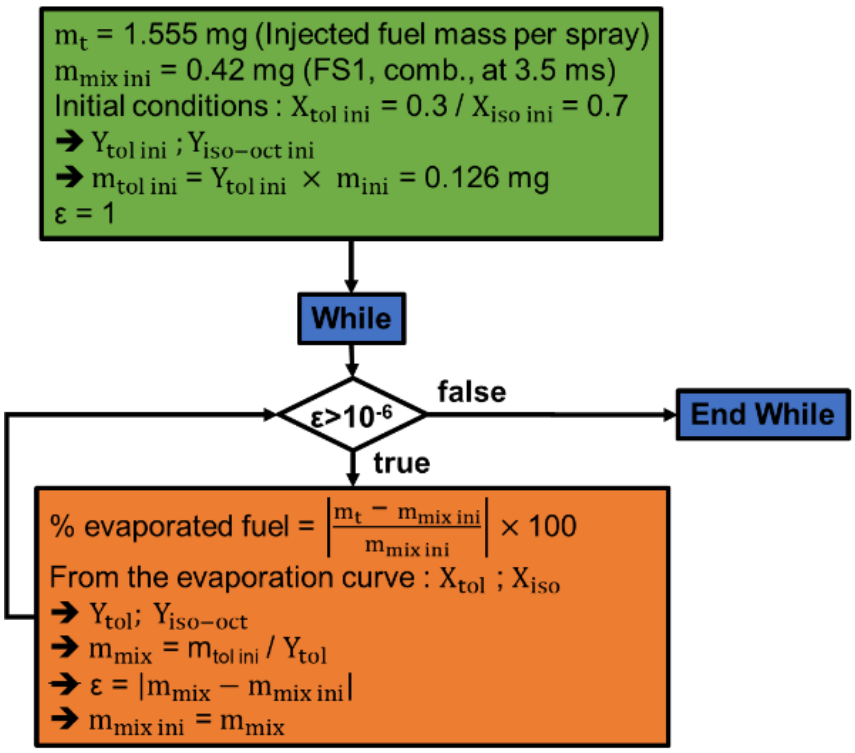

Figure 5.25. Algorithm schematic for the approximation of the initial deposited fuel mass taking into account variation of toluene concentration. The example corresponds to the case under reacting conditions with FS1.

Figure 5.25 shows a schematic of the algorithm. The example in this figure corresponds to the case under reacting conditions with FS1. The inputs to the algorithm are the total fuel-mass injected per spray, the initial deposited fuel-mass, and the initial toluene mass. From **Figure 4.19,** for a certain initial evaporated fuel percentage, a new toluene volume fraction and a new initial fuel-mass can be determined.

The algorithm compares between the initial fuel-mass and the newly calculated "iterated" initial fuel-mass deduced from the evaporation curve in **Figure 4.19**. If the difference between the two masses is large ($>10^{-6}$ mg), the algorithm replaces the initial fuel-mass with the new "iterated" initial fuel-mass and begins further iterations until the difference between the initial fuel-mass and the new "iterated" fuel-mass is small ($<10^{-6}$ mg). Convergence was reached after eight iterations to within 78% of initial evaporated fuel percentage for FS1, and after four iterations to within 90% of initial evaporated fuel percentage for FS2. This means that the difference between the two initial masses of the two fuel surrogates is not only related to the preferential evaporation effect, but that other factors, which need to be investigated further, may contribute to this difference.

5.2.5 Evaporation rate

The evaporation rate was calculated as indicated in **Equation (5.1)** from the difference between two consecutive thickness images *d* acquired at times t_1 and t_2:

$$\text{Evaporation rate(t)} = \frac{d(t_2) - d(t_1)}{t_2 - t_1}\ (\mu\text{m ms}^{-1}),\ \text{and t} = \frac{t_1 + t_2}{2}\ (\text{ms}) \qquad (5.1)$$

Prior to the calculation of the thickness images, the raw images were first block time-averaged in blocks of five images to improve the signal-to-noise ratio, as described in **section 4.2.4**. To further reduce noise, the fuel-film thickness images were block time-averaged again in blocks of five images for the calculation of evaporation rate. In total, evaporation rate results shown here were calculated from time blocks of 25 images.

Figure 5.26 shows the evaporation rates with FS1 and FS2 under reacting and non-reacting conditions. The two fuel surrogates have similar evaporation rates and fuel-films become thinner as they evaporate.

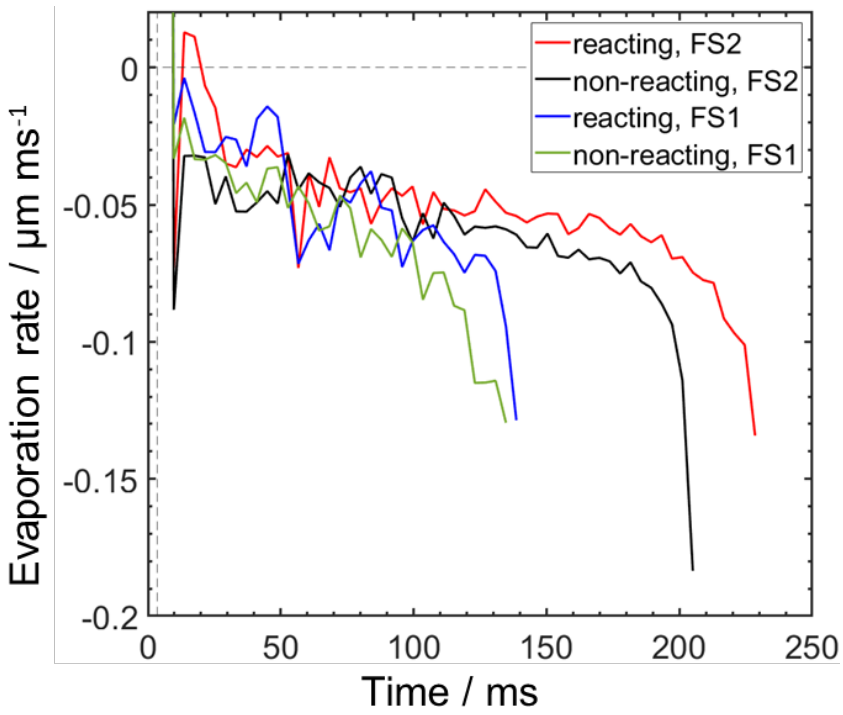

Figure 5.26. Evolution of mean evaporation rate with FS1 and FS2 from all repetitions under reacting (16 repetitions) and non-reacting (10 repetitions).

The thinner thicknesses, especially at the edges of our blob-structured fuel films, resulted in higher evaporation rates. This result is consistent with that of Maligne and Bruneaux [39], who measured a higher evaporation rate in discrete pocket

fuel-film structures than in continuous film structures. In his model, Chemak [79] found that as the fuel film thickness decreases, the liquid fuel-film temperature increases and approaches the plate temperature, resulting in an increase in the evaporation rate, which is consistent with our results. Just before the end of fuel-film evaporation, the evaporation rate became faster (two to three times its initial value) for all four cases. Similar trends in the evaporation rate, especially just before the end of fuel-film evaporation, were obtained in Chemak's thesis [79].

6 Conclusions

In this thesis, the fuel-film formation and evaporation, as well as the interaction between the fuel-films and the premixed flame were studied experimentally. For this purpose, two experimental parameters, liquid fuel-film thickness and soot extinction, were studied using optical diagnostics. The light absorption technique was adopted to measure the liquid fuel-film thickness. The DBI technique was used to measure the soot extinction. The experiments were performed in two thermodynamically controlled environments: a constant-volume cell at IFPEN and a constant-flow facility at UDE, under non-reacting and reacting conditions. The liquid fuel-film thickness was determined from toluene absorption around 265 nm. Two fuel surrogates were used, the first one consisted of 70% iso-octane and 30% toluene, and the second of 60% iso-octane, 30% toluene and 10% n-octane.

At IFPEN, spatio-temporally resolved measurements of the liquid fuel-film thickness on a transparent plate after spray impingement were obtained by UV absorption, using high-speed imaging under non-reacting and reacting conditions. Fuel-film thickness was determined from toluene absorption around 265 nm. Soot extinction images were acquired simultaneously with fuel-film thickness images in the orthogonal line-of-sight direction.

At UDE, a time-multiplexed multi-spectral diagnostic technique based on absorption of UV and visible light was developed to image the thickness of combusting fuel-films in the presence of fuel vapor and soot. The technique was developed on the basis of the single-wavelength UV absorption technique used at IFPEN. In the single wavelength UV absorption technique (at 265 nm), light-scattering and soot extinction made fuel-thickness quantification difficult. The absorbance images showed a significant contribution from soot extinction after soot formation, making the field of view optically dense. The UV-vis absorption technique allows to distinguish and correct the different contributions present in the absorbance images that interfere with the quantitative measurements of liquid fuel-film thickness. The developed technique is based on the quasi-simultaneous acquisition of absorbance images at multiple wavelengths (here, 265, 310, 365, and 520 nm) using inexpensive LEDs a high-speed camera. The additional wavelengths (different than 265 nm) are used to differentiate scattering and absorption in the fuel film as well as light extinction by soot and precursors. The multi-spectral approach permitted obtaining spatio-temporally resolved fuel-film thickness measurements and additional information on the soot.

A morphological post-processing algorithm was developed to detect liquid fuel-films in the absorbance images and to correct for the vapor contribution. The

absorbance images were converted to fuel-film thickness images via a proportionality relationship calculated from the in-situ calibration equation $d = A \cdot 37$ µm. This equation was similar in the two experimental campaigns and with both fuel surrogates (containing 30%-vol. toluene). The global parameters of thickness and mass of one fuel-spray were obtained.

In the constant volume cell (at IFPEN), fuel-film thickness images were calculated using the single-wavelength UV absorption technique from the dark-subtracted absorbance images at 265 nm. Under non-reacting conditions, fuel-film thickness images were calculated at different cell temperatures and pressures. At high temperatures, the evaporation of the fuel-film was very fast, due to thinner fuel-film thicknesses deposited on the plate. At high cell pressures, above saturation pressure, better fuel spray atomization was achieved with small fuel-film thicknesses, but with slow evaporation. Under sub-atmospheric pressure, close to the saturation pressure, small fuel-film thicknesses were obtained with fast evaporation. Under reacting conditions, DBI images showed that the residual oxygen excess percentage affected the flame arrival time and soot spatial distribution. In the high residual oxygen excess case, the premixed flame arrived earlier and formed soot closer to the plate with higher soot extinction than in the low residual oxygen excess case.

In the constant flow facility (at UDE), the developed multi-spectral technique quantified the different uncertainties that are not related to the absorbance of the liquid fuel-film. One experimental condition was adopted at $p = 1$ bar and $T = 100$°C. The subtraction of a dark frame (all LEDs off) in every imaging cycle corrected natural soot incandescence in all images. To correct light scattering at the liquid film absorbance images at 310 nm were used. This is in a spectral region close to 265 nm but where absorption by toluene is very low. Correcting light scattering at the film was found to be of minor importance for the thickness quantification (< 3% in total film mass). LEDs at 310, 365, and 520 nm were used to determine the wavelength-dependent absorbance of soot and soot precursors. The result was used to infer absorbance at 265 nm from that at 310 nm and subtract it. This correction substantially improves the film-thickness quantification in the presence of soot (up to 30% in total film mass). However, even in entirely corrected images, the film-thickness images appear blurrier and the film mass is higher under reacting than under non-reacting conditions. Most likely, this is from absorbance by small-size PAH over the film that is not detected at 310 nm. Adding further deep-UV LEDs to the illumination scheme may enable including such small PAH in the “soot” correction. Vapor contribution was about 25% of the absorbance signal under reacting and non-reacting conditions.

After direct injection, the liquid fuel-films start to form on the wall and evaporate. After ignition, the premixed flame propagates towards the wall. The flame front reaches the wall and starts quenching, but encounters locally rich vapor zones above the liquid fuel-films. The interaction between the premixed flame and the evaporating fuel-films turns into diffusion like flame powered by the residual oxygen excess in the premixed flame burnt gases leading to soot formation.

Other uncertainties related to the absorption technique were assessed. Uncertainty related to preferential evaporation decreased by 65% when using the second fuel-surrogate at 98% of the evaporated fuel. A small effect was attributed to temperature on the absorption technique of 7% after increasing ambient temperature by 40°C. The effect of pressure was not studied but was assumed to be negligible.

No parametric variations were performed in the constant-flow facility, however the UV-vis absorption technique focused on quantifying the fuel-film thickness. In this context, the technique developed here can be used to image the temporally resolved fuel-film evaporation rate in combustion and its dependence on experimental conditions. But the simultaneous imaging of soot extinction at multiple wavelengths has the potential to provide additional information on the local soot maturity. In the end, this technique can be adapted in later studies of fuel-film flame interaction in the constant volume cell.

7 Bibliography

7.1 References

[1] Grand view research, Internal combustion engine market size, share & trends analysis report by fuel (petroleum and natural gas), by end-use, by region, and segment forecasts, 2018 - 2020, available at <https://www.grandviewresearch.com/industry-analysis/internal-combustion-engine-market>, (5 November 2021).

[2] J. Heywood, Internal Combustion Engines Fundamentals, McGraw-Hill Education, 1st edition, New York, 1988.

[3] K. Rainer, Particle alert for direct-injection gasoline cars Soot particles from GDI engines, 2017, available at <https://www.empa.ch/web/s604/soot-particles-from-gdi>, (10 November 2021).

[4] M. Raza, L. Chen, F. Leach, S. Ding, A Review of Particulate Number (PN) Emissions from Gasoline Direct Injection (GDI) Engines and Their Control Techniques, Energies 11 (6) (2018) 1417.

[5] M.C. Drake, T.D. Fansler, A.S. Solomon, G.A. Szekely, JR, Piston fuel films as a source of smoke and hydrocarbon emissions from a wall-controlled spark-ignited direct-injection engine, SAE Tech. Pap. 2003-01-0547 (2003).

[6] E. Stevens and R. Steeper, Piston wetting in an optical DISI engine fuel films, pool fires, and soot generation, SAE Tech. Pap. 2001-01-1203 (2001).

[7] P. Mock, European vehicle market statistics 2018/2019, The international council on clean transportation, 2018, available at <https://theicct.org/publication/european-vehicle-market-statistics-2018-2019/>, (20 November 2021).

[8] International Energy Agency, Global EV Outlook, 2019, available at <https://www.iea.org/reports/global-ev-outlook-2019>, (2021).

[9] B. Stevens and P.-A. Schieb, OECD Workshop on: Developing Infrastructure for Alternative Transport Fuels and Power-trains to 2020/2030/2050. A Synthesis Report, OECD International futures programme (2013).

[10] Z. Hua, Advanced Direct Injection Combustion Engine Technologies and Development: *Volume 1: Gasoline and Gas Engines*, Woodhead Publishing in mechanical engineering, 2009.

[11] Bosch, Gasoline injection systems, 2013, available at <https://www.bosch-presse.de/pressportal/de/en/gasoline-injection-systems-42304.html>, (10 December 2021).

[12] G. Pilla, G. Bruneaux, T. Collazo, C. Bramoullé, L. Hermant, V. Ricordeau, *Étude GSM E1.1: Mise au point de nouvelles techniques de mesures pour les moteurs essence*, IFPEN, 2013.

[13] R. Hadef, K.P. Geigle, W. Meier, M. Aigner, Soot characterization with laser-induced incandescence applied to a laminar premixed ethylene–air flame, International Journal of Thermal Sciences 49 (8) (2010) 1457–1467.

[14] Fredrik Ree Westlye, *Experimental study of liquid fuel spray combustion*, PhD thesis, DTU department of mechanical engineering, 2016.

[15] P. Desgroux, X. Mercier, K.A. Thomson, Study of the formation of soot and its precursors in flames using optical diagnostics, Proc. Combust. Inst. 34 (1) (2013) 1713–1738.

[16] H.A. Michelsen, C. Schulz, G.J. Smallwood, S. Will, Laser-induced incandescence: Particulate diagnostics for combustion, atmospheric, and industrial applications, Prog. Energy Combust. Sci. 51 (2015) 2–48.

[17] J.E. Ketterer and W.K. Cheng, On the Nature of Particulate Emissions from DISI Engines at Cold-Fast-Idle, SAE Int. J. Engines 7 (2) (2014) 986–994.

[18] T. Lind, *Application and Development of Optical Soot Diagnostic Techniques*, PhD thesis, Lund University, Faculty of Engineering, Department of energy sciences division of combustion Engines, 2018.

[19] L.C. Riis Johansen, *Spark ignition combustion of direct injected alternative fuels*, PhD thesis, Chalmers tekniska högskola, 2016.

[20] F. Rouessac, A. Rouessac, Analyse chimique - 6ème édition, Dunod, 2004.

[21] Irving P. Herman, Optical diagostics for thin film processing, Elsevier Science, 1996.

[22] C.B. A. KNOWLES, Practical Absorption Spectrometry: *Ultraviolet spectrometry group*, London New York Chapman and Hall, 1984.

[23] H. Yang, D. Greszik, I. Wlokas, T. Dreier, C. Schulz, Tunable diode laser absorption sensor for the simultaneous measurement of water film thickness, liquid- and vapor-phase temperature, Appl. Phys. B 104 (1) (2011) 21–27.

[24] R. Pan, C. Brocksieper, J.B. Jeffries, T. Dreier, C. Schulz, Diode laser-based standoff absorption measurement of water film thickness in retro-reflection, Appl. Phys. B 122 (9) (2016) 249.

[25] M. Lubnow, T. Dreier, C. Schulz, NIR sensor for aqueous urea solution film thickness and concentration measurement using a broadband light source, Appl. Opt. 58 (16) (2019) 4546–4552.

[26] F. Mirschinka, J. N. Geiler, S. Kaiser, M. Mansbart, E. Schünemann, Imaging of water droplet clusters on glass with simultaneous laser-induced fluorescence and near-infrared absorption, ICLASS, Edinburgh, UK, 2021.

[27] R. Pan, J.B. Jeffries, T. Dreier, C. Schulz, Measurements of liquid film thickness, concentration and temperature of aqueous NaCl solution by NIR absorption spectroscopy, Appl. Phys. B 120 (3) (2015) 397–406.

[28] M. Lubnow, J.B. Jeffries, T. Dreier, C. Schulz, Water film thickness imaging based on time-multiplexed near-infrared absorption, Opt. Express 26 (16) (2018) 20902–20912.

[29] K. Miyashita, T. Tsukamoto, Y. Fukuda, K. Kondo, T. Aizawa, High-speed UV and visible laser shadowgraphy of GDI in-cylinder pool fire, SAE Tech. Pap. 2016-01-2165 (2016).

[30] C. Schulz and V. Sick, Tracer-LIF diagnostics, Prog. Energy Combust. Sci. 31 (1) (2005) 75–121.

[31] Z. Hua, Laser Diagnostics and Optical Measurement Techniques in Internal Combustion Engines, SAE International, USA, 2012.

[32] J.N. Geiler, R. Grzeszik, S. Quaing, A. Manz, S.A. Kaiser, Development of laser-induced fluorescence to quantify in-cylinder fuel wall films, Int. J. Engine Res. 19 (1) (2017) 134–147.

[33] N. Jüngst and S. Kaiser, Imaging of fuel-film evaporation and combustion in a direct-injection model experiment, SAE Tech. Pap. 2019-01-0293 (2019).

[34] M. Alonso, P.J. Kay, P.J. Bowen, R. Gilchrist, S. Sapsford, Quantification of transient fuel films under elevated ambient pressure environments, Atomization Sprays 22 (1) (2012) 79–95.

[35] M. Alonso, P.J. Kay, P.J. Bowen, R. Gilchrist, S. Sapsford, A laser induced fluorescence technique for quantifying transient liquid fuel films utilizing total internal reflection, Exp. Fluids 48 (1) (2010) 133–142.

[36] F. Schulz, J. Schmidt, F. Beyrau, Development of a sensitive experimental set-up for LIF fuel wall film measurements in a pressure vessel, Exp. Fluids 56 (5) (2015) 133.

[37] J.N. Geiler, F. Mirschinka, S.A. Kaiser, Characterization of the fluorescence properties of selected organic compounds for measuring the thickness of evaporating liquid fuel films, Appl. Phys. B 127 (2021) 110.

[38] J.B. Ghandi and P.G. Felton, On the fluorescent behavior of ketones at high temperatures, Exp. Fluids 21 (1996) 143–144.

[39] D. Maligne and G. Bruneaux, Time-resolved fuel film thickness measurement for direct injection SI engines using refractive index matching, SAE Tech. Pap. 2011-01-1215 (2011).

[40] B. Yang and J. Ghandhi, Measurement of diesel spray impingement and fuel film characteristics using refractive index matching method, SAE Tech. Pap. 2007-01-0485 (2007).

[41] C.-P. Ding, M. Sjöberg, D. Vuilleumier, D.L. Reuss, X. He, B. Böhm, Fuel film thickness measurements using refractive index matching in a stratified-charge SI engine operated on E30 and alkylate fuels, Exp. Fluids 59 (3) (2018) 59.

[42] Z. Le, Z. Zhihao, Z. Xiucheng, A. Nitisha, N. Jeffrey, L. Seong-Young, High pressure impinging spray film formation characteristics, SAE Tech. Pap. 2018-01-0312 (2018).

[43] S. Henkel, F. Beyrau, Y. Hardalupas, Taylor, A M K P, Novel method for the measurement of liquid film thickness during fuel spray impingement on surfaces, Opt. Express 24 (3) (2016) 2542–2561.

[44] M. Bardi, G. Bruneaux, A. Nicolle, O. Colin, Experimental methodology for the understanding of soot-fuel relationship in diesel combustion: fuel characterization and surrogate validation, SAE Tech. Pap. 2017-01-0721 (2017).

[45] K. Nakakita, M. Nagaoka, T. Fujikawa, K. Ohsawa, Photographic and three-dimensional numerical studies of diesel soot formation process, SAE Int. J. Engines 902081 (1990).

[46] F.R. Westlye, K. Penney, A. Ivarsson, L.M. Pickett, J. Manin, S.A. Skeen, Diffuse back-illumination setup for high temporally resolved extinction imaging, Appl. Opt. 56 (17) (2017) 5028–5038.

[47] L. de Francqueville, G. Bruneaux, B. Thirouard, Soot volume fraction measurements in a gasoline direct injection engine by combined laser induced incandescence and laser extinction method, SAE Int. J. Engines 3 (1) (2010) 163–182.

[48] N. Jüngst and S.A. Kaiser, Visualization of soot formation from evaporating fuel films by laser-induced fluorescence and incandescence, Proc. Combust. Inst. 38 (1) (2021) 1089–1097.

[49] N. Jüngst, *Optical diagnostics for soot formation from evaporating fuel films in combustion*, PhD thesis, Universität Duisburg-Essen, Duisburg, 2021.

[50] K.P. Geigle, R. Hadef, W. Meier, *Soot Formation and Flame Characterization of an Aero-Engine Model Combustor Burning Ethylene at Elevated Pressure*, ASME Turbo Expo 2013: Turbine Technical Conference and Exposition, San Antonio, Texas, USA, 03/06/2013 - 07/06/2013, American Society of Mechanical Engineers, 06032013.

[51] R.L. Vander Wal, Laser-induced incandescence: detection issues, Applied optics 35 (33) (1996) 6548–6559.

[52] S.A. Skeen and K. Yasutomi, Measuring the soot onset temperature in high-pressure n-dodecane spray pyrolysis, Combust. Flame 188 (2018) 483–487.

[53] E.A. Boardman, L.S.-W. Huang, J.J. Robson-Hemmings, T.M. Smeeton, S.E. Hooper, J. Heffernan, Deep ultraviolet (UVC) laser for sterilisation and fluorescence applications, Sharp Laboratories of Europe, Ltd., 2012, available at <http://www.sharp.co.jp/corporate/rd/n36/pdf/104_08.pdf>, (2021).

[54] M. Shur and R. Gaska, Deep-Ultraviolet Light-Emitting Diodes, Electron Devices, IEEE Transactions 57 (1) (2010) 12–25.

[55] R. Payri, F.J. Salvador, P. Martí-Aldaraví, D. Vaquerizo, ECN Spray G external spray visualization and spray collapse description through penetration and morphology analysis, Appl. Therm. Eng. 112 (2017) 304–316.

[56] M.M. Khan, J. Hélie, M. Gorokhovski, N.A. Sheikh, Experimental and numerical study of flash boiling in gasoline direct injection sprays, Appl. Therm. Eng. 123 (2017) 377–389.

[57] F. Schulz and F. Beyrau, The influence of flash-boiling on spray-targeting and fuel film formation, Fuel 208 (2017) 587–594.

[58] E. Sher, T. Bar-Kohany, A. Rashkovan, Flash-boiling atomization, Prog. Energy Combust. Sci. 34 (4) (2008) 417–439.

[59] R.O. Grover, T.D. Fansler, A. Lippert, M.C. Drake, D.N. Assanis, A numerical–experimental assessment of wall impingement models for spark-ignition direct-injection engines, Int. J. Engine Res. 21 (2) (2020) 281–301.

[60] X. Li, H. Pan, X. Dong, D. Hung, M. Xu, Spray impingement wall film breakup by wave entrainment, Proc. Combust. Inst. 37 (3) (2019) 3287–3294.

[61] C. Habchi, A Comprehensive Model for Liquid Film Boiling in Internal Combustion Engines, Oil Gas Sci. Technol. – Rev. IFP 65 (2) (2010) 331–343.

[62] G.L. Pilla and L. de Francqueville, Investigation of particle formation mechanisms in GDI engines during transient heating operation, société des ingénieurs automobiles (SIA) R-2013-06-08 (2013).

[63] M. Bardi, G. Pilla, X. Gautrot, Experimental assessment of the sources of regulated and unregulated nanoparticles in gasoline direct-injection engines, Int. J. Engine Res. 20 (1) (2018) 128–140.

[64] A. Roque, F. Foucher, W. Imoehl, J. Helie, Generation and Oxidation of Soot due to Fuel Films Utilizing High Speed Visualization Techniques, SAE Tech. Pap. 2019-01-0251 (2019).

[65] J. Manin, M. Bardi, L.M. Pickett, R. Payri, Boundary condition and fuel composition effects on injection processes of high-pressure sprays at the microscopic level, Int. J. Multiphase Flow 83 (2016) 267–278.

[66] J. Manin, L.M. Pickett, S.A. Skeen, Two-color diffused back-illumination imaging as diagnostic for time-resolved soot measurements in reacting sprays, SAE Int. J. Engines 6 (4) (2013) 1908–1921.

[67] S.A. Skeen, J. Manin, L.M. Pickett, E. Cenker, G. Bruneaux, K. Kondo, T. Aizawa, F. Westlye, K. Dalen, A. Ivarsson, T. Xuan, J.M. Garcia-Oliver, Y.

Pei, S. Som, W. Hu, R.D. Reitz, T. Lucchini, G. D'Errico, D. Farrace, S.S. Pandurangi, Y.M. Wright, M.A. Chishty, M. Bolla, E. Hawkes, A progress review on soot experiments and modeling in the engine combustion network (ECN), SAE Int. J. Engines 9 (2) (2016) 883–898.

[68] J.B. Ghandhi and D.M. Heim, An optimized optical system for backlit imaging, Rev. Sci. Instrum. 80 (5) (2009) 56105.

[69] T. Lind, G. Roberts, W. Eagle, C. Rousselle, Ö. Andersson, M.P.B. Musculus, Mechanisms of Post-Injection Soot-Reduction Revealed by Visible and Diffused Back-Illumination Soot Extinction Imaging, SAE Tech. Pap. 2018-01-0232 (2018).

[70] K.O.P. Bjørgen, D.R. Emberson, T. Lovas, Diffuse Back-Illuminated Extinction Imaging of Soot: Effects of Beam Steering and Flame Luminosity, SAE Tech. Pap. 2019-01-0011 (2019).

[71] K. Shway, M. Bardi, G. Bruneaux, S. Kaiser, Quantitative UV-absorption imaging of liquid fuel films and their evaporation, ICLASS, Edinburgh, UK, 2021.

[72] K. Shway, N. Jüngst, M. Bardi, G. Bruneaux, S.A. Kaiser, A multispectral UV–vis absorption technique for quantitative high-speed field-sequential imaging of fuel films and soot in combustion, Proceedings of the Combustion Institute 39 (1) (2023) 1475–1483.

[73] M. Bardi, R. Payri, L.M. Malbec, G. Bruneaux, L. M. Pickett, J. Manin, T. Bazyn, C. Genzale, Engine combustion network: comparison of spray development, vaporization, and combustion in different combustion vessels, Atomization Sprays 22 (10) (2012) 807–842.

[74] Sandia National Laboratories, Mesh and Geometry, National Technology and Engineering Solutions of Sandia, LLC, 2019, available at <https://ecn.sandia.gov/gasoline-spray-combustion/computational-method/mesh-and-geometry/>, (12 February 2020).

[75] I. Berlman, Handbook of fluorescence spectra of aromatic molecules, Academic press, New York and London, 1965, p. 113-114.

[76] M. Bardi, A. Di Lella, G. Bruneaux, A novel approach for quantitative measurements of preferential evaporation of fuel by means of two-tracer laser induced fluorescence, Fuel 239 (2019) 521–533.

[77] N. Jüngst, N. Frapolli, Y.M. Wright, K. Boulouchos, S.A. Kaiser, Experimental and numerical investigation of evaporating fuel films in combustion, Appl. Energy Combust. Sci. 7 (2021) 100033.

[78] National institue of standards and technology, NIST Chemistry WebBook, SRD 69, 2022, available at <https://webbook.nist.gov/chemistry/fluid/>, (4 September 2023).

[79] Mohamed Amine Chemak, *Large Eddy Simulation of Liquid-Fuel Film/Sooting-Flame Interaction in Wall Bounded Turbulent Flows*, PhD thesis, Normandie Université & IFP Energies Nouvelles, 2022.

[80] J.H. Seinfeld, S.N. Pandis, Atmospheric chemistry and physics, John Wiley and Sons, New Jersey, 2006, Chapter 15.1.1.

[81] S. Bejaoui, X. Mercier, P. Desgroux, E. Therssen, Laser induced fluorescence spectroscopy of aromatic species produced in atmospheric sooting flames using UV and visible excitation wavelengths, Combust. Flame 161 (10) (2014) 2479–2491.

7.2 Contributions of the author

7.2.1 Journal articles

[72] K. Shway, N. Jüngst, M. Bardi, G. Bruneaux, S.A. Kaiser, A multispectral UV–vis absorption technique for quantitative high-speed field-sequential imaging of fuel films and soot in combustion, Proceedings of the Combustion Institute 39 (1) (2023) 1475–1483.

7.2.2 Conference contributions

[71] K. Shway, M. Bardi, G. Bruneaux, S. Kaiser, Quantitative UV-absorption imaging of liquid fuel films and their evaporation, ICLASS, Edinburgh, UK, 2021.

7.2.3 Oral presentations

K. Shway, M. Bardi, G. Bruneaux, S.A. Kaiser, Development Of Quantitative Experimental Diagnostics For The Characterization Of Pool Fires At Engine Like Conditions, GDR suie, France, online event (December 7th, 2020).

K. Shway, M. Bardi, G. Bruneaux, S. Kaiser, Quantitative UV-absorption imaging of liquid fuel films and their evaporation, ICLASS, Edinburgh, UK, online event (August 30th – September 2nd, 2021).

K. Shway, M. Bardi, G. Bruneaux, S. Kaiser, A time-multiplexed multispectral UV-vis extinction technique for quantitative high-speed imaging of fuel films and soot in combustion, IEA TCP “Clean Combustion” workshop for the Task Leaders’ Meeting, online event (July 9th, 2021).

K. Shway, M. Bardi, G. Bruneaux, S.A. Kaiser, Development of Quantitative Experimental Diagnostics for the Characterization of Pool Fires at Engine-Like Conditions, ECN 7.7 web meeting (June 3rd, 2021).

K. Shway, N. Jüngst, M. Bardi, G. Bruneaux, S.A. Kaiser, A multispectral UV–vis absorption technique for quantitative high-speed field-sequential imaging of fuel films and soot in combustion, 39th International Symposium on Combustion, Vancouver, Canada (July 24th - 29th, 2022).

7.2.4 Posters

K. Shway, N. Jüngst, M. Bardi, G. Bruneaux, S.A. Kaiser, A time-multiplexed multispectral UV-vis extinction technique for quantitative high-speed imaging of fuel films and soot in combustion, Gordon Research Conferences (GRC) connects, online event (July 13th, 2021).

8 Appendix

8.1 Constant-flow facility experiments

8.1.1 Intensity variation in raw images

During image analysis, a variation in the background intensity of the LED-on images was detected that was not related to the injection/impingement process, as it was outside the process region of interest. This low-frequency variation was related to a variation in the sensitivity of the high-speed intensifier during image acquisition and must be taken into account for a correct quantification of the liquid film thickness. In this section, the intensity variation of the raw images with respect to time is assessed. A correction coefficient k_λ^t at time t and wavelength λ was calculated to correct for the intensity variation in the raw images. The corrected intensity absorbance images were then calculated according to **Equation (4.6)**.

One region of interest (ROI) was selected at the contour of the raw image outside the liquid fuel-film region (total of 29,920 pixels) to study the variation of raw image intensity in the cases with and without injection. Note that fuel spray, vapor, and soot may be present in the selected region, which may affect the intensity signal (decrease or increase in intensity). **Figure 8.1** shows the selected ROI at the contour of a ratio image under non-reacting conditions with FS1 at t = 10.6 ms aSOI (rep. 2) and λ = *265 nm*.

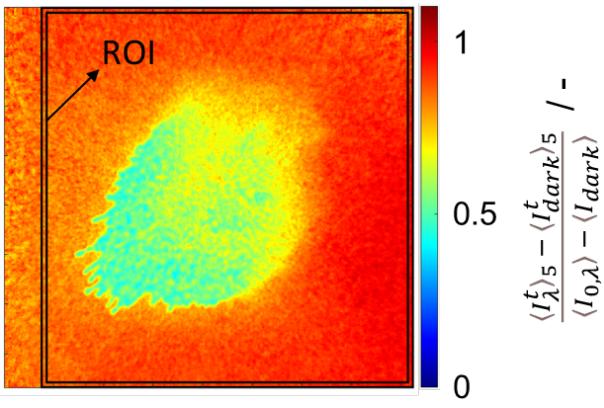

Figure 8.1. Ratio image at t = 10.6 ms aSOI (rep. 2) and λ = 265 nm under reacting conditions using FS1.

At the beginning of each set of experiments (one experimental condition), one repetition without injection was acquired. The average of the ratio values in the ROI at time t and wavelength λ for the case without injection $(R_\lambda^{t,mean})_{WO\ inj.}$

was calculated first. A fifth-degree polynomial fitting for $(R_\lambda^{t,mean})_{WO\ inj.}$ was calculated to reduce the shot-to-shot variations. **Figure 8.2** shows the variation of $(R_\lambda^{t,mean})_{WO\ inj.}$ with respect to time for all wavelengths λ. The results shown in **Figure 8.2** corresponds to a camera configuration with an intensifier gain equal to 47, before the start of acquisition for the cases under firing conditions with FS1. The variation of $(R_\lambda^{t,mean})_{WO\ inj.}$, is attributed to the sensitivity of the detection system, was different from one wavelength to another. This effect needs to be corrected in the raw UV-vis absorption images of the cases with injection.

If the signal intensity in the raw images with injection varied similarly from one repetition to another, the variation of signal intensity in the raw UV-vis absorption images with injection could be simply corrected by $(R_\lambda^{t,mean})_{WO\ inj.}$. In this case, k_λ^t is simply equal to $(R_\lambda^{t,mean})_{WO\ inj.}$. However, as we will see later, the signal intensity in UV-vis absorption images varied differently from one repetition to another, even under the same experimental conditions. Based on this fact, another approximation was needed to accurately correct for the signal intensity variation in each repetition. Therefore, the average of the ratio values variation in the ROI over time $R_\lambda^{t,mean}$ was calculated.

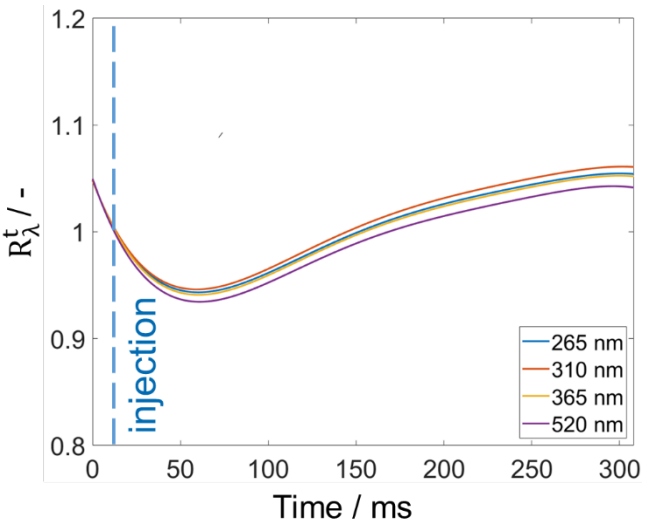

Figure 8.2. Evolution in time of $(R_\lambda^{t,mean})_{WO\ inj.}$, corresponding to a camera configuration with an intensifier gain equal to 47, before the start of acquisition for the cases under firing conditions with FS1.

Figure 8.3 top row shows the evolution in time of $R_\lambda^{t,mean}$ at λ = 265 nm (first column) and 365 nm (second column) under reacting conditions with FS1 for all 16 injection repetitions. $R_\lambda^{t,mean}$ values showed important variations in intensity

due to the presence of vapor and soot. In these repetitions, even after the soot disappeared (after t = 150 ms aSOI), $R_\lambda^{t,mean}$ varied differently from one repetition to another. This may be related to the shot-to-shot variations. Therefore, the correction coefficient k_λ^t, at one experimental condition cannot be corrected with $(R_\lambda^{t,mean})_{WO\ inj.}$ from the case without injection, but with another approximation that takes into account the signal intensity variations in each repetition.

The presence of fuel vapor (at λ = 265 nm) and soot (at all wavelengths) affected the ratio values. For this reason, the 97th percentile of the ratio values in the ROI at time t and wavelength λ ($R_\lambda^{t,97th\ percentile}$) was calculated to reduce the outliers, values related to the contributions of vapor and soot, obtained in $R_\lambda^{t,mean}$.

Figure 8.3 bottom row shows the evolution in time of $R_\lambda^{t,97th\ percentile}$ at the same experimental conditions. The traces at 310, 365 and 520 nm showed a similar trend, therefore, only the traces at 365 nm were presented in **Figure 8.3**. At 310, 365 and 520 nm, only soot contribution made the ratio values fluctuating. These fluctuations were more important at 265 nm. However, the traces at 265 nm were affected by both soot (under reacting conditions) and vapor (under both reacting and non-reacting conditions) contributions. At all wavelengths, fuel injection made a large decrease in the ratio value traces.

The 97th percentile approximation reduced effectively the fluctuations found in $R_\lambda^{t,mean}$. The calculation of a fifth-degree polynomial fitting for $R_\lambda^{t,97th\ percentile}$ reduced the shot-to-shot variations and omitted the decrease in signal intensity caused by the fuel injection.

The ratio intensity variations obtained from the cases without injection $(R_\lambda^{t,mean})_{WO\ inj.}$ and $(R_\lambda^{t,97th\ percentile})_{WO\ inj.}$, representing only the intensity variations from the sensitivity of the detection system, and fitted $R_\lambda^{t,97th\ percentile}$, representing the intensity variations without outliers (related to vapor and soot contributions), were used to calculate k_λ^t (under reacting and non-reacting conditions) via **Equation (8.1)**:

$$k_\lambda^t = \frac{R_\lambda^{t,97th\ percentile}}{(R_\lambda^{t,97th\ percentile})_{WO\ inj.}} \times (R_\lambda^{t,mean})_{WO\ inj.} \tag{8.1}$$

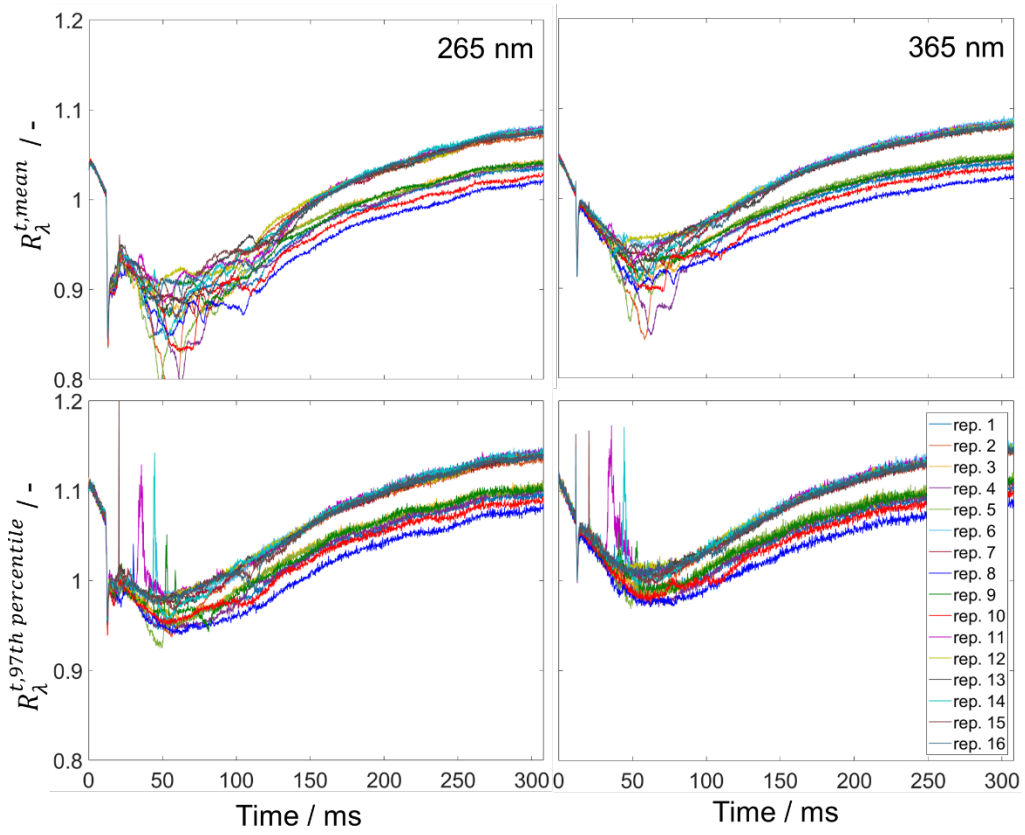

Figure 8.3. Evolution in time of $R_\lambda^{t,\,mean}$ (top row), and $R_\lambda^{t,\,97th\ percentile}$ (bottom row) at 265 nm (first column) and 365 nm (second column) under reacting conditions with FS1 for all 16 injection repetitions.

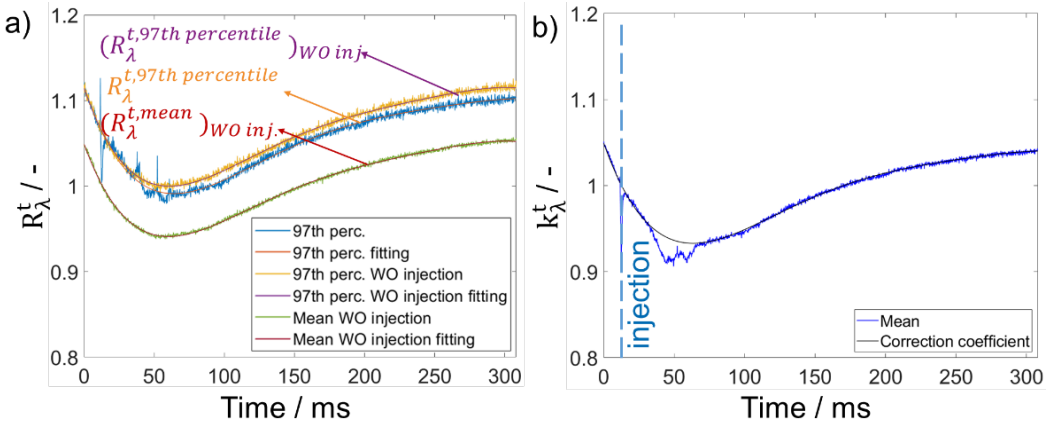

Figure 8.4. Evolution in time of (a) $R_\lambda^{t,\,97th\ percentile}$, $(R_\lambda^{t,\,mean})_{WO\ inj.}$ and $(R_\lambda^{t,\,97th\ percentile})_{WO\ inj.}$ and their corresponding fifth-degree polynomial fitting and (b) k_t the correction coefficient at 365 nm for repetition 1 under reacting conditions with FS1.

Figure 8.4a shows the evolution in time of $R_\lambda^{t,\,97th\ percentile}$, $(R_\lambda^{t,\,mean})_{WO\ inj.}$ and $(R_\lambda^{t,\,97th\ percentile})_{WO\ inj.}$ and their corresponding fifth-degree polynomial fit at λ = 365 nm for repetition 1 (rep. 1) under reacting conditions with FS1. **Figure 8.4**b shows the evolution in time of $R_\lambda^{t,\,mean,rep.1}$ and $k_{\lambda,rep.1}^t$. **Figure 8.5** shows the evolution in time of the correction coefficient k_λ^t at 365 nm for all repetitions under reacting conditions with FS1.

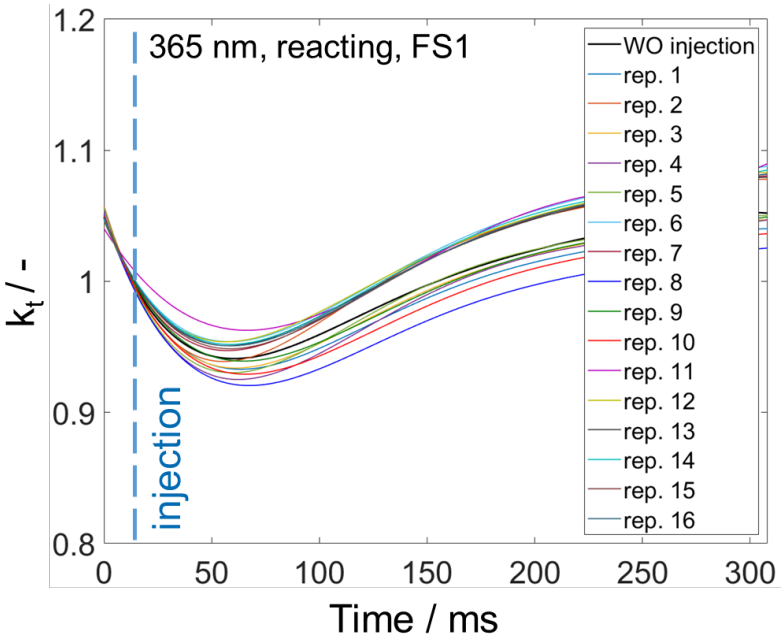

Figure 8.5. Evolution in time of the correction coefficient k_λ^t at λ = 365 nm for all repetitions under reacting conditions with FS1.

8.1.2 Fuel-film detection

The morphological post-processing algorithm adopted for the constant-flow facility experiments for liquid fuel-film detection is similar to that applied in the constant-volume cell experiments. **Figure 8.6** shows the schematic of the morphological image processing algorithm with example images from a single repetition with FS1 under reacting conditions at t = 3.5, 10.6 and 46 ms aSOI and λ = 265 nm.

For the constant-flow facility experiments, the algorithm was applied to the images under both non-reacting and reacting conditions. The algorithm segments the image into three levels: a background that represents the image noise, a mid-ground that represents the vapor (under non-reacting and reacting conditions) and soot (under reacting conditions) surrounding the fuel-film, and a foreground that represents the liquid fuel-film.

Spatial mask: Spatial masks were calculated similarly to the constant-volume cell experiments, as described in **section 5.1.2**. Here, the reference image I_{ref} corresponds to $\langle I_{0,\lambda}\rangle - \langle I_{\mathrm{dark}}\rangle$ at wavelength λ. The fuel-films are detected at $\lambda = 265$ nm. The shot noise was estimated similarly to **section 5.1.2**, from the ratio between I_1, a single image before injection represented by $(\langle I^t_{265\,nm}\rangle_5 - \langle I^t_{\mathrm{dark}}\rangle_5)_{bSOI}$ and $I_{ref.}$ Since the signal intensity was corrected by a correction coefficient k_t at time t, the ratio I_1/I_{ref} was corrected and represented by $\frac{(\langle I^t_{265\,nm}\rangle_5 - \langle I^t_{dark}\rangle_5)_{bSOI}}{\langle I_{0,\,265\,nm}\rangle - \langle I_{dark}\rangle} \times \frac{1}{k_t}$. A threshold of $\overline{I_1/I_{ref}} - k\cdot\mathrm{std}(I_1/I_{ref})$, representing the shot noise absorbance level (background) in the images, was calculated. The threshold separates the background from the mid-ground and foreground. In the constant-flow facility experiments, k was equal to 25. The result is a time series of binary masks *SM*.

First and second spatio-temporal masks (*STM1* and *STM2*, respectively): These were calculated in the same way as in **section 5.1.2.** For the calculation of STM1, the only difference is in t_d, the approximate time when fuel film is completely deposited on the plate. In the constant-flow facility experiments, t_d was equal to 3.5 ms aSOI. For the calculation of *STM2*, the difference is in the reference mask $\mathrm{STM1}_{ref}$ and the reference time t_{ref} corresponding to $\mathrm{STM1}_{ref}$. $\mathrm{STM1}_{ref}$ was obtained from the spatial mask equation, but here k was equal to 120 to obtain a well-defined fuel-film structure with less contribution from the fuel-vapor surrounding the fuel-film.

The intensity-corrected ratio images $\frac{(\langle I^t_{265\,nm}\rangle_5 - \langle I^t_{dark}\rangle_5)_{bSOI}}{\langle I_{0,\,265\,nm}\rangle - \langle I_{dark}\rangle} \times \frac{1}{k_t}$ are then multiplied by the corresponding mask STM2 and converted to absorbance, and then film thickness images.

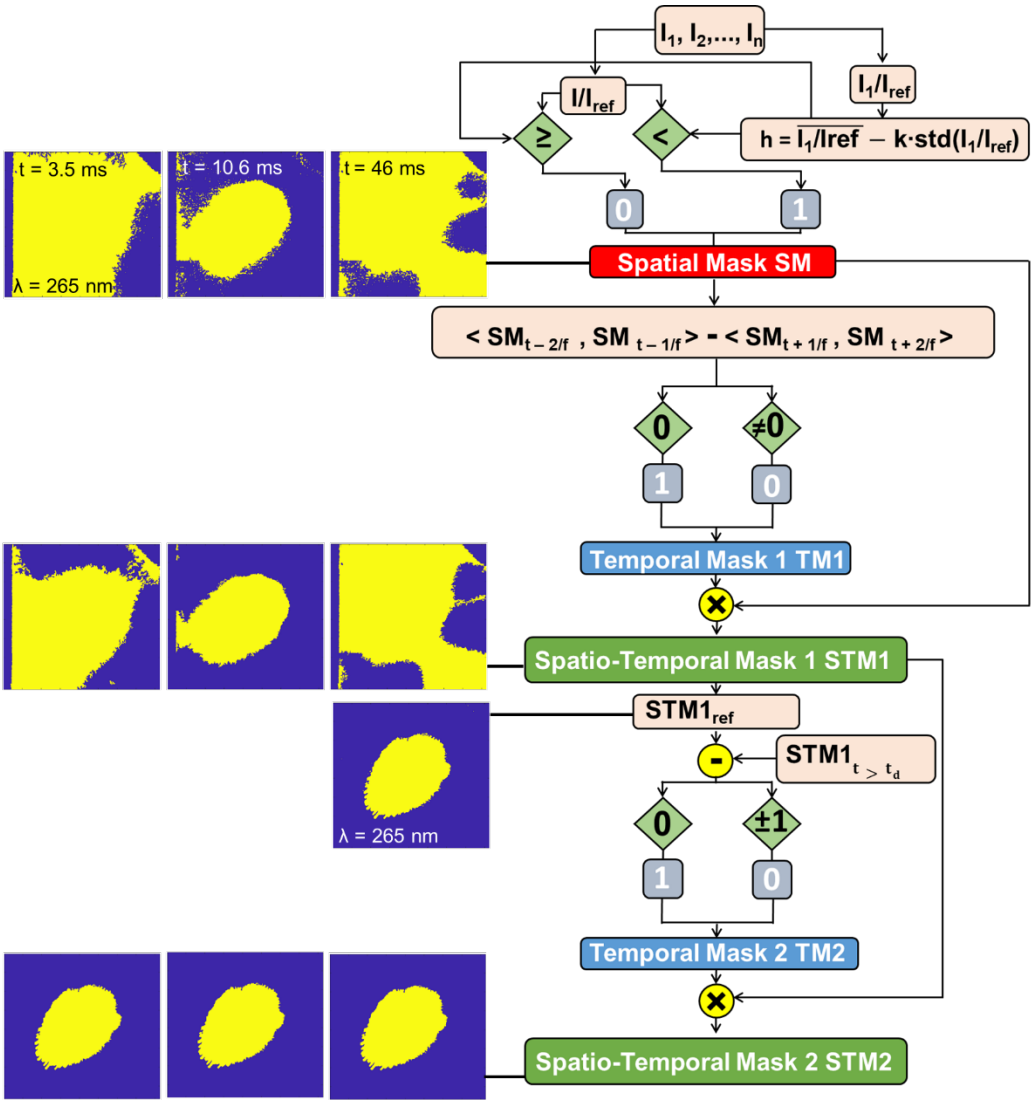

Figure 8.6. Flowchart of the morphological image processing for separating background, vapor and soot, and liquid films. Images in the flowchart correspond to one repetition (rep. 1) with FS1 under reacting conditions at t = 3.5, 10.6 and 46 ms aSOI and λ = 265 nm.

8.2 Synthèse du manuscrit de thèse en français

8.2.1 Introduction

La combustion est, jusqu'à présent, le principal processus de conversion énergétique, dans lequel le carburant réagit avec un oxydant (généralement l'oxygène de l'air) pour libérer de l'énergie et des produits de combustion. Dans le domaine de l'automobile, le moteur à combustion interne (diesel ou essence) est actuellement le principal système de conversion énergétique de la plupart des véhicules, en raison de son efficacité, de sa polyvalence et de ses faibles coûts d'exploitation. Malgré l'efficacité supérieure des moteurs diesel, les réglementations strictes sur les émissions d'oxyde d'azote (NO_x) et de nanoparticules ont incité les constructeurs automobiles à utiliser de plus en plus de moteurs à essence, en particulier ceux à injection indirecte d'essence (PFI) ou à injection directe d'essence (GDI).

L'introduction des systèmes d'injection directe d'essence (GDI) dans les moteurs à essence a amélioré leur efficacité, offrant une puissance et des performances bien supérieures à celles des autres systèmes d'injection d'essence, tout en réduisant les émissions de CO_2. Toutefois, en raison du temps d'atomisation réduit du carburant dans les moteurs GDI, le carburant injecté directement dans la chambre de combustion peut entraîner une augmentation des émissions de nanoparticules de carbone si le jet (spray) impacte le piston ou le cylindre et forme des films de carburant liquide. Ces films liquides s'évaporent lentement et, après l'allumage, peuvent interagir avec la flamme du prémélange pour produire des suies. Les risques associés aux suies, composée de nanoparticules de carbone, constituent une source majeure de pollution atmosphérique, nuisant à l'écosystème et à la santé humaine, et causant des milliers de décès dans le monde.

À la fin des années 1990, l'Union européenne a pris l'initiative d'introduire des réglementations sur les émissions automobiles afin de limiter les polluants tels que le monoxyde de carbone (CO), les hydrocarbures imbrûlés (HC), les NO_x, les nanoparticules produits par les moteurs à combustion interne des voitures. Les moteurs GDI doivent ainsi continuer à améliorer leur efficacité et leurs performances pour répondre aux nouvelles réglementations en matière d'émissions, ce qui nécessite une meilleure compréhension de tous les mécanismes impliqués dans la formation des suies dans les moteurs GDI [1,2].

Malgré des progrès significatifs en matière d'électrification des véhicules, les véhicules à moteur à combustion interne dominent toujours le marché. De nombreux pays dans le monde mettent en œuvre de nouvelles politiques visant à

adopter une production automobile plus propre afin de réduire les émissions locales dans les villes et de lutter contre le changement climatique. Cependant, bien que la tendance du marché soit à l'électrification des véhicules, avec des investissements massifs des constructeurs automobiles dans ce domaine, le marché croissant des véhicules hybrides confirme la nécessité d'optimiser et d'améliorer les moteurs GDI pour répondre aux nouvelles réglementations en matière d'émissions, tout en améliorant l'efficacité du moteur et l'économie de carburant.

L'objectif de cette thèse est de comprendre expérimentalement, à l'aide de diagnostics optiques, les mécanismes à l'origine des émissions élevées de nanoparticules dans les moteurs GDI. Le but de ce travail est d'étudier la formation et l'évaporation des films de carburant liquide après l'injection directe d'essence, et l'interaction entre les films de carburant liquide déposés et la flamme de prémélange dans des environnements thermodynamiques contrôlés et des conditions similaires à celles d'un moteur. Deux paramètres expérimentaux ont été choisis pour cette étude : l'épaisseur du film de carburant et l'extinction des suies.

8.2.2 Synthèse de l'état de l'art

Parmi les techniques utilisées dans la littérature pour détecter et quantifier l'épaisseur du film liquide dans des cas similaires à ceux des moteurs à combustion interne : L'absorption, la fluorescence induite par laser (LIF), et la « refractive index matching » (RIM). Pour plus de détails sur chaque technique, voir la **section 2.3**. Dans nos expériences, nous avons utilisé la technique d'absorption pour mesurer l'épaisseur du film liquide à partir de l'absorption UV du toluène. Par rapport à la LIF, la technique d'absorption présente l'avantage que la photophysique sous-jacente de l'absorption est beaucoup plus simple que celle de la fluorescence. L'absorption UV n'est pas affectée par la pression ou l'extinction par l'oxygène. Elle pourrait dépendre de la température, mais dans le cas du toluène, nos mesures ont montré que ce phénomène n'était pas significatif dans la gamme de température concernée. Cependant, dans la LIF, l'extinction de la fluorescence par l'oxygène peut contribuer à supprimer le signal provenant de la vapeur de carburant, considéré comme l'une des principales interférences dans la technique d'absorption. Dans notre étude, nous utilisons des diodes électroluminescentes (LED) peu coûteuses qui peuvent être pulsées à des fréquences très élevés, alors que toutes les imageries de films de carburant LIF documentées sont basées sur l'illumination laser.

La LIF et l'absorption UV nécessitent tous deux un carburant contenant des aromatiques, mais à des concentrations différentes - beaucoup plus faibles pour

la LIF. La forte teneur en aromatiques du substitut de carburant utilisé dans la technique d'absorption est plus représentative de la composition de l'essence. Toutefois, l'évaporation préférentielle est plus importante dans la technique d'absorption que dans la technique LIF. Pour toute composition de substitut de carburant, l'erreur d'évaporation préférentielle sur les mesures d'absorption devrait être étudiée. En ce qui concerne la RIM, elle n'est pas affectée par les conditions ambiantes et peut être réalisée avec presque tous les carburants, mais elle dépend fortement de la rugosité de la surface du substrat. La présence de résidus liquides ou de dépôts de suies sur la surface peut affecter la précision de la technique. Cette technique ne nécessite pas l'ajout d'un traceur et peut être utilisée avec des carburants commerciaux.

Dans ces trois techniques, la diffusion de lumière, l'incandescence par les suies et l'extinction par les suies et les précurseurs des suies peuvent potentiellement interférer avec la mesure de l'épaisseur du film liquide. Dans le cadre de nos travaux à l'UDE, une technique d'absorption UV-vis a été mise au point pour distinguer et corriger ces contributions. Dans sa mise en œuvre actuelle, la technique d'absorption nécessite un accès optique à partir de deux côtés opposés du film, mais une configuration pour l'imagerie par réflexion est également possible [3].

Pour mesure les suies, plusieurs diagnostics optiques typiques ont été utilisés dans la littérature, tels que : la technique d'extinction de la lumière (light extinction technique), la technique du rétroéclairage diffus (DBI) et la technique de l'incandescence induite par laser (LII). Pour plus de détails sur chacune de ces techniques, voir la **section 2.4**. En tant que technique non intrusive, la DBI est plus avantageuse que la LII. Le déplacement du faisceau lumineux rencontré dans la technique d'extinction a été atténué par l'utilisation d'une lumière diffuse dans la DBI. Dans notre étude, la technique DBI a été choisie pour mesurer les suies.

8.2.3 Méthodologies

- **Expériences en cellule à volume constant**

Les expériences ont été réalisées dans une cellule à volume constant à l'IFPEN [4,5]. La configuration de la formation du film liquide et de son interaction avec la flamme de prémélange comprend de quatre étapes :

1. Remplissage avec des gaz de prémélange (N_2 dans le cas non-réactif et C_2H_2, H_2, O_2 et N_2 dans le cas réactif)
2. Injection de carburant (70% d'iso-octane - 30% de toluène)

3. Combustion (allumage et propagation de la flamme de prémélange à l'intérieur de la cellule)
4. Interaction film liquide / flamme.

Dans des conditions non-réactives, une variation paramétrique de la température de la cellule (50, 100, 150 et 200°C) et de la pression (0.5, 1 et 6 bar) a été effectuée. En conditions réactives, la température de la cellule était de 100°C et la pression de 1 bar, deux excès d'oxygène résiduels ont été utilisés $\zeta = 2$ et 15%.

La technique d'absorption UV a été utilisée pour mesurer l'épaisseur du film de carburant liquide à partir de l'absorption du toluène à des longueurs d'onde inférieures à 270 nm environ. La technique DBI a été utilisée pour la mesure de l'extinction des suies à 810 nm. Le trajet optique de l'absorption UV est orthogonal à celui de DBI. Les acquisitions d'images de l'absorption UV et de DBI ont été déclenchées simultanément. Le schéma de la cellule à volume constant et le trajet optique ainsi que les conditions expérimentales utilisées, sont présentés dans la **Figure 1**. Les deux techniques sont basées sur la loi de Beer-Lambert, et les images d'absorbance et d'extinction ont été calculées à partir du rapport entre une image acquise à l'instant t et une image de référence (acquise avant l'injection).

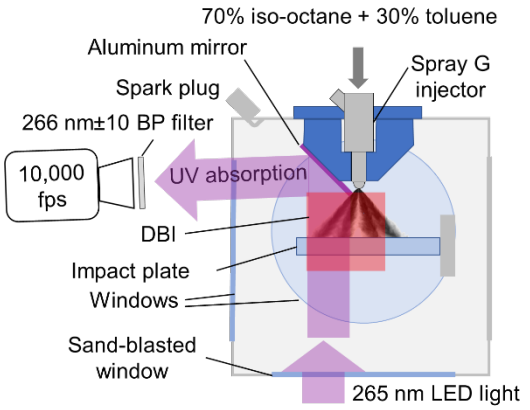

Injecteur	Spray G AV67 – 022 [6] injecteur à 8 orifices
Substitut de carburant	30% toluene + 70% iso-octane
p_{cell}	0.5, 1, 6 bar
T_{wall}	50, 100, 150, 200°C
$p_{injection}$	200 bar
T_{fuel}	90°C
$t_{injection}$	0.78 ms

Figure 1. (À gauche) Schéma de la cellule à volume constant et du trajet optique, et (à droite) l'ensemble des conditions expérimentales.

Les images d'absorbance obtenues ont montré des contributions de la vapeur, de l'extinction des suies et de la diffusion de la lumière interférant avec l'absorption du toluène liquide. Dans ce qui suit, une nouvelle technique d'absorption a été développée pour tenir compte de ces différentes contributions.

- **Expériences en installation à débit d'air constant**

Les expériences ont été réalisées dans une installation à débit d'air constant optiquement accessible à l'UDE [7]. Une condition expérimentale a été adoptée à p = 1 bar et T = 100°C dans des conditions non-réactives et réactives. Un second substitut de carburant a été utilisé, composé de 60 % d'iso-octane, 30 % de toluène et 10 % de n-octane.

À l'UDE, une technique de diagnostic multispectrale multiplexée dans le temps, basée sur la technique d'absorption UV et visible, a été mise au point pour mesurer l'épaisseur des films de carburant liquide en combustion, en présence de vapeur de carburant et des suies. Cette technique a été développée sur la base de la technique d'absorption UV à longueur d'onde unique utilisée à l'IFPEN. Dans la technique d'absorption UV à longueur d'onde unique (à 265 nm), la diffusion de la lumière, l'incandescence des suies et l'extinction des suies rendent difficile la quantification de l'épaisseur du carburant. Les images d'absorbance ont montré une contribution significative de l'extinction des suies après sa formation, ce qui rend le champ de vision optiquement dense. La technique d'absorption UV-vis permet de distinguer et de corriger les différentes contributions présentes dans les images d'absorbance, qui interfèrent avec les mesures quantitatives de l'épaisseur du film de carburant liquide. La technique développée est basée sur l'acquisition quasi-simultanée d'images d'absorbance à plusieurs longueurs d'onde (ici, 265, 310, 365 et 520 nm) en utilisant des LED peu coûteuses et d'une caméra à grande vitesse. Des longueurs d'onde supplémentaires (différentes de 265 nm) sont utilisées pour différencier la diffusion de la lumière et l'absorption dans le film de carburant ainsi que l'extinction de la lumière par les suies et les précurseurs des suies. La **Figure 2** montre le schéma optique utilisé et les conditions expérimentales utilisées.

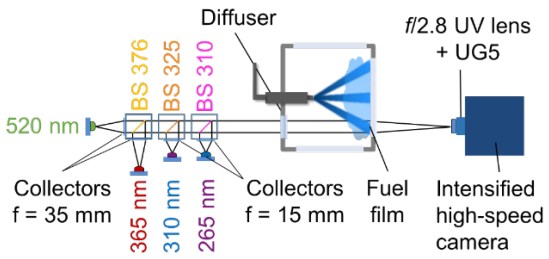

Injecteur	Injecteur Bosch à 6 orifices
Substitut de carburant	FS1 : 30% toluene + 70% iso-octane FS2 : 30% toluene + 60% iso-octane + 10% n-octane
p_{cell}	1 bar
T_{wall}	79 °C
T_{air}	103°C
$p_{injection}$	100 bar
V_{air}	1.8 m/s
$t_{injection}$	1 ms

Figure 2. (À gauche) Schéma optique autour de l'installation à débit d'air constant, et (à droite) l'ensemble des conditions expérimentales.

- **Étalonnage in-situ et incertitudes de l'absorption**

L'étalonnage in-situ a été réalisé en plaçant une cuvette de 10 mm d'épaisseur à l'intérieur du trajet optique dans la cellule à volume constant à 50°C. Le substitut de carburant (FS1), composé de 70 % d'iso-octane et de 30 % de toluène, a été dilué à 1:1000 dans un solvant non absorbant (iso-octane transparent aux UV). Cela correspond à une épaisseur de 10 μm de carburant pur. La même procédure a été réalisée à l'intérieur de l'installation à débit d'air constant dans des conditions ambiantes. Cette fois, l'étalonnage in-situ a été effectué pour les deux substituts de carburant FS1 (70 % d'isooctane - 30 % de toluène) et FS2 (60 % d'isooctane – 30 % de toluène - 10 % de n-octane). Dans les deux expériences et pour les deux substituts de carburant, l'absorbance à cette épaisseur était égale à 0,27. À partir de là, la constante de proportionnalité 1 / (c ε) entre d et A dans l'**équation (4.3)** a été calculée, comme étant de 37 μm. Les images d'absorbance ont été converties en images de l'épaisseur du film de carburant liquide à l'aide d'une relation de proportionnalité calculée à partir de l'équation d'étalonnage in-situ d = A 37 μm. Cette équation était similaire dans les deux campagnes expérimentales et avec les deux substituts de combustible (contenant 30 % de toluène en volume).

D'autres incertitudes liées à la technique d'absorption ont également été évaluées. Après l'injection directe et la formation du film de carburant liquide, le traceur (par exemple, le toluène) est supposé s'évaporer avec les autres composants du substitut de carburant, en maintenant sa concentration constante. En réalité, les composants du substitut de carburant s'évaporent préférentiellement en fonction de leurs caractéristiques d'évaporation. Par conséquent, la concentration du traceur peut varier au cours de l'évaporation. À épaisseur de film de carburant et coefficient d'extinction molaire constants, tout changement de concentration du traceur contribuera à une différence d'absorbance, entraînant une incertitude dans la mesure de l'épaisseur du film de carburant liquide. Nous avons étudié l'évaporation préférentielle numériquement (en utilisant un modèle numérique développé à l'IFPEN [8] pour l'évaporation d'un mélange multi-composant) et expérimentalement (évaporation lente des deux substituts de carburant sur une plaque chauffée). L'objectif de l'étude était de déterminer l'erreur d'incertitude associée à l'évaporation préférentielle sur l'absorbance. Un autre objectif était de trouver une composition de substitut de carburant (FS2) qui réduirait la variation de la concentration de toluène pendant l'évaporation, et donc l'effet de l'évaporation préférentielle sur les mesures de l'épaisseur du film de carburant liquide. L'incertitude associée à l'évaporation préférentielle a ainsi été diminué de

65% lors de l'utilisation du second substitut de carburant FS2 par rapport au premier substitut de carburant FS1, quand 98 % du carburant a été évaporé.

L'effet de la température sur l'absorption a également été étudié. Une incertitude de 7 % a été trouvée après avoir augmenté de la température ambiante de 40°C, montrant un faible effet de la température sur la technique d'absorption. L'effet de la pression n'a pas été étudié, mais a été considéré comme négligeable.

8.2.4 Résultats

Un algorithme de post-traitement morphologique a été développé pour détecter les films de carburant liquide et pour corriger la contribution de la vapeur de carburant dans les images d'absorbance. Les paramètres globaux d'épaisseur et de masse ont été obtenus à la fin de notre post-traitement.

Dans la cellule à volume constant (à l'IFPEN), les épaisseurs de film liquide ont été déterminées dans des conditions non réactives et réactives. Une variation paramétrique de la température de la cellule et de la pression a été faite dans des conditions non-réactives. La **Figure 3** montre une série d'images de l'épaisseur du film de carburant liquide corrigées de la vapeur pour une seule répétition à plusieurs conditions expérimentales de température et de pression. À des températures élevées, l'évaporation du film liquide était très rapide, en raison de l'amincissement de l'épaisseur du film de carburant déposé sur la plaque. À des pressions de cellule élevées, supérieures à la pression de saturation, une meilleure atomisation du carburant injecté a été obtenue avec des épaisseurs de film liquide minces, mais avec une évaporation lente. À une pression inférieure à la pression atmosphérique (0.5 bar), proche de la pression de saturation, de faibles épaisseurs de film liquide ont été obtenues avec une évaporation rapide.

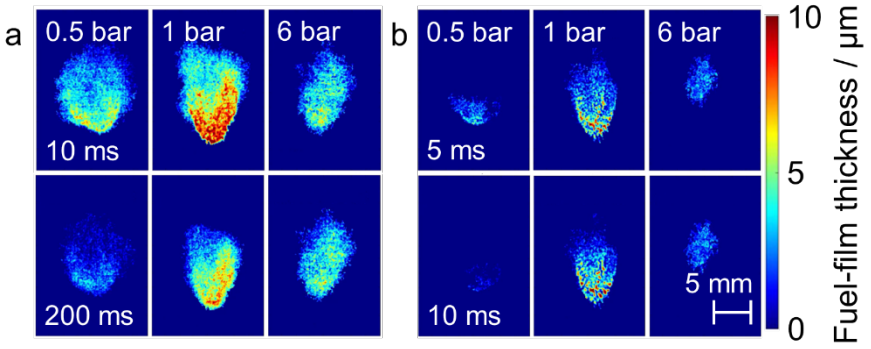

Figure 3. Images sélectionnées de l'épaisseur du film de carburant liquide corrigé de la vapeur pour une seule répétition dans trois conditions expérimentales à p = 0,5, 1 et 6 bar (colonnes de gauche à droite) et deux températures de cellule (a) T = 50°C à 10 (ligne du haut) et 200 ms (ligne du bas) aSOI, et (b) 100°C à 5 (ligne du haut) et 10 ms (ligne du bas) aSOI.

Après l'injection directe, des films de carburant liquide commencent à se former sur la paroi et à s'évaporer. Après l'allumage, la flamme de prémélange se propage dans la cellule vers la plaque, où le film liquide continue de s'évaporer. Le front de flamme atteint la paroi et commence à s'éteindre, mais rencontre des zones de vapeur localement riches au-dessus des films de carburant liquide. L'interaction entre la flamme de prémélange et les films de combustible qui s'évaporent se transforme en une flamme de type diffusion alimentée par l'excès d'oxygène résiduel dans les gaz brûlés de la flamme de prémélange, ce qui entraîne la formation des suies. Les images DBI ont montré que le pourcentage d'excès d'oxygène résiduel affectait le temps d'arrivée de la flamme et la distribution spatiale des suies. Dans le cas d'un excès d'oxygène résiduel élevé ($\zeta = 15\%$), la flamme de prémélange est arrivée plus tôt et a formé des suies plus près de la plaque avec une extinction des suies plus élevée que dans le cas d'un faible excès d'oxygène résiduel ($\zeta = 2\%$).

Dans l'installation à débit d'air constant (à l'UDE), la technique multispectrale mise au point a permis de quantifier les différentes incertitudes qui ne sont pas liées à l'absorbance du film de carburant liquide. La soustraction d'une image sombre (toutes les LED éteintes) dans chaque cycle d'images a permis de corriger l'incandescence naturelle des suies dans toutes les images (un cycle d'images est composé d'une série de 5 images : sombre, à 265 nm, à 310 nm, à 365 nm et à 520 nm). Pour corriger la diffusion de la lumière au niveau du film liquide, des images d'absorbance à 310 nm ont été utilisées. Il s'agit d'une région spectrale proche de 265 nm, mais où l'absorption par le toluène est très faible. La correction de la diffusion de la lumière au niveau du film s'est avérée d'une importance mineure pour la quantification de l'épaisseur (< 3 % de la masse totale du film). Des LED à 310, 365 et 520 nm ont été utilisées pour déterminer l'absorbance des suies et des précurseurs des suies en fonction de la longueur d'onde. Le résultat a été utilisé pour déduire l'absorbance à 265 nm de celle à 310 nm et la soustraire. Cette correction améliore considérablement la quantification de l'épaisseur du film en présence des suies (jusqu'à 30 % de la masse totale du film). Cependant, même dans les images entièrement corrigées, comme le montre la **Figure 4**, les images de l'épaisseur du film semblent plus floues et la masse du film est plus élevée dans des conditions réactives que dans des conditions non-réactives. Cela est probablement dû à l'absorption par des précurseurs des suies de petite taille en dessus du film liquide, non détectée à 310 nm. La contribution de la vapeur était d'environ 25 % du signal d'absorbance dans les deux conditions réactives et non-réactives.

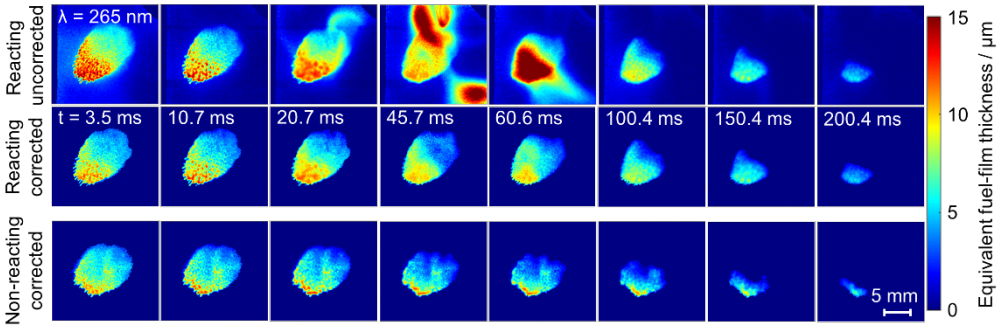

Figure 4. Séquences d'images de l'épaisseur du film de carburant pour le substitut de carburant FS1 dans des conditions réactives (images non corrigées et corrigées) et non-réactives.

Cette technique d'absorption UV-vis s'est concentrée sur la quantification de l'épaisseur du film de carburant, et aucune variation paramétrique n'a été effectuée dans le cadre de cette étude. Dans ce contexte, la technique développée a été utilisée pour étudier le taux d'évaporation du film de carburant liquide en fonction du temps pendant la combustion, et sa dépendance par rapport aux conditions expérimentales. L'imagerie simultanée de l'extinction des suies à plusieurs longueurs d'onde obtenue dans cette technique a le potentiel de fournir des informations supplémentaires sur la maturité locale des suies.

8.2.5 Conclusions

Dans cette thèse, la formation et l'évaporation des films de carburant liquide, ainsi que l'interaction entre les films de carburant et la flamme de prémélange, ont été étudiées expérimentalement. À cette fin, deux paramètres expérimentaux, l'épaisseur du film de carburant liquide et l'extinction des suies, ont été étudiés à l'aide de diagnostics optiques. La technique d'absorption a été adoptée pour mesurer l'épaisseur du film de carburant liquide. La technique DBI a été utilisée pour mesurer l'extinction des suies. Les expériences ont été réalisées dans deux environnements thermodynamiquement contrôlés : une cellule à volume constant à l'IFPEN et une installation à débit d'air constant à l'UDE, dans des conditions non-réactives et réactives. L'épaisseur du film de carburant liquide a été déterminée à partir de l'absorption du toluène autour de 265 nm. Deux substituts de carburant ont été utilisés, le premier composé de 70 % d'iso-octane et de 30 % de toluène, et le second de 60 % d'iso-octane, de 30 % de toluène et de 10 % de n-octane.

Dans la cellule à volume constant, des mesures résolues dans l'espace et dans le temps de l'épaisseur du film de carburant liquide sur une plaque transparente après l'impact du jet de carburant ont été obtenues par la technique d'absorption UV, en utilisant l'imagerie à grande vitesse dans des conditions non-réactives et

réactives. Les images d'extinction des suies ont été acquises simultanément avec les images d'épaisseur du film de carburant liquide.

Dans l'installation à débit d'air constant, une technique d'absorption multispectrale UV-visible multiplexée dans le temps a été mise au point sur la base de la technique d'absorption UV à longueur d'onde unique, afin de tenir compte des contributions de la diffusion de la lumière et de l'extinction des suies et des précurseurs des suies dans la quantification de l'épaisseur du carburant liquide en combustion. L'approche multispectrale a permis d'obtenir des mesures résolues dans l'espace et dans le temps de l'épaisseur du film de carburant liquide, ainsi que des informations supplémentaires sur les suies. La technique développée peut être adaptée à d'autres études de l'interaction entre les films du carburant liquide et la flamme de prémélange dans la cellule à volume constant.

8.2.6 Références

[1] M.C. Drake, T.D. Fansler, A.S. Solomon, G.A. Szekely, JR, Piston fuel films as a source of smoke and hydrocarbon emissions from a wall-controlled spark-ignited direct-injection engine, SAE Tech. Pap. 2003-01-0547 (2003).

[2] E. Stevens and R. Steeper, Piston wetting in an optical DISI engine fuel films, pool fires, and soot generation, SAE Tech. Pap. 2001-01-1203 (2001).

[3] M. Lubnow, T. Dreier, C. Schulz, NIR sensor for aqueous urea solution film thickness and concentration measurement using a broadband light source, Appl. Opt. 58 (16) (2019) 4546–4552.

[4] M. Bardi, G. Bruneaux, A. Nicolle, O. Colin, Experimental methodology for the understanding of soot-fuel relationship in diesel combustion: fuel characterization and surrogate validation, SAE Tech. Pap. 2017-01-0721 (2017).

[5] M. Bardi, R. Payri, L.M. Malbec, G. Bruneaux, L. M. Pickett, J. Manin, T. Bazyn, C. Genzale, Engine combustion network: comparison of spray development, vaporization, and combustion in different combustion vessels, Atomization Sprays 22 (10) (2012) 807–842.

[6] Sandia National Laboratories, Mesh and Geometry, National Technology and Engineering Solutions of Sandia, LLC, 2019, available at <https://ecn.sandia.gov/gasoline-spray-combustion/computational-method/mesh-and-geometry/>, (12 February 2020).

[7] N. Jüngst, *Optical diagnostics for soot formation from evaporating fuel films in combustion*, PhD thesis, Universität Duisburg-Essen, Duisburg, 2021.

[8] M. Bardi, A. Di Lella, G. Bruneaux, A novel approach for quantitative measurements of preferential evaporation of fuel by means of two-tracer laser induced fluorescence, Fuel 239 (2019) 521–533.

DOI: 10.17185/duepublico/79237
URN: urn:nbn:de:hbz:465-20240417-120352-5